

**I. Multiple-Pulse Radio-Frequency Gradient Nuclear Magnetic
Resonance Imaging of Solids**

**II. Optical Nuclear Magnetic Resonance Analysis of Epitaxial Gallium
Arsenide Structures**

Thesis by

John Aaron Marohn

In Partial Fulfillment of the Requirements

for the Degree of

Doctor of Philosophy

California Institute of Technology

Pasadena, California

1996

(Submitted May 31, 1996)

Acknowledgments

I would like to thank my thesis advisor Daniel P. Weitekamp for giving me the freedom to contribute to the invention of two promising techniques; for continuous access to his ideas, perspective, insight, and experimental advice; for always encouraging excellence; and for being a tireless catalyst of personal and professional growth.

I have worked with many wonderful collaborators: Margat Werner, who initiated work on the solids imaging project; Jack Hwang, who, hammer and jigsaw in hand, began construction of the low-temperature optical NMR apparatus with inspiring focus, to be joined by Mike Miller, Paul Carson, and Jim Kempf; Frank Grunthaner, of the Jet Propulsion Laboratory, source of infectious enthusiasm, invaluable advice, and the sample that made the second half of this thesis more than just a proposal. David Shykind, postdoc emeritus, gets special thanks. His creativity, know-how, and moral support made possible the successes of *both* of the projects discussed in this thesis. Guy Duremburg deserves special mention for fearlessly beginning difficult machining jobs late Friday afternoon, and for helping me to appreciate life's lessons.

The Weitekamp group has been a wonderful environment, nurturing a special brand of quantitative curiosity. Contributing to this environment was Herman Cho, Steve Buratto, Russ Bowers, Dan Jones, K.D. Kurur, Pedro Pizarro, Margat Werner, Mike Miller, Gary "Canasta" Leskowitz, Jim Kempf, and especially Paul Carson and Len Mueller. Jim Kempf and Paul Carson deserve special thanks for eleventh-hour help in preparing this manuscript. I thank members of the Zewail group, namely Jennifer Herek, Chuck Williamson, and Soren Pedersen for making the subbasement of Noyes socially and intellectually stimulating.

I thank Katy Johansson for getting me my first research job, and my undergraduate mentor, George McLendon, for encouraging me to work with Mike O'Neil and X-rays for half a summer after isolating the agreed amount of protein. The joy and enthusiasm over science exhibited over three summers by George and his students, especially Katy and Mike, had everything to do with my becoming a scientist.

I can't imagine surviving this Caltech adventure without being able to share in the contagious good humor of Paul and Kirsten Stockman. Dinner rotation members too, past and present, were a source of enduring friendship and support, most notably Cynthia Kiser, Sonja Opstrup, and Tyler Holcomb.

My wife and best friend, Patty Sipman, has been the wind in my sails during every difficult passage of the last few years, both professional and personal, and a source of endless inspiration. I thank her family for adopting, helping, and encouraging me. Let me acknowledge help from members of my own family, especially my uncle David Weimer, a continuing mentor and example, and my sister Amy, who's creativity, and sense of humor and perspective have been such a source of joy to me. Finally, let me thank my parents whose sacrifices and encouragement have helped me realize this thesis. This thesis is dedicated to them.

Abstract

This dissertation details two techniques for materials analysis by nuclear magnetic resonance. The first is a general strategy for recording spin density maps from solids through improved nuclear magnetic resonance imaging. The second involves ultrasensitive methods for detecting nuclear magnetic resonance optically and is applicable to semiconductors at low temperature.

Conventional liquids magnetic resonance imaging (MRI) protocols fail in solids, where rapid local-field dephasing of nuclear magnetization precludes the frequency encoding of spatial information with conventional magnetic field gradients. In our approach, a multiple-pulse line-narrowing sequence is delivered with a solenoid coil to prolong a solid's effective transverse relaxation time. A radiofrequency gradient coil, delivering resonant pulses whose amplitude varies across the sample, is driven in concert with the line-narrowing coil to encode spatial information. The practical implementation of this protocol demanded the construction of an active Q-spoiling circuit to negate coupling of the two isoresonant coils. Two-dimensional Fourier-zugmatographic images of hexamethylbenzene have been obtained that exhibit $300\ \mu\text{m} \times 300\ \mu\text{m}$ planar resolution. This imaging protocol is one of the highest sensitivity methods for imaging solids by NMR (the other involves line narrowing and pulsed DC gradients).

Extraordinary increases in detection sensitivity are required for NMR to study epitaxial semiconductor devices. Optical pumping is one route to such increased sensitivity. Here, a transfer of angular momentum from polarized light to electrons (via selection rules), and electrons to nuclei (through hyperfine couplings), can result in $>10\%$ nuclear spin polarization in less than 5 seconds at 2 K. A total sensitivity gain of 10^5 follows by detecting this large polarization optically, through the inverse process, allowing collection of the NMR spectra for several GaAs-based epitaxial devices. Previous workers observed these spectra to be either power-broadened at the rf levels required to induce optical response, or distorted due to the presence of photocarriers during optical detection. An innovation of the Weitekamp group was to time-sequence and separately optimize the periods of optical pumping, NMR evolution, and optical detection. Although time sequencing in principle allows the collection of multiple-pulse high-resolution NMR spectra, it appeared inadequate when applied to a semiconductors heterojunction.

In conventional NMR, the entire dipole-allowed spectrum may be collected following a single pulse. In time-sequenced optical NMR however, the desired interferogram must be built up pointwise by repetitively incrementing an evolution time. Although sensitive, this experiment is time consuming and sensitive to drift. A new optical detection protocol has been developed which removes these problems and allows NMR spectra to be collected optically in *real time*. In this experiment, a circularly polarized reference nuclear hyperfine field is introduced during the precession of a signal field. The observed luminescence polarization is sensitive to the instantaneous vector sum of the fields, producing Larmor beats. With the reference magnetization in equilibrium through the use of either continuous irradiation or a pulsed spin-lock, the oscillation of luminescence polarization at the Larmor beat frequency is able to record the spectrum of the signal nucleus alone.

A spectrometer has been constructed for implementing both time-sequenced and Larmor-beat optical detection of NMR. In order to implement rotation studies in a way compatible with optical detection at 2K, variable-angle Helmholtz coils have been added to the apparatus so that the direction of the static field can be varied. The results of preliminary rotation studies put a surprisingly low upper bound on the electric fields present at the most rapidly polarizable sites in a AlGaAs/GaAs heterojunction. This can be understood in terms of a model where these sites are neutral donors at locations where the built-in interfacial electric field has fallen off.

Contents

Chapter 1: Overview	1
I Multiple-Pulse Radiofrequency Gradient Nuclear Magnetic Resonance Imaging of Solids.....	2
II Optical Nuclear Magnetic Resonance Analysis of Epitaxial Gallium Arsenide Structures.....	3
III References	6
Chapter 2: Multiple-Pulse Radio-Frequency Gradient NMR Imaging of Solids.....	9
I Abstract	10
II Introduction.....	11
III Multiple-Pulse Line Narrowing.....	12
IV Active Q-Spoiling of Line-Narrowing and Gradient Coils.....	18
V Encoding Spatial Information with Synchronous RF Magnetic Field Gradients.....	19
VI Two Dimensions of Imaging with a Single Gradient Coil	23
VII Conclusions.....	28
VIII Acknowledgments.....	29
IX References.....	30
Chapter 3: Decoupling Two Isoresonant Radiofrequency Coils by Active Q-Spoiling.....	33
I Abstract	34
II Introduction	35
III Pulsed Overcoupling.....	35
IV Diode Driver Circuit.....	40
V Conclusions	43
VI Acknowledgments	44
VII References.....	45
Chapter 4: The Foundations of Optical Nuclear Magnetic Resonance in Semiconductors.....	47
I Abstract	48
II Introduction.....	49
III Selection Rules for Optical Absorption and Emission in Gallium Arsenide.....	49
IV The Interaction of Electrons and Nuclei Through Hyperfine Coupling.....	52
V Optical Nuclear Polarization.....	54
VI The Hanle Effect	59
VII References.....	61

Chapter 5: Optical Detection of Nuclear Magnetic Resonance in III-V

Semiconductors.....	64
I Abstract	65
II Introduction	66
III Equation of Motion for Recombination-Electron Spin Under External and Internal Magnetic Fields	67
IV Conventional Optical Detection of NMR in GaAs Heterostructure	69
V Larmor-Beat Optical Detection of NMR.....	76
VI Larmor-Beat Optical Detection: Beyond Small-Signal Response.....	78
VII Other Sources of Larmor Beats.....	84
VIII Zeeman Frequency Detection of NMR in Semiconductors	85
IX Conclusions.....	86
X Acknowledgments	86
XI Appendix A.....	88
XII Appendix B.....	90
XIII References	92

Chapter 6: Heterodyne RF Spectrometer for Optical Larmor Beat Detection of Nuclear Magnetic Resonance..... 95

I Abstract	96
II Introduction	97
III Spectrometer Requirements	98
IV Cryogenic Equipment.....	100
V Longitudinal and Transverse Magnets	102
VI The Radiofrequency Magnetic Field	102
VII Optics and Determination of Photoluminescence Polarization	103
VIII Demodulating Photoluminescence Polarization During LBD.....	107
IX Time-Sequencing and Computer Control.....	108
X Experiments	111
XI Shot-Noise-Limited Detection.....	112
XII Conclusions.....	114
XIII Acknowledgments.....	114
XIV Appendix.....	115
XV References.....	125

Chapter 7: What Can Optical Nuclear Magnetic Resonance Measure in Single 2D Epitaxial Structures?..... 127

I Abstract	128
II Introduction	129
III Sample and Experimental Details	129
IV Results and Discussion	131
V Conclusions	140
VI Acknowledgments	140

VII References.....142

List of Figures

Chapter 2

FIG. 1. Combined line-narrowing rf-gradient imaging protocol.....	13
FIG. 2. Line-narrowing and gradient coils.....	19
FIG. 3. Orthogonal projections of a hexamethylbenzene phantom.....	21
FIG. 4. Computer simulations of SWW-16 imaging.....	22
FIG. 5. Two-dimensional image of an HMB phantom.....	24
FIG. 6. Two-dimensional image of two capillary tubes of water.....	25
FIG. 7. Computational estimate of solenoid homogeneity.....	27
FIG. 8. Simulated SWW-16- G_x imaging employing a phase-inhomogeneous line-narrowing coil.....	28

Chapter 3

FIG. 1. Reflected voltage from solenoid strongly coupled to, then decoupled from, an adjacent isoresonant gradient coil.....	36
FIG. 2. Homogeneous solenoid and quadrupole gradient coils to be decoupled.....	37
FIG. 3. Tuned circuits associated with FIG. 2 coils.....	39
FIG. 4. Bipolar PIN diode driver.....	41
FIG. 5. Optoisolator circuit for bipolar PIN diode driver.....	42

Chapter 4

FIG. 1. Electronic energy levels and wavefunctions in GaAs.....	50
FIG. 2. Selection rules for near band-edge absorption of circularly-polarized light in GaAs.....	51
FIG. 3. Dynamic nuclear polarization by hyperfine coupling to out-of-equilibrium electrons.....	55
FIG. 4. Maximum achievable dynamic nuclear polarization.....	56
FIG. 5. Time-domain view of the Hanle effect.....	58
FIG. 6. Optically detected NMR spectra of GaAs.....	60

Chapter 5

FIG. 1. Hanle-effect depolarization of luminescence by transverse magnetic fields.....	70
FIG. 2. Hanle-effect depolarization of luminescence in a GaAs heterojunction by a single transverse magnetic field.....	71
FIG. 3. Time-sequenced continuous-wave (CW) optical NMR spectrum of the heterostructure.....	72
FIG. 4. Adiabatic rapid passage steady-state optical NMR of the heterostructure.....	73
FIG. 5. Modulation of ρ in a GaAs heterojunction by longitudinal magnetic fields.....	75
FIG. 6. Evolution of nuclear fields and luminescence polarization during Larmor beat detection.....	77
FIG. 7. Real-time optical detection of the ^{71}Ga free induction decay in a GaAs heterojunction.....	79
FIG. 8. Short-time evolution of luminescence polarization.....	80
FIG. 9. Function determining the DC component of luminescence polarization during LBD experiment.....	82
FIG. 10. Function determining the Fourier component of luminescence polarization at the Larmor-beat frequency.....	82
FIG. 11. Vectors relevant to calculation of Larmor beat signal.....	85

Chapter 6

FIG. 1. Block diagram of the optical nuclear magnetic resonance spectrometer.	99
FIG. 2. Optics for excitation and detection photoluminescence	104
FIG. 3. Detection circuit for demodulation of luminescence oscillating at the Larmor beat frequency. .	105
FIG. 4. Detection circuit for demodulation of luminescence oscillating at the Larmor beat plus PEM frequency.....	106
FIG. 5. Timeline of a representative optical NMR experiment.	109
FIG. 6. “Tuneup” experiment for Larmor beat optical detection.....	110
FIG. 7. Time-sequenced spin-echo spectrum recorded by Larmor beat detection.	111

Chapter 7

FIG. 1. Schematic of the heterojunction sample.	130
FIG. 2. Photoluminescence spectrum of the heterojunction.	131
FIG. 3. Time-sequenced spin-echo NMR employing optical Larmor beat detection.....	132
FIG. 4. Optical NMR spectra of the heterostructure.	134
FIG. 5. Optically-induced Knight shift measurement	135
FIG. 6. Line-narrowed optical NMR spectrum of the heterostructure.	137
FIG. 7. Optical NMR spectra of the unstrained heterostructure.	138

List of Tables**Chapter 2**

TABLE I Important rotating-frame spin interactions.	14
TABLE II Toggling-frame transformations for the CLSW-16 sequence.	16

Chapter 5

TABLE I Small-signal expansions for LBD and TSONMR.	83
--	----

Chapter 1: Overview

1 Multiple-Pulse Radiofrequency Gradient Nuclear Magnetic Resonance Imaging of Solids

Magnetic resonance imaging (MRI) has become the premier tool for the non-destructive evaluation of soft tissue in living systems [1]. Despite remarkable progress [2] and a growing body of applications [3], analysis of solids by NMR remains challenging and nonroutine, for the simple reason that NMR resonances in solids are much broader than in liquids.

As a consequence of nuclei carrying both a magnetic moment and angular momentum, nuclear magnetization precesses in a static magnetic field, with the rate of precession linearly proportional to magnetic field strength (4.258 kHz/Gauss for protons) [4]. Application of a magnetic field gradient makes the precession frequency proportional to position. In liquids MRI, the free induction decay of excited magnetization is recorded in the presence of a magnetic field gradient and Fourier transformed to give an image [1, 5]. Obtaining high resolution images of solids is difficult because magnetization dephases too quickly to discern the gradient-induced difference in precession frequencies between adjacent picture elements.

Mansfield and Grannell [6] first suggested that a useful strategy for the NMR imaging of solids should involve multiple-pulse line narrowing. Their proposal involved an eight pulse sequence to remove dipolar and chemical-shift contributions to the solids linewidth, and required a pulsed gradient of moderate size. Solids imaging by pulsed-field gradients and line-narrowing was first demonstrated by Miller, Cory, and Garroway [7]. An alternative proposal by Cho, Lee, Shykind, and Weitekamp [8] demonstrated an improved line-narrowing sequence, and suggested encoding spatial information with radiofrequency (rf) gradients. In contrast to DC magnetic field gradients, the rapid switching of an rf magnetic field does not produce long-lived eddy currents whose effects are detrimental to the imaging experiment. Non line-narrowing strategies to solids imaging are less fully developed. They involve the use of very large (fringe-field) magnetic field gradients to encode spatial information over very short periods of time [9], and suffer from low sensitivity associated with encoding an image in a large bandwidth.

Chapter 2 details a technique for imaging solids using line-narrowing in conjunction with pulsed radiofrequency gradients. The proposal of Cho et al., is extended by employing a quadrupole rf gradient coil [10, 11]. The action of the rf gradient in concert with the line-narrowing pulses is described using coherent averaging theory [12], where the gradient pulses are treated as spatially-dependent pulse-train errors. Although the quadrupole coil produces gradients in x and y , it is calculated that only the gradient component adjusted to oscillate in phase with the line-narrowing pulses leads to spatially-dependent evolution. It is predicted theoretically and demonstrated experimentally that two dimensional images may be obtained from a single quadrupole gradient coil.

Chapter 3 describes the homebuilt probe used to acquire these images. A complicating factor in our imaging approach is that it requires two resonant rf circuits to operate in close proximity to one another. In general it is difficult to excite such coils independently because the circuits are coupled by mutual inductance and capacitance [13]. This chapter details a method of high-power Q spoiling which mitigates the effect of this coupling and allows independent excitation of the line-narrowing and gradient coils [11, 14].

II Optical Nuclear Magnetic Resonance Analysis of Epitaxial Gallium Arsenide Structures

Epitaxial growth allows atomic-layer control of composition and doping in III-V semiconductor devices [15]. The heterojunction, the junction formed between two dissimilar materials such as AlGaAs and GaAs, is the most important building block for III-V devices to result from this growth technology. Heterojunction devices include [15, 16] room-temperature injection lasers, light-emitting diodes, photodetectors, solar cells, and high electron-mobility transistors.

That conventional NMR is too insensitive to probe the $\sim 10^{12}$ nuclei in a device's active region is disappointing, because NMR should report on important material properties: conduction-electron density through the Knight shift [17-22] and through relaxation time [22]; lattice-mismatch [18] and defect-associated strain [19, 21] through electric-field-gradient induced quadrupole splitting of resonances for spins with $I > 1/2$; and, in analogy with bulk studies, should even allow quantification of electric fields

[23] through the quadrupole splitting. It has been proposed that the isotropic optically-induced Knight shift could be used to map the excited-state electronic wavefunction in a quantum well with atomic resolution [20].

One proven technique for enhancing NMR sensitivity in semiconductors uses optical pumping to create large nonresonant Overhauser-effect enhancements of nuclear polarization [24, 25]. By combining this with optical detection of nuclear magnetization, sensitivity enhancements of $>10^5$ have been observed in epitaxially-grown $\text{Ga}_{1-x}\text{Al}_x\text{As}$ [26] and GaAs [17], and in GaAs/ $\text{Ga}_{1-x}\text{Al}_x\text{As}$ heterojunctions [27] and quantum wells [18, 28]. Unfortunately, the NMR lineshapes observed during steady-state optical detection were distorted in these studies by either the presence of spin-polarized photocarriers or by the high rf powers needed to see signal.

The previous innovation, by the Weitekamp group, of separating periods of optical pumping, NMR evolution, and optical detection enables ultrasensitive detection of NMR in GaAs in a way fully commensurate with high resolution multiple-pulse NMR [19-21]. Application of time-sequenced optical NMR (TSNMR) to the study of an AlGaAs/GaAs heterojunction proved problematical. The point-wise acquisition of NMR transients demanded by the technique were found too time consuming and susceptible to signal drift. These problems were obviated by developing a method for recording NMR transients in *real time*.

Chapter 4 briefly reviews the processes required for optical detection of nuclear magnetic resonance in GaAs including favorable optical selection rules, electron-nuclear hyperfine couplings, and rates for optical-nuclear polarization transfer. The Hanle effect will be introduced as a method for optically encoding magnetic resonance.

Chapter 5 gives experimental motivation for and theoretical analysis of optical Larmor beat detection in semiconductors. Time-sequenced NMR is shown to be incompatible with the large hyperfine fields obtained in an AlGaAs/GaAs heterojunction by optical pumping. Linear response to a transverse signal nuclear field is restored by the introduction of a circularly polarized reference nuclear hyperfine field. Luminescence polarization, sensitive to the instantaneous vector sum of the transverse fields shows

Larmor beats. Larmor beat detection is used to record a real-time optical ^{71}Ga free-induction decay at fixed magnetic field.

Chapter 6 details the homebuilt Larmor beat spectrometer. The spectrometer combines 2 K polarization-resolved photoluminescence detection with an rf heterodyne receiver and a triple-resonance transmitter. Computer synchronization of light shuttering, magnetic field orientation and direction, rf irradiation, and data acquisition enables implementation of both time-sequenced and real-time optical NMR experiments.

Chapter 7 presents data acquired in a sensitive time-sequenced experiment employing Larmor beat detection to read out magnetization. The sample studied here is a single p-channel AlGaAs/GaAs heterojunction. Peak splittings observed in ^{71}Ga FT, nutation, and spin echo spectra are consistent with a narrow distribution of quadrupole couplings whose mean varied between dewar cooling cycles. Although removed with more careful sample mounting, these strain-induced peak splittings show that Larmor beat detection has an orders-of-magnitude resolution advantage over competing fixed-field optical detection methods. Preliminary rotation studies on an unstrained sample are consistent with a surprisingly low upper bound on the electric field present at the most rapidly polarizable sites in the heterojunction. Knight shift measurements corroborate the conclusion that these sites are donors at locations where the built-in interfacial electric field has fallen off. Finally, a spectrum is collected for ^{71}Ga evolving under a 16-pulse line-narrowing sequence which exhibits ~ 50 Hz resolution. This represents a first step toward realization of a proposal for achieving atomic-layer resolved signal using intercalated light and rf pulses [20].

III References

[1] NMR Imaging in Biomedicine,

P. Mansfield and P. G. Morris, Academic Press, Orlando (1982).

[2] *Solid State NMR Imaging*

D. G. Cory, in Annual Reports on NMR Spectroscopy, edited by G. A. Webb, Academic Press, New York, NY (1992), Vol. 24, p. 87.

[3] *NMR Imaging of Polymer Materials*

B. Blumich and P. Blumler, *Makromolekulare Chemie Macromolecular Chemistry and Physics* **194** 2133-61 (1993).

[4] Principles of Nuclear Magnetism,

A. Abragam, Clarendon Press, Oxford (1961).

[5] Principles of Nuclear Magnetic Resonance in One and Two Dimensions,

R. R. Ernst, G. Bodenhausen, and A. Wokaun, Oxford University Press, New York (1987).

[6] *"Diffraction" and Microscopy in Solids and Liquids by NMR*

P. Mansfield and P. K. Grannell, *Physical Review B* **12** 3618-34 (1975).

[7] *Pulsed Field Gradient NMR Imaging of Solids*

J. B. Miller, D. G. Cory, and A. N. Garroway, *Chemical Physics Letters* **164** 1-4 (1989).

[8] *Nutation Sequences for Magnetic Resonance Imaging in Solids*

H. M. Cho, C. J. Lee, D. N. Shykind, and D. P. Weitekamp, *Physical Review Letters* **55** 1923 (1985).

[9] *Formation of Sensitive Layer in Experiments on NMR Subsurface Imaging of Solids*

A. A. Samoilenko, D. Y. Artemov, and L. A. Sibeldina, *JETP Letters* **47** 417-9 (1988).

[10] *Advances in Multiple-Pulse Radio-Frequency-Gradient Imaging of Solids*

J. A. Marohn, D. N. Shykind, M. H. Werner, and D. P. Weitekamp, in Review of Progress in Quantitative Nondestructive Evaluation, edited by D. O. Thomson and D. E. Chimenti, Plenum Corporation, New York (1993), Vol. 12A, p. 687-94.

[11] NMR Imaging of Solids with Multiple-Pulse Line Narrowing and Radiofrequency Gradients,

M. H. Werner, Ph.D. Thesis, Department of Chemistry, California Institute of Technology, Pasadena, CA (1993).

[12] *High Resolution NMR in Solids: Selective Averaging*

U. Haeblerlen, in Advances in Magnetic Resonance, edited by J. S. Waugh, Academic Press, New York, NY (1976).

[13] Radio Engineers Handbook,

F. E. Terman, McGraw-Hill Book Company, Inc., New York (1943).

[14] *Imaging of Solids with RF-Gradients and Line-Narrowing*

M. H. Werner, T. J. Lenosky, D. N. Shykind, and D. P. Weitekamp, 31st Experimental Nuclear Magnetic Resonance Spectroscopy Conference, Pacific Grove, CA, (April 1-5, 1990).

[15] Electronic Structure of Semiconductor Heterojunctions,

G. Margaritondo, Ed., Kluwer Academic Publishers, Milano, Italy (1988).

[16] Physics of Semiconductor Devices, 2nd Edition

S. M. Sze, John Wiley and Sons, NY (1981).

[17] *Low Field Electron-Nuclear Spin Coupling in Gallium Arsenide Under Optical Pumping Conditions*

D. Paget, G. Lampel, B. Sapoval, and V. I. Safarov, Physical Review B **15** 5780 (1977).

[18] *Optically Detected Nuclear Magnetic Resonance of Nuclei within a Quantum Well*

G. P. Flinn, R. T. Harley, M. J. Snelling, A. C. Tropper, and T. M. Kerr, Semiconductor Science and Technology **5** 533 (1990).

[19] *Time-Sequenced Optical Nuclear Magnetic Resonance of Gallium Arsenide*

S. K. Buratto, D. N. Shykind, and D. P. Weitekamp, Physical Review B **44** 9035 (1991).

[20] *Can Nuclear Magnetic Resonance Resolve Epitaxial Layers?*

S. K. Buratto, D. N. Shykind, and D. P. Weitekamp, Journal of Vacuum Science and Technology B **10** 1740 (1992).

[21] *Fourier-Transform Time-Sequenced Optical Nuclear Magnetic Resonance of Gallium Arsenide*

S. K. Buratto, J. Y. Hwang, N. D. Kurur, D. N. Shykind, and D. P. Weitekamp, Bulletin of Magnetic Resonance **15** 190 (1993).

[22] *Electronic States in Gallium-Arsenide Quantum-Wells Probed by Optically Pumped NMR*

R. Tycko, S. E. Barrett, G. Dabbagh, L. N. Pfeiffer, and K. W. West, *Science* **268** 1460-3 (1995).

[23] *Electric Shifts in Magnetic Resonance*

N. Bloembergen, *Proc. Colloq. Ampere (Atomes Mol. Etudes Radio Elec.)* **11** 39-57 (1962).

[24] *Nuclear Dynamic Polarization by Optical Electronic Saturation and Optical Pumping in Semiconductors*

G. Lampel, *Physical Review Letters* **20** 491 (1968).

[25] Optical Orientation,

F. Meier and B. P. Zakharchenya, Eds., Elsevier, Amsterdam (1984).

[26] *Optical Detection of Dynamic Polarization of Nuclei in Semiconductors*

A. I. Ekimov and V. I. Safarov, *JETP Letters* **15** 179 (1972).

[27] *Optically Detected Nuclear Magnetic Resonance and Knight Shift in $Al_xGa_{1-x}As/GaAs$ Heterostructures*

M. Krapf, G. Denninger, H. Pascher, G. Weimann, and W. Schlapp, *Solid State Communications* **78** 459 (1991).

[28] *Optical Polarization of Nuclei in GaAs/AlGaAs Quantum Well Structures*

V. K. Kalevich, V. L. Korenev, and O. M. Fedorova, *JETP Letters* **52** 349 (1990).

Chapter 2: Multiple-Pulse Radio-Frequency Gradient NMR Imaging of Solids

I Abstract

We demonstrate that two-dimensional images of solids can be obtained using a single radiofrequency gradient coil to deliver pulses in the windows of a multiple-pulse line-narrowing sequence. The multiple-pulse sequence averages away evolution due to direct dipolar coupling, chemical shift interactions, and susceptibility effects that would otherwise broaden the NMR spectrum of a solid. Spatial information is introduced by applying spatially-dependent pulses in the windows of the line-narrowing sequence with an rf gradient coil. Two-dimensional Fourier-zeugmatographic images of solids have been obtained with submillimeter resolution.

II Introduction

Modern magnetic resonance imaging has enabled routine non-destructive analysis of soft tissue in living systems [1]. Despite remarkable progress [2, 3], analysis of solids by magnetic resonance imaging remains challenging, for the simple reason that NMR resonances in solids are much broader than in liquids [4]. Since resolving adjacent picture elements Δr apart requires application of a magnetic field gradient $G \geq M_2^{1/2} / \Delta r$ proportional to linewidth $M_2^{1/2}$ (defined as the square root of the second moment of the resonance), imaging a solid requires application of a gradient as large as

$$G = 5 \text{ Tm}^{-1} \quad (M_2^{1/2} = 5 \times 10^{-4} \text{ T}, \Delta r = 10^{-4} \text{ m}).$$

A gradient of this magnitude can be produced by a large superconducting magnet, but because of the difficulties associated with switching such a large magnetic field gradient, “fringe field” imaging protocols [5] must rely on sophisticated sample rotation and employ backprojection reconstruction to obtain three-dimensional images from a single static gradient. Although relatively simple to implement, the methods employ a static gradient inherently incompatible with many powerful solids contrast techniques [2, 3, 6] demanding spectroscopic resolution.

Alternative approaches to NMR imaging of solids seek to reduce $M_2^{1/2}$ by multiple-pulse line narrowing [7, 8]. Consequently, solid’s imaging can be accomplished with a much smaller, switchable, gradient $G^* = 10^{-2} \text{ Tm}^{-1}$ ($M_2^{1/2} = 10^{-6} \text{ T}$, $\Delta r = 10^{-4} \text{ m}$). Moreover, line-narrowing imaging protocols necessarily encode images in a narrower bandwidth resulting in signal-to-noise improved by a large factor, $(G / G^*)^{1/2} \sim 22$ for example.

This paper describes an approach to the imaging of solids by NMR involving line-narrowing and pulsed radiofrequency magnetic-field gradients [9-11]. A gradient coil delivers resonant rf pulses, whose amplitude varies linearly across the sample, in the windows of a multiple-pulse sequence delivered by a solenoid coil producing the usual homogeneous rf magnetic field. The approach may be viewed as a marriage of well-developed rf-gradient liquid-state imaging techniques [12] with proven solids line-narrowing schemes [7, 13, 14].

Competing methods synchronize pulsed DC magnetic field gradients with line-narrowing pulses. By employing rf gradients instead, long-lived eddy currents — deleterious to imaging — are greatly reduced. Another technical advantage of rf gradients is that the circuitry needed to produce rapidly switched gradient-coil rf pulses are already present in many NMR spectrometers. A complicating factor arises, however, when employing two isoiresonant high quality factor Q rf coils operating in close proximity: mutual inductance and capacitance frustrates exciting the coils independently [15]. This is ameliorated by using active high-power Q -switching [9] to transiently decouple the coils.

III Multiple-Pulse Line Narrowing

Nuclear spin interactions contributing to $M_2^{1/2}$ in a solid include chemical shift anisotropy, nuclear electric quadrupole interactions, direct dipole-dipole spin interactions (homonuclear and heteronuclear), indirect spin interactions (homonuclear and heteronuclear), and susceptibility differences across the sample. Multiple-pulse line-narrowing techniques [13, 14] use strong rf pulses to toggle nuclear magnetization with respect to the Zeeman field in such a way as to average away various spin-spin and spin-field interactions. FIG. 1(a) illustrates such a multiple-pulse line narrowing sequence [16]. The sequence is applied repetitively and the magnetization is sampled at the end of each cycle. The Fourier transform of the resulting transient exhibits a single resonance for the sample at the rf carrier frequency which decays with a time constant dependent on the remaining dynamic sources of broadening and experimental limitations of the line-narrowing sequence.

The line-narrowing properties of FIG. 1(a)'s CLSW-16 sequence — and similar “time-suspension” sequences [7] — follow straightforwardly from the sequences' construction from compensated sets [17] of solid-echo sequences and have been previously summarized [7, 16]. The usual quantum-mechanical description of line narrowing [13, 14] will nevertheless be briefly summarized here as a prerequisite for understanding the action of rf-gradient pulses synchronous with line narrowing. It is found experimentally that the usual treatment needs to be extended to describe breakdown of imaging due to experimental imperfections in line-narrowing and gradient-coil inhomogeneity.

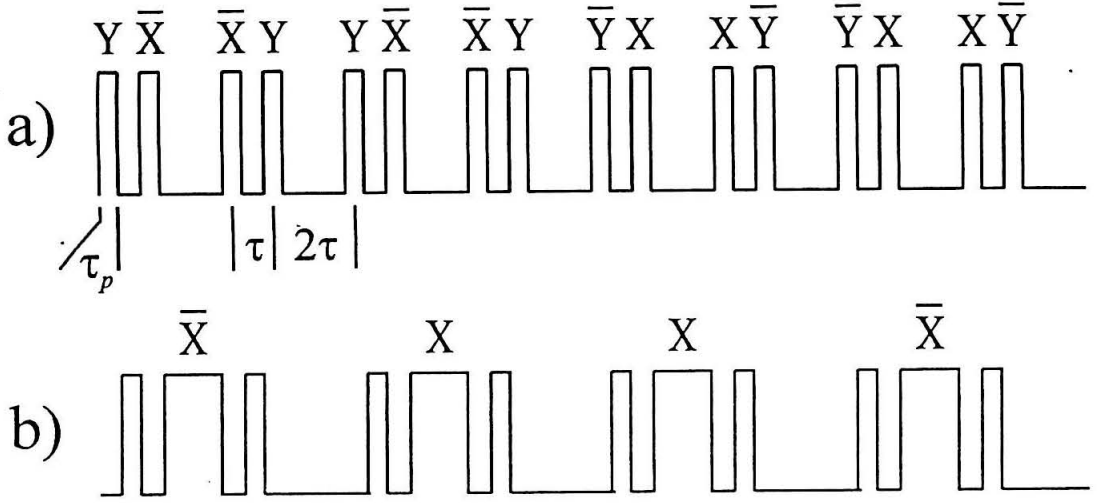


FIG. 1. Combined line-narrowing rf-gradient imaging protocol.

(a) CLSW-16 line-narrowing sequence excites a homogeneous rf coil. All pulses rotate magnetization by $\pi/2$, and the rotating-frame phases of the pulses are given in the convention that $X = 0$, $Y = \pi/2$, $\bar{X} = \pi$, and $\bar{Y} = 3\pi/2$. The spacing between the pulse (length τ_p) centers alternates between τ and 2τ , the cycle time is $\tau_c = 24\tau$. (b) Synchronous rf pulses, applied in the windows of the line-narrowing sequence, drive a gradient coil, encoding spatial information. The gradient is operative for a total time τ_G . The initial adjustable net rotating frame-phase between line-narrowing and gradient pulses is $\phi_G(0)$ (not shown), and the relative phase of the gradient pulses is cycled as shown to lead to constructive interference in gradient evolution.

It is necessary to begin with the lab-frame Hamiltonian describing the interaction of spins I with an external resonant transverse magnetic field of frequency ν and phase $\phi(t)$ delivered by a line-narrowing coil,

$$H_{rf}^{\text{Lab}}(\mathbf{r}, t) = 2\nu_1(\mathbf{r}, t) \{I_x \cos \Delta(\mathbf{r}) + I_y \sin \Delta(\mathbf{r})\} \cos(\nu t + \phi(t)) . \quad (1)$$

I-Spin Interaction	Hamiltonian	Spin Part
Chemical shift	$H_I^O = -\sum_{j=1}^N (\nu_j - \Delta\nu_I) I_{Zj}$	H_Z
Quadrupolar	$H_I^Q = -\sum_{j=1}^N \frac{\nu_{Qj}}{3} (3I_{Zj}^2 - I(I+1))$	H_{ZZ}
Homonuclear dipolar	$H_{II}^D = -\sum_{j<k} D_{jk} (3I_{Zj}I_{Zk} - \mathbf{I}_j \cdot \mathbf{I}_k)$	H_{ZZ}
Homonuclear indirect	$H_{II}^J = -\sum_{j<k} J_{jk} \mathbf{I}_j \cdot \mathbf{I}_k$	—
Heteronuclear dipolar + indirect	$H_{IS} = -\sum_{j<k} F_{jk} I_{Zj} S_{Zk}$	H_Z

TABLE I Important rotating-frame spin interactions.

These interactions need to be coherently averaged by the line-narrowing sequence of FIG. 1(a) as a prerequisite for high-sensitivity solids imaging. The interaction Hamiltonians are usefully characterized as linear (H_Z) or bilinear (H_{ZZ}) in spin I variables.

The field is allowed to have spatially inhomogeneous in-plane magnitude $\nu_1(\mathbf{r}, t)$ and direction (phase) $\Delta(\mathbf{r})$. This Hamiltonian is taken into an interaction representation [13] consisting of a “tilted frame” to remove the spatial variation in magnetic field direction, plus the usual rotating frame. The requisite transformation is

$$H_{\text{rf}} = \exp(-i(\nu t + \Delta(\mathbf{r})) I_z) H_{\text{rf}}^{\text{Lab}} \exp(+i(\nu t + \Delta(\mathbf{r})) I_z). \quad (2)$$

The resulting Hamiltonian, after truncation and assuming homogeneous field strength $\nu_1(t) = \nu_1(\mathbf{r}, t)$, is

$$H_{\text{rf}}(t) = \nu_1(t)(I_x \cos\phi(t) + I_y \sin\phi(t)). \quad (3)$$

The associated propagator — in the “delta-pulse” approximation — for a pulse of length τ_p , strength $\nu_1(0)$, net angle $\nu_1(0)\tau_p = \pi/2$, and phase ϕ_j is

$$P_j = \exp(i \frac{\pi}{2} I_x \cos\phi_j + I_y \sin\phi_j). \quad (4)$$

Rotating-frame Hamiltonians describing the interaction of spins I with the static magnetic field, electric field gradients, themselves, and with other spins S appear in TABLE I. As it will be useful to consider only the spin part of the Hamiltonians manipulated with resonant pulses, TABLE I categorizes I -spin interactions as linear in I_z and proportional to spin operators

$$H_Z \propto I_{zj}, \quad (5)$$

and bilinear in I_z , proportional to spin operators

$$H_{ZZ} \propto 3I_{zj}I_{zk} - \mathbf{I}_j \cdot \mathbf{I}_k. \quad (6)$$

The total time-dependent “internal” Hamiltonian is a sum of all these interactions:

$$H_{\text{int}} = H_I^O + H_I^Q + H_{II}^D + H_{II}^J + H_{IS}. \quad (7)$$

The associated propagator is:

$$U_j(\tau_j) = \exp(-i \tau_j H_{\text{int}}) \quad (8)$$

The subscript on the propagator will be used shortly to keep track of propagators appearing after different pulses in the line-narrowing sequence.

Density matrix evolution under the 16-pulse sequence of FIG. 1(a) is approximated by instantaneous rf-pulse rotations followed by internal-Hamiltonian evolution during windows between the pulses. In the notation of reference [14], the density matrix at times $n\tau_c$ is

$$|\sigma(n\tau_c)\rangle = \{ U_{16}(\tau) P_{16} \cdots U_2(\tau) P_2 U_1(2\tau) P_1 U_0(\tau) \}^n |\sigma(0)\rangle. \quad (9)$$

A “toggling frame” interaction representation [13] removes the pulse propagators from this expression.

Let

$$U_j(\tau) = P_j \cdots P_2 P_1 \tilde{U}_j(\tau) P_1^{-1} P_2^{-1} \cdots P_j^{-1} \equiv U_{\text{rf},j} \tilde{U}_j(\tau) U_{\text{rf},j}^{-1}, \quad (10)$$

where $\tilde{U}_j(\tau)$ are the toggling frame propagators and $U_{\text{rf},j}$ defines unitary transformations into the toggling frame for Hamiltonians during the $j = 1$ to 16 windows of the pulse sequence. Substituting Equation (10) into (9) gives the simplified propagator

$$|\sigma(n\tau_c)\rangle = \{ \tilde{U}_{16}(\tau) \tilde{U}_{15}(2\tau) \cdots \tilde{U}_2(\tau) \tilde{U}_1(2\tau) \tilde{U}_0(\tau) \}^n |\sigma(0)\rangle, \quad (11)$$

where we have used the result that the 16-pulse sequence is cyclic in the sense that $U_{\text{rf},16} = 1$. The exponents in (11) now involve non-commuting toggling-frame Hamiltonians:

$$\tilde{H}_j = U_{\text{rf},j}^{-1} H_{\text{int}} U_{\text{rf},j}. \quad (12)$$

window j	$U_{rf,j}^{-1}$	$\tilde{T}_{x,j}$	$\tilde{T}_{y,j}$	$\tilde{T}_{z,j}$
0	1	+X	+Y	+Z
1	$\exp(i\frac{\pi}{2}I_y)$	-Z	+Y	+X
2	$\exp(i\frac{\pi}{2}I_y)\exp(-i\frac{\pi}{2}I_x)$	-Z	-X	+Y
3	$\exp(i\frac{\pi}{2}I_y)\exp(-i\pi I_x)$	-Z	-Y	-X
4	$\exp(i\frac{\pi}{2}I_y)\exp(-i\pi I_x)\exp(i\frac{\pi}{2}I_y)$	+X	-Y	-Z
5	$\exp(i\frac{\pi}{2}I_y)\exp(-i\pi I_x)\exp(i\pi I_y)$	+Z	-Y	+X
6	$\exp(i\frac{\pi}{2}I_y)\exp(-i\pi I_x)\exp(i\pi I_y)\exp(-i\frac{\pi}{2}I_x)$	+Z	-X	-Y
7	$\exp(i\frac{\pi}{2}I_y)\exp(-i\pi I_x)\exp(i\pi I_y)\exp(-i\pi I_x)$	+Z	+Y	-X
8	$\exp(i\frac{\pi}{2}I_y)\exp(-i\pi I_x)\exp(i\pi I_y)\exp(-i\pi I_x)\exp(i\frac{\pi}{2}I_y)$	+X	+Y	+Z
9	$\exp(i\frac{\pi}{2}I_y)\exp(-i\pi I_x)\exp(i\pi I_y)\exp(-i\pi I_x)$	+Z	+Y	-X
10	$\exp(i\frac{\pi}{2}I_y)\exp(-i\pi I_x)\exp(i\pi I_y)\exp(-i\frac{\pi}{2}I_x)$	+Z	-X	-Y
11	$\exp(i\frac{\pi}{2}I_y)\exp(-i\pi I_x)\exp(i\pi I_y)$	+Z	-Y	+X
12	$\exp(i\frac{\pi}{2}I_y)\exp(-i\pi I_x)\exp(i\frac{\pi}{2}I_y)$	+X	-Y	-Z
13	$\exp(i\frac{\pi}{2}I_y)\exp(-i\pi I_x)$	-Z	-Y	-X
14	$\exp(i\frac{\pi}{2}I_y)\exp(-i\frac{\pi}{2}I_x)$	-Z	-X	+Y
15	$\exp(i\frac{\pi}{2}I_y)$	-Z	+Y	+X
16	1	+X	+Y	+Z

TABLE II Toggling-frame transformations for the CLSW-16 sequence.

The last columns exhibit toggling-frame values for operators I_x , I_y , and I_z in shorthand notation. Values \tilde{T}_z are needed to describe line narrowing, while \tilde{T}_x and \tilde{T}_y are used to compute the net effect of rf-gradient pulses.

Toggling-frame transformation operators for the sequence appear in TABLE II. The desired propagator is simplified by employing the Magnus expansion [13, 18],

$$|\sigma(n\tau_c)\rangle = \exp(-i n \tau_c \{ \overline{H}_{\text{int}}^{(0)} + \overline{H}_{\text{int}}^{(1)} + \overline{H}_{\text{int}}^{(2)} + \dots \}) |\sigma(0)\rangle, \quad (13)$$

where the first three terms in the expansion appear below.

$$\overline{H}_{\text{int}}^{(0)} = \frac{1}{\tau_c} \sum_{j=0}^{16} \tau_j \tilde{H}_j \quad (14)$$

$$\overline{H}_{\text{int}}^{(1)} = \frac{-i}{2\tau_c} \sum_{j=0}^{16} \sum_{k=0}^j [\tau_j \tilde{H}_j, \tau_k \tilde{H}_k] \quad (15)$$

$$\overline{H}_{\text{int}}^{(2)} = \frac{1}{6\tau_c} \sum_{j=0}^{16} \sum_{k=0}^j \sum_{l=0}^k \{ [\tau_j \tilde{H}_j, [\tau_k \tilde{H}_k, \tau_l \tilde{H}_l]] + [\tau_l \tilde{H}_l, [\tau_k \tilde{H}_k, \tau_j \tilde{H}_j]] \} \quad (16)$$

The sums are over pulse-sequence windows, with τ_j (either τ or 2τ) the length of the j th window. The first term, which corresponds to adding non-commuting exponents in Equation (11), is called the average Hamiltonian.

This description of evolution is sufficient to understand line narrowing by the 16-pulse sequence in the delta-pulse limit. From TABLE II, average Hamiltonian contributions from linear and bilinear internal spin Hamiltonians are computed as

$$\overline{H}_Z^{(0)} = \sum_{j=0}^{16} \tau_j (\tilde{I}_z)_j = 0 \quad (17)$$

and

$$\overline{H}_{ZZ}^{(0)} = 0. \quad (18)$$

The last sum follows from $H_{XX} + H_{YY} + H_{ZZ} = 0$. From the first result, we conclude that

$$\overline{H}_O^{(0)} = \overline{H}_{IS}^{(0)} = 0 \text{ and from the second result, it follows that } \overline{H}_D^{(0)} = \overline{H}_Q^{(0)} = 0. \text{ To zeroth order in an}$$

average Hamiltonian description of line-narrowing, then, the sample's I -spin nuclei have been rendered magnetically equivalent. Homonuclear indirect couplings are unscaled by the pulse sequence:

$\overline{H}_J^{(0)} = H_J$. Fortunately, magnetic equivalence — unbroken over relevant length scales even during imaging — guarantees that these residual couplings do not also contribute to $M_2^{1/2}$ in zeroth order [19].

That CLSW-16 also removes all contributions to $M_2^{1/2}$ to first order follows from reflection symmetry about $\tau/2$ of all toggling-frame Hamiltonians [13, 20], which demands that all $H_{\text{int}}^{(\text{odd})}$ vanish. The

largest non-zero correction term in the Magnus expansion is therefore found to be of second order:

$$\overline{H}_D^{(2)} \propto \frac{\tau^2}{18} \{ [H_{Dy} - H_{Dx}, [H_{Dy}, H_{Dx}]] - [H_{Dx} - H_{Dy}, [H_{Dz}, H_{Dx}]] \} \quad (19)$$

Although time-suspension pulse sequences averaging internal Hamiltonians to even higher order have been reported [7], the reduction in $M_2^{1/2}$ by CLSW-16 is already dramatic. The 14 kHz linewidth of a representative hexamethylbenzene sample (whose image is shown in FIG. 4) is narrowed to less than 80 Hz by application of the CLSW-16 sequence ($\tau_p = 2.1 \mu\text{s}$ and $\tau_c = 218.4 \mu\text{s}$). This linewidth reduction is more than sufficient to demonstrate imaging by introduction of spatial information with modest resonant pulses to an rf gradient coil.

IV Active Q-Spoiling of Line-Narrowing and Gradient Coils

Any protocol that requires two high- Q iso-resonant rf coils operating in close proximity must contend with capacitive and inductive inter-circuit coupling [15]. In our application, the coupling frustrates pulsing independently the homogeneous magnetic field of the solenoidal line-narrowing coil and the quadrupolar field of the gradient coil, and lowers the Q of both associated circuits.

Inductive coupling may in principle be removed by orienting the coils to have net orthogonal magnetic field distributions. Found difficult in practice, minimizing residual capacitive coupling often demands further that one coil sit well inside the other, compromising filling factor [4]. Fortunately because the line-narrowing and gradient coils operate in distinct time intervals, other decoupling schemes can be employed. Most successful decoupling schemes involve Q -switching. Passive self Q -switching strategies rely on circuits employing $\lambda/4$ lines [21] or non-linear circuit elements — such as diodes [22] — which compromise either the circuits' Q , time response, or both. Previous active decoupling schemes employed slow magnetic reed relays [23] or high- Q PIN diodes which had acceptable time response (μsec), but operated only at low power [24, 25].

A key experimental development, therefore, in the line-narrowing rf-gradient imaging of solids was a method of *active high-power* Q -switching to mitigate inter-circuit coupling [9]. To enable Q switching, PIN diodes are added in series to ground with the matching capacitors of the series-tuned resonance LC circuits of both solenoid and quadrupole coil networks, such that only when the PIN diodes

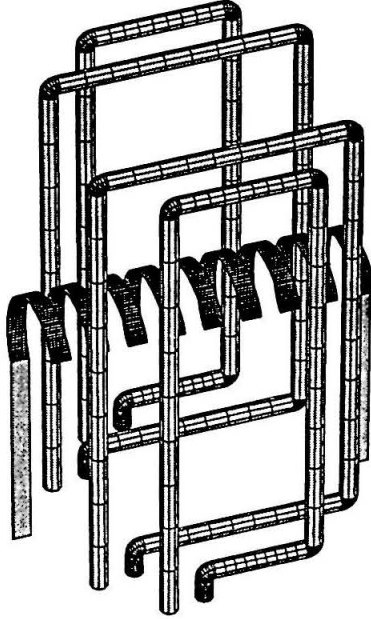


FIG. 2. Line-narrowing and gradient coils.

A solenoid (9 turns of ~ 1.5 mm copper strip, inner diameter 5.2 mm, length 26 mm) delivers line-narrowing pulses while a quadrupole coil delivers rf-gradient pulses (diameter $d = 20$ mm, height 35 mm).

are forward biased is the circuit properly matched (coupled) to its transmission line. *Passive overcoupling* to lower Q and improve an NMR probe's transient response is well known [26].

V Encoding Spatial Information with Synchronous RF Magnetic Field Gradients

A quadrupole gradient coil [27, 28] produces a magnetic field

$$B_G(\mathbf{r}) = \frac{I_G \mu_0}{d^2} (x \hat{x} + y \hat{y}) , \quad (20)$$

where I_G is the current through the coil, μ_0 is free-space permeability, and d is the diameter of the coil (FIG. 2). The coil is driven with amplitude- (I_G) and phase- (ϕ_G) modulated resonant pulses of

frequency ν , according to the sequence in FIG. 1(b). The lab-frame Hamiltonian describing the interaction between the coil's magnetic field and nuclear spins I is

$$H_G^{\text{Lab}}(\mathbf{r}, t) = 3 G_0(t) \{x I_x + y I_y\} \cos(\nu t + \phi_G(t)), \quad (21)$$

where $G_0(t) = \gamma I_G(t) \mu_0 / 3d^2$ is the gradient amplitude converted to kHz/meter through the gyromagnetic ratio γ . The transformation of equation (2) takes this lab-frame Hamiltonian into the same "tilted" and "rotating" frame used to remove pulse-phase spatial inhomogeneity and time dependence from the homogeneous-pulse Hamiltonian. The result, once truncated, is

$$H_G(\mathbf{r}, t) = \frac{3}{2} G_0(t) \{ x [I_x \cos(\Delta(\mathbf{r}) - \phi_G(t)) + I_y \sin(\Delta(\mathbf{r}) - \phi_G(t))] + y [I_x \sin(\Delta(\mathbf{r}) - \phi_G(t)) - I_y \cos(\Delta(\mathbf{r}) - \phi_G(t))] \} \quad (22)$$

This result confirms that the proximate action of the rf-gradient is to nutate magnetization around the x and y axis in a rotated and tilted frame of reference defined by the line-narrowing pulses; calculation of the net effect over the pulse sequence of FIG. 1 requires coherent averaging theory [13]. The treatment closely parallels the treatment of pulse-amplitude errors [29]. Since the gradient pulses act during periods which, in the absence of the gradient, would involve free evolution under H_{int} , it is natural therefore to treat them as part of the internal Hamiltonian (now time dependent). An average Hamiltonian for the time-dependent gradient pulses is therefore calculated in the toggling frame, using equation (14) and with the help of TABLE II; only \tilde{I}_x contributes. The result is

$$\bar{H}_G^{(0)}(\mathbf{r}) = \nu_G(\mathbf{r}, \phi_G(0)) I_z \quad (23)$$

$$\nu_G(\mathbf{r}, \phi_G(0)) \equiv G_0 \{ x \cos(\Delta(\mathbf{r}) - \phi_G(0)) + y \sin(\Delta(\mathbf{r}) - \phi_G(0)) \} \quad (24)$$

The net effect of the pulsed rf gradient is therefore to precess magnetization about the z axis at a rate $\nu_G(\mathbf{r}, \phi_G(0))$ dependent on spatial position and the initial rotating- and tilted-frame phase difference $\phi_G(0)$ between line-narrowing and gradient pulses. Suppose line narrowing is accomplished with a perfect solenoid in the sense that $\Delta(\mathbf{r}) = 0$. Then

$$\bar{H}_G^{(0)}(\mathbf{r}, \phi_G(0) = 0) = G_0 x I_z \quad (25)$$

$$\bar{H}_G^{(0)}(\mathbf{r}, \phi_G(0) = -\pi/2) = G_0 y I_z \quad (26)$$

which indicates that by varying the relative phase between pulses to the line-narrowing and gradient coils, magnetization can be evolved at a frequency proportional to either x or y position alone.

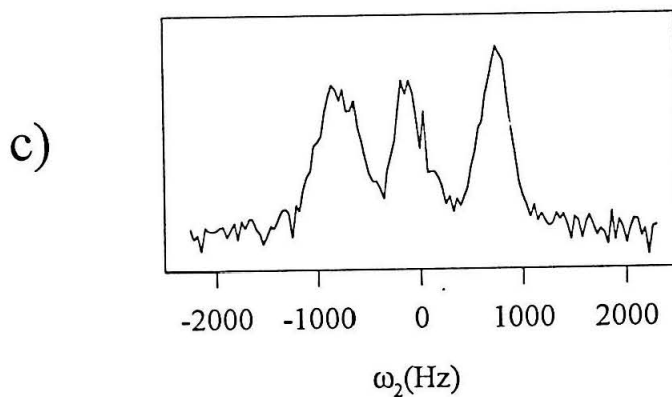
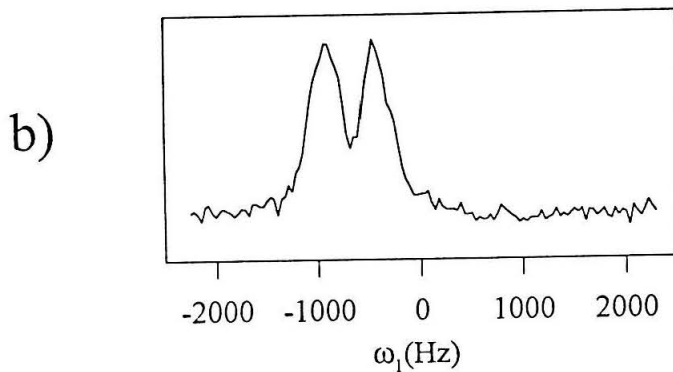
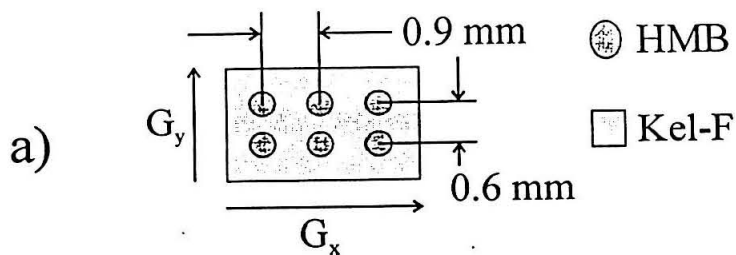


FIG. 3. Orthogonal projections of a hexamethylbenzene phantom.

(a) Six-point hexamethylbenzene (HMB) phantom. The six HMB cylinders are 0.9 mm in diameter and 1 mm deep. (b) Imaged in one dimension with SWW-16- G_x ($\tau_p = 2.1 \mu\text{s}$ with 60 W line-narrowing pulses, $\tau_G = 84.4 \mu\text{s}$ with 300 W gradient pulses, and $\tau_c = 214.8 \mu\text{s}$.) (c) Imaged in an orthogonal dimension with SWW-16- G_x . The effective gradient strength G_0 is determined from the projection's peak splittings and known sample geometry to be $0.85 \pm 0.15 \text{ G/cm}$. These proton-density profiles highlight the ability of a combined line-narrowing rf-gradient imaging protocol to image along two orthogonal directions using a single quadrupole gradient coil.

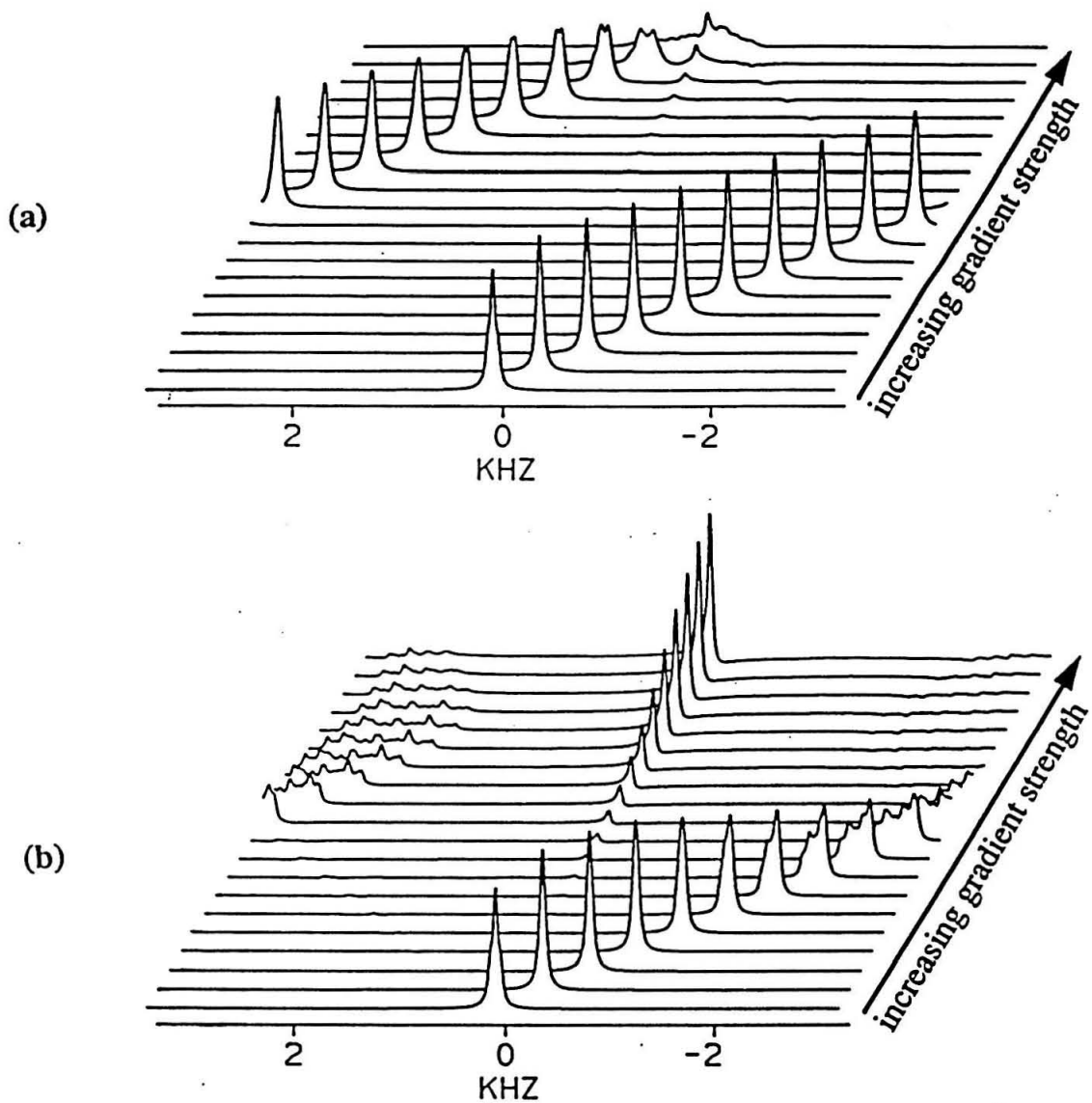


FIG. 4. Computer simulations of SWW-16 imaging.

(a) One-dimensional gradient coil. (b) Quadrupole coil. The presence of a gradient G_x leads to

shifts in line position across the "sample." The additional gradient G_y in the quadrupole coil contributes to spatially-dependent line width. Parameters $\tau_p = 2.7 \mu\text{s}$ and $\tau_c = 152.4 \mu\text{s}$.

Chemical shifts and dipolar couplings (in Hz) for the 5-spin system were $\nu_1=1000$, $\nu_2=900$, $\nu_3=400$, $\nu_4=-100$, $\nu_5=-500$, $D_{12}=600$, $D_{13}=200$, $D_{14}=100$, $D_{15}=2300$, $D_{23}=2500$, $D_{24}=100$, $D_{25}=200$, $D_{34}=2000$, $D_{35}=1000$, $D_{45}=3000$. The one-pulse line width was $\gamma M_2^{1/2} \sim 20 \text{ kHz}$.

This is observed experimentally in FIG. 3. It is useful to distinguish two sequences corresponding to the interspersed line-narrowing and gradient pulse of FIG. 1, SWW-16- G_x when $\phi_G(0) = 0$ and SWW-16- G_y when $\phi_G(0) = -\pi/2$. Orthogonal one-dimensional proton-density images of a hexamethylbenzene phantom acquired using alternatively SWW-16- G_x or SWW-16- G_y clearly illustrate the ability of the combined line-narrowing rf-gradient imaging protocol to select for $\overline{H}_G^{(0)}$ evolution due to one desired gradient component alone.

The exact numerical simulations of FIG. 4 assess the effect of the undesired gradient component on line narrowing on a 5-spin system. The figure plots the Fourier transform of rotating-frame magnetization evolved under the pulse sequence of FIG. 1, in the gradient of Equation (22) with $\Delta(\mathbf{r}) = 0$. In FIG. 4(a), x is stepped from $x_i = 0$ to $x_f = 2\pi / (\tau_c G_0)$ with $y = 0$, simulating SWW-16 evolution at different positions in a simple one-dimensional gradient coil. In FIG. 4(b), x is stepped similarly with $y = x$, simulating SWW-16 evolution at points along the diagonal of a quadrupole coil.

Line shifts in both simulations scale linearly with position x alone as expected from Equation (25). The difference in linewidths between FIG. 4(a) and FIG. 4(b) is due to the presence of the orthogonal gradient in FIG. 4(b), which contributes through \tilde{I}_y to correction terms to the average Hamiltonian. Note that reliable estimates of line-narrowing efficacy were only obtained using more than three spins in the simulation, as expected from Equation (19), because residual line width is governed by 3-spin terms in $\overline{H}_D^{(0)}$. Furthermore, it was observed that placing gradient pulses symmetrically in the multiple-pulse windows (as in the experiment) minimizes gradient contributions to line width in both FIG. 4(a) and FIG. 4(b).

VI Two Dimensions of Imaging with a Single Gradient Coil

FIG. 5 plots in magnitude mode a two-dimensional image acquired by combining SWW-16- G_x and SWW-16- G_y into a pulse sequence analogous to that used in liquid-state Fourier-zugmatographic imaging [1, 30, 31]. The resolution expected based on measured gradient strength and known gradient-free line width is 150 μm . The observed resolution, taken as the width of the Lorentzian which when

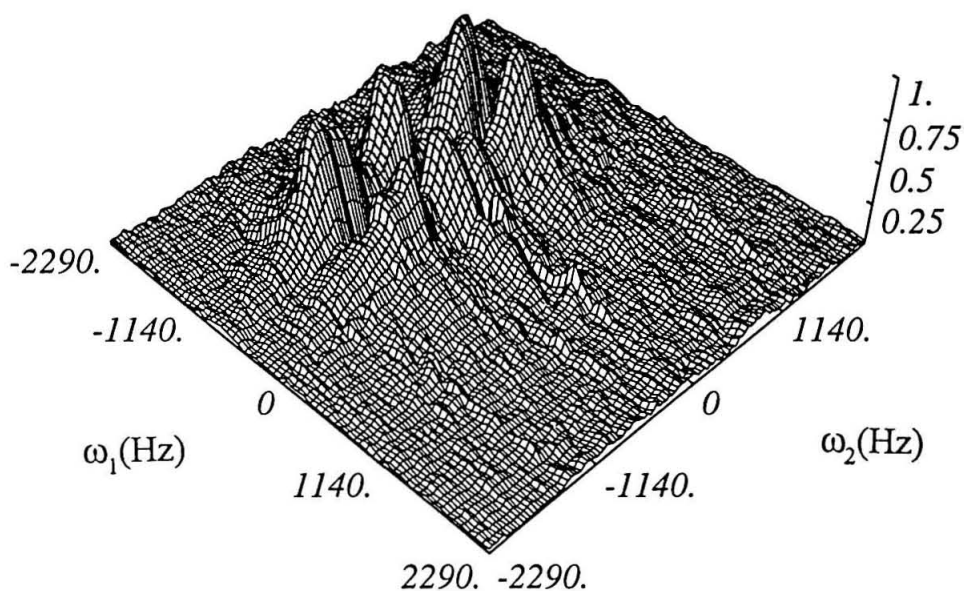


FIG. 5. Two-dimensional image of an HMB phantom.

Magnetization was evolved under the sequence $\pi/2-(\text{SWW}-16\text{-G}_x)_N-(\text{SWW}-16\text{-G}_x)_M$.

Twenty four signal averages of an $N_{\text{max}}=64$, $M_{\text{max}}=128$ data set were collected in approximately one hour on a modified Bruker MSL-200 spectrometer with line-narrowing and gradient parameters as in FIG. 3. The resulting interferogram was baseline corrected, line broadened (by 36 Hz in N and 18 Hz in M), and Fourier transformed along both dimensions. The resulting proton density image, plotted in magnitude mode, exhibits $\sim 300 \mu\text{m}$ resolution in each imaged dimension.

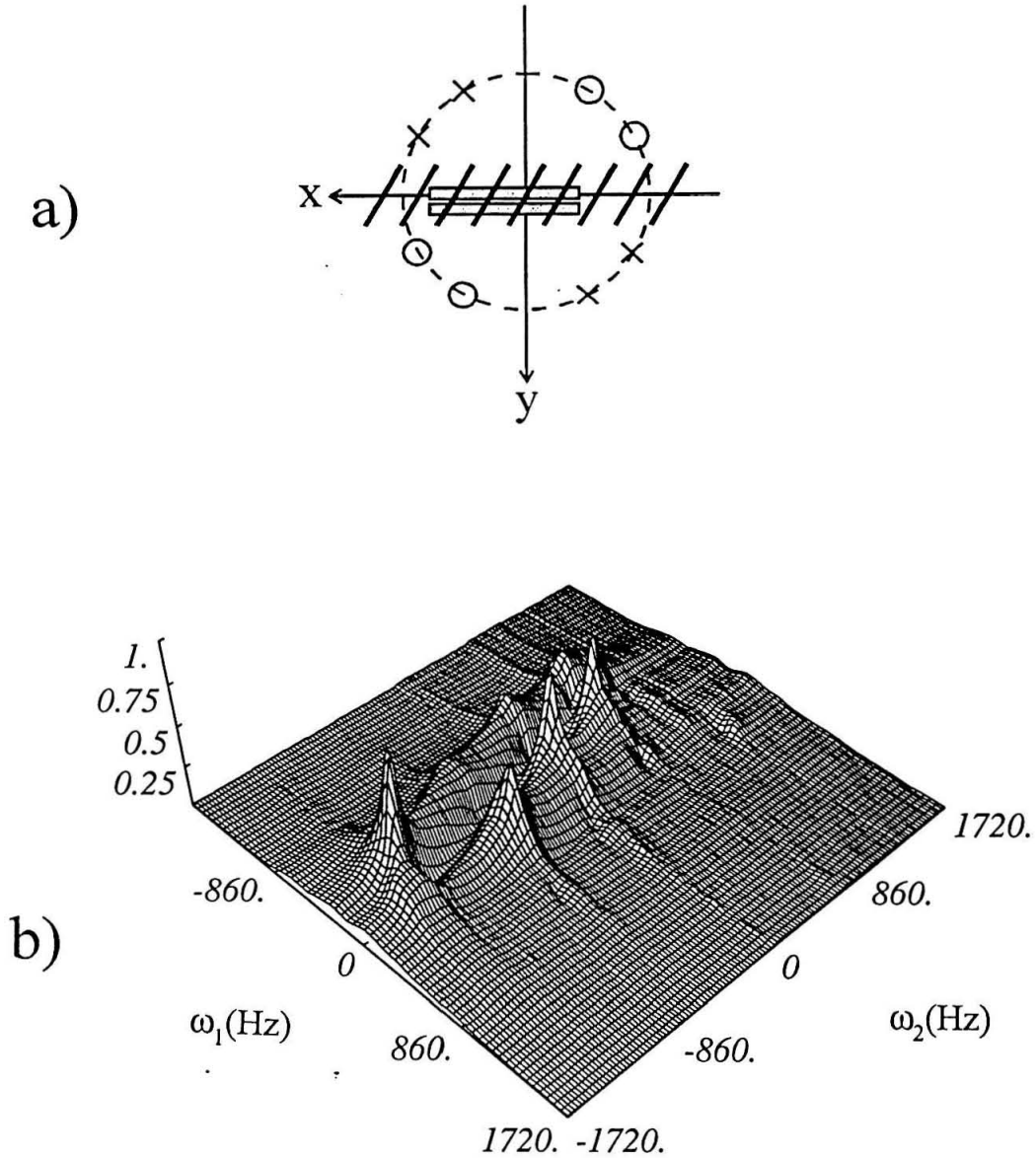


FIG. 6. Two-dimensional image of two capillary tubes of water.

(a) Two capillary tubes (0.9 mm inner diameter) are centered vertically in the solenoid. One tube, filled with 13.5 mm of water, resides ~ 2 mm from the solenoid edge at $y = -0.6$ mm. A twin tube, filled with 14 mm of water, is placed only ~ 1 mm from the opposite solenoid edge at $y = +1.6$ mm. (b) Two-dimensional magnitude-mode proton-density map, acquired and worked up as in FIG. 5, shows pronounced irregularities (see text for hypothesis).

convolved with the known spin density gives the observed linewidth, is roughly 300 μm . Convolution with a more relevant 2D magnitude-mode lineshape [31] would improve this estimate of observed resolution. Such an extension would fail, however, to account for obvious peak-height and position irregularities exhibited in the image.

These irregularities are even more pronounced in the image of a sample occupying a larger volume fraction of the line-narrowing coil. The image of two capillary tubes of water in FIG. 6 shows irregularities that have the same spatial period as the turns of the line-narrowing solenoid and that are more pronounced in sections of the image corresponding to positions further from the solenoid center.

A contributing cause for the observed “striping” is likely the breakdown of line narrowing due to rf inhomogeneity in the solenoid. FIG. 7(a) exhibits the calculated line-narrowing pulse angle $\theta_p(\mathbf{r})$ along a line in the solenoid corresponding to the near-solenoid edge of the water capillary of FIG. 6(a). While such large variations in pulse angle are sufficient to cause breakdown of line-narrowing in HMB, if not water, it may be shown that spatial variations in the phase $\Delta(\mathbf{r})$ of the solenoid pulses is alone probably large enough to cause the striping in FIGS. 5 and 6.

The effect of $\Delta(\mathbf{r})$ upon rf-gradient imaging may be addressed by numerically simulating magnetization evolving along the line $(x, y_0, 0)$ where x runs from $-x_0$ to $+x_0$. A time-domain signal may be calculated according to

$$S(t, y_0, \phi_G(0)) = \int_{-x_0}^{x_0} dx \exp(-i v_G(x, y_0, \phi_G(0))t - \Gamma t), \quad (27)$$

where $v_G(x, y_0, \phi_G(0))$ is the frequency of evolution along the line, dependent upon $\Delta(\mathbf{r})$ according to eqns. (23-24), and Γ is a line-broadening parameter. The simulation of FIG. 7(b) provides values for $\Delta(x, y_0)$. FIG. 8(a) plots the Fourier transform of $S(t, 1.6, 0)$, representing the SWW-16- G_x image of a filamentary phantom at $y_0 = 1.6$ mm stretching the length of the line-narrowing coil. For comparison, FIG. 8(b) plots the same image simulated with a simple one-dimensional gradient coil, for which

$$v_G(\mathbf{r}, \phi_G(0)) = G_0 x \cos(\Delta(\mathbf{r}) - \phi_G(0)). \quad (28)$$

The difference in the two figures is due to the breakdown, when employing a phase-inhomogeneous line-narrowing coil, of SWW-16’s ability to select for evolution due to one gradient component alone.

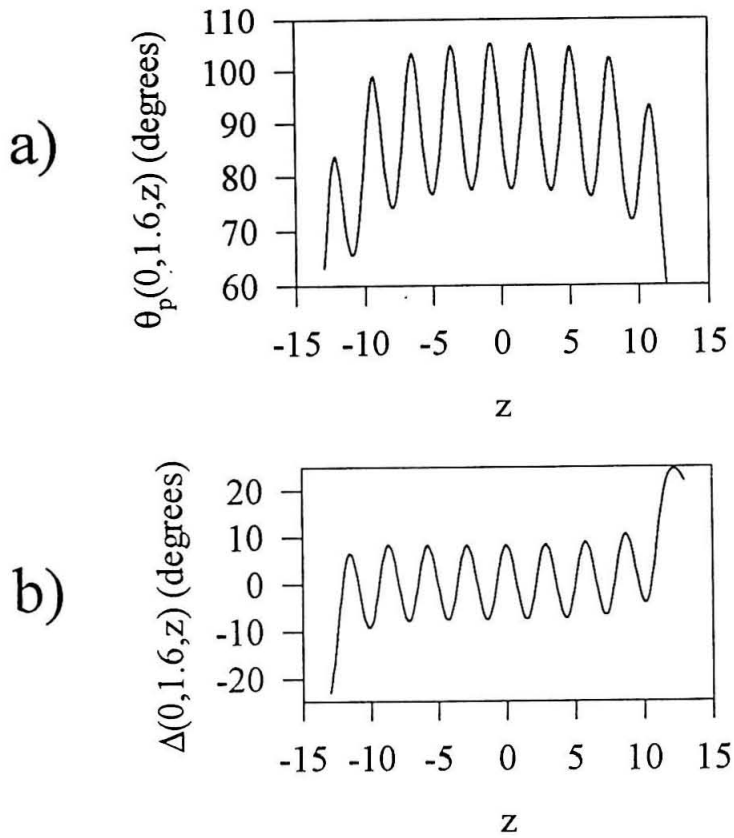


FIG. 7. Calculational estimate of solenoid homogeneity.

The experiment's strip-wire solenoid was modeled as a filament of current (length 26 mm, 9 turns) whose magnetic field along $y = 1.6$ mm was calculated by numerically integrating the Biot-Savart equation along the solenoid's current path. (a) In-plane magnetic field magnitude plotted as effective pulse angle referenced to $\theta_p(0,0,0) = 90^\circ$. (b) In-plane magnetic field angle, plotted as solenoid pulse phase referenced to the coil axis.

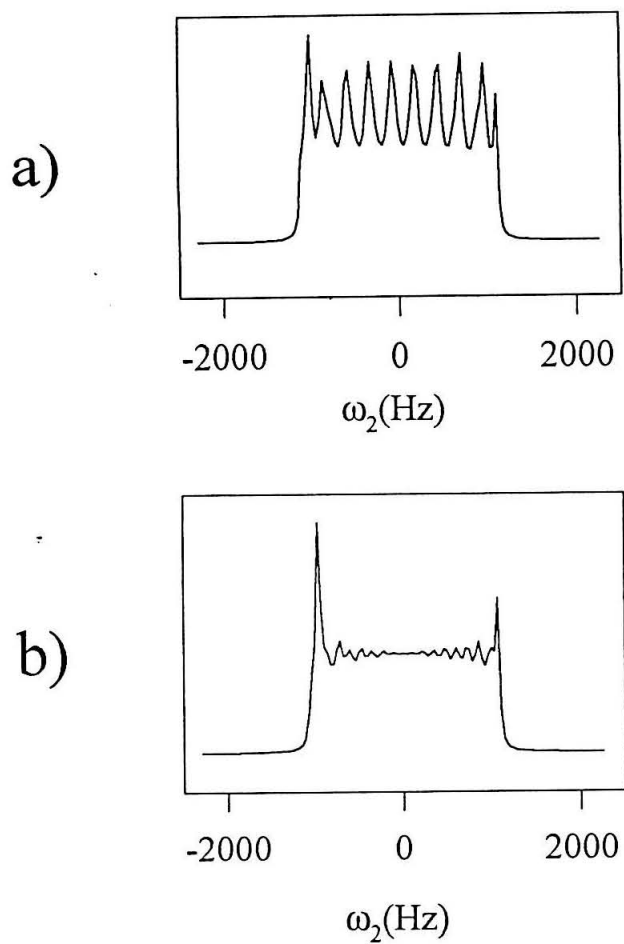


FIG. 8 Simulated SWW-16- G_x imaging employing a phase-inhomogeneous line-narrowing coil. Spatial information is encoded using a quadrupole gradient in (a) and a conventional gradient coil in (b).

VII Conclusions

A multiple-pulse rf-gradient NMR imaging protocol for obtaining two-dimensional spin-density maps in solids has been demonstrated. While the method requires active high-power Q -switching to decouple isoresonant line-narrowing and gradient coils, it utilizes rf amplifiers to drive the gradient coils

which are already part of many commercial spectrometers. Extension of imaging to three dimensions is straightforward since the Q -switching coil-decoupling scheme generalizes to an arbitrary number of coils, since only one at a time need be active.

The protocol shares with other line-narrowing approaches compatibility with any spectroscopic solids-contrast mechanism. The method is unique in its ability to obtain two-dimensional solids images from a single gradient coil. This ability requires not only rf-coil homogeneity demanded by any multiple-pulse experiment, but is sensitive to rf-coil phase inhomogeneity as well. The protocol should allow two-dimensional images to be collected using two orthogonal gradient coils, which strongly relaxes the line-narrowing coil's phase-homogeneity requirement.

VIII Acknowledgments

The authors thank S. W. Sinton and J. H. Iwamiya for advice on implementing NMR imaging on a Bruker MSL-200 spectrometer. This work was supported by grants from Lockheed Missiles and Space Company Incorporated and the National Science Foundation (CHE-9005964).

IX References

[1] NMR Imaging in Biomedicine,

P. Mansfield and P. G. Morris, Academic Press, Orlando (1982).

[2] Solid State NMR Imaging

D. G. Cory, in Annual Reports on NMR Spectroscopy, edited by G. A. Webb, Academic Press, New York, NY (1992), Vol. 24, p. 87.

[3] NMR Imaging of Polymer Materials

B. Blumich and P. Blumler, *Makromolekulare Chemie Macromolecular Chemistry and Physics* **194** 2133-61 (1993).

[4] Principles of Nuclear Magnetism,

A. Abragam, Clarendon Press, Oxford (1961).

[5] Formation of Sensitive Layer in Experiments on NMR Subsurface Imaging of Solids

A. A. Samoilenko, D. Y. Artemov, and L. A. Sibeldina, *JETP Letters* **47** 417-9 (1988).

[6] High-Resolution NMR Spectroscopy of Synthetic Polymers in Bulk,

R. Komoroski, Ed., VCH Publishers, Inc., Deerfield Beach, FL (1986).

[7] Time-Suspension Multiple-Pulse Sequences Applications to Solid-State Imaging

D. G. Cory, J. B. Miller, and A. N. Garroway, *Journal of Magnetic Resonance* **90** 205-13 (1990).

[8] Line-Narrowing Approaches To Solid-State NMR Imaging Pulsed Gradients and 2nd Averaging

J. B. Miller, D. G. Cory, and A. N. Garroway, *Philosophical Transactions of the Royal Society of London Series a Physical Science and Engineering* **333** 413-26 (1990).

[9] Imaging of Solids with RF-Gradients and Line-Narrowing

M. H. Werner, T. J. Lenosky, D. N. Shykind, and D. P. Weitekamp, 31st Experimental Nuclear Magnetic Resonance Spectroscopy Conference, Pacific Grove, CA (April 1-5, 1990).

[10] NMR Imaging of Solids with Multiple-Pulse Line Narrowing and Radiofrequency Gradients,

M. H. Werner, Ph.D. Thesis, Department of Chemistry, California Institute of Technology, Pasadena, CA (1993).

[11] *Advances in Multiple-Pulse Radio-Frequency-Gradient Imaging of Solids*

J. A. Marohn, D. N. Shykind, M. H. Werner, and D. P. Weitekamp, in Review of Progress in Quantitative Nondestructive Evaluation, edited by D. O. Thomson and D. E. Chimenti, Plenum Corporation, New York (1993), Vol. 12A, p. 687-94.

[12] *Rotating Frame Zeugmatography*

D. I. Hoult, *Journal of Magnetic Resonance* **33** 183-97 (1979).

[13] *High Resolution NMR in Solids: Selective Averaging*

U. Haeberlen, in Advances in Magnetic Resonance, edited by J. S. Waugh, Academic Press, New York, NY (1976).

[14] Principles of High Resolution NMR in Solids, 2nd Edition

M. Mehring, Springer-Verlag, Berlin Heidelberg (1983).

[15] Radio Engineers Handbook,

F. E. Terman, McGraw-Hill Book Company, Inc., New York (1943).

[16] *Nutation Sequences for Magnetic Resonance Imaging in Solids*

H. M. Cho, C. J. Lee, D. N. Shykind, and D. P. Weitekamp, *Physical Review Letters* **55** 1923 (1985).

[17] *Analysis of Multiple Pulse NMR in Solids. III*

D. P. Burum and W.-K. Rhim, *The Journal of Chemical Physics* **71** 944-56 (1979).

[18] *On the Exponential Solution of Differential Equations for a Linear Operator*

W. Magnus, *Communications on Pure and Applied Mathematics* **7** 649-93 (1954).

[19] Nuclear Magnetic Resonance Spectroscopy,

R. K. Harris, John Wiley and Sons, Inc., New York (1986).

[20] *High Resolution NMR in Solids*

P. Mansfield, *Physics Letters* **32A** 485-6 (1970).

[21] *A New Method For the Decoupling of Multiple-Coil NMR Probes*

A. Haase, *Journal of Magnetic Resonance* **61** 130-6 (1985).

[22] *Elimination of Coupling Between Cylindrical Transmit Coils and Surface-Receive Coils for InVivo NMR*

M. R. Bendall, A. Connelly, and J. M. Mckendry, *Magnetic Resonance in Medicine* **3** 157-63 (1986).

[23] *Active Detune Switch for Complete Sensitive-Volume Localization in in Vivo Spectroscopy Using Multiple rf Coils and Depth Pulses*

M. R. Bendall, J. M. Mckendry, I. D. Cresshull, and R. J. Ordridge, *Journal of Magnetic* **60** 473-8 (1984).

[24] *An Efficient Technique For Decoupling NMR Transmit Coils From Surface-Coil Receivers*

L. M. Li and C. H. Sotak, *Journal of Magnetic Resonance* **93** 207-13 (1991).

[25] *Electronic Decoupling of Surface-Coil Receivers for NMR Imaging and Spectroscopy*

W. A. Edelstein, C. J. Hardy, and O. M. Mueller, *Journal of Magnetic Resonance* **67** 156-61 (1986).

[26] *Overcoupling NMR Probes to Improve Transient Response*

G. C. Chingas, *Journal of Magnetic Resonance* **54** 153-7 (1983).

[27] *Observation of the Transverse Stern-Gerlach Effect in Neutral Potassium*

M. Bloom, E. Enga, and H. Lew, *Canadian Journal of Physics* **45** 1481-95 (1967).

[28] *On the Use of a Quadrupole Coil for NMR Spin-Echo Diffusion Studies*

G. Odberg and L. Odberg, *Journal of Magnetic Resonance* **16** 342-7 (1974).

[29] *Analysis of Multiple Pulse NMR in Solids. II*

W.-K. Rhim, D. D. Elleman, L. B. Schreiber, and R. W. Vaughan, *The Journal of Chemical Physics* **60** 4595-604 (1974).

[30] *NMR Fourier Zeugmatography*

A. Kumar, D. Welti, and R. Ernst, *Journal of Magnetic Resonance* **18** 69-83 (1975).

[31] Principles of Nuclear Magnetic Resonance in One and Two Dimensions.

R. R. Ernst, G. Bodenhausen, and A. Wokaun, Oxford University Press, New York (1987).

Chapter 3: Decoupling Two Isoresonant Radiofrequency Coils by Active Q-Spoiling

I Abstract

We detail a method for decoupling two high- Q high-power iso-resonant circuits applicable if each circuit may operate in a distinct time interval. Independent excitation of each circuit is made possible by transiently overcoupling the neighboring circuit to its transmission line, spoiling its Q and thereby mitigating the effects of capacitive and inductive inter-circuit coupling. Transient overcoupling entails adding PIN diodes in series to ground with the matching capacitors of series-tuned NMR coils and constructing suitable diode drivers. The protocol demonstrably decouples a 200 MHz high- Q solenoid from a nearby quadrupole gradient coil, enabling realization of a proposal for multiple-pulse rf-gradient imaging of solids.

II Introduction

Any NMR experiment that requires two high- Q isoiresonant rf coils operating in close proximity must contend with capacitive and inductive inter-coil coupling. The coupling shifts the resonances and lowers the Q of both associated circuits, and frustrates pulsing the coils independently [1]. FIG. 1(a) illustrates the effect of intercoil coupling between a solenoid and quadrupole gradient coil.

Inductive coupling may in principle be removed by orienting the coils so that their fields are orthogonal. Residual capacitive coupling may be minimized by reducing the size of one coil, but this effectively reduces the filling factor of the other coil [2]. If each coil may operate in a distinct time interval, other decoupling schemes can be employed. Passive self Q -switching decoupling strategies rely on $\lambda/4$ lines [3] or non-linear circuit elements — such as diodes [4] — which compromise either the circuits' Q , response time, or both. Previous active transmit-coil decoupling schemes using slow magnetic relays [5] or high- Q PIN diodes had acceptable time response (μsec), but operated only at low power [6, 7].

We demonstrate a method of *active high-power* Q -switching which eliminates coupling between isoiresonant coils [8-10]. *Passive* overcoupling, which lowers Q and improves an NMR probe's transient response, is well known [11]. FIG. 1(b) illustrates that the proposed Q -switching can mitigate the effects of intercoil coupling exhibited in FIG. 1(a).

III Pulsed Overcoupling

FIG. 2 presents a related set of coils to be decoupled to implement line-narrowing rf-gradient imaging of solids [12]. A solenoid delivers a 16-pulse line-narrowing sequence of resonant magnetic field pulses to the sample while the quadrupole gradient coil delivers resonant magnetic field gradient pulses in the windows of the line-narrowing sequence, encoding spatial information in two dimensions with a single gradient coil [9, 10]. Both coils are series tuned to 200 MHz and parallel matched to $50\ \Omega$ in the usual way [13]. FIG. 3 illustrates the associated probe circuit.

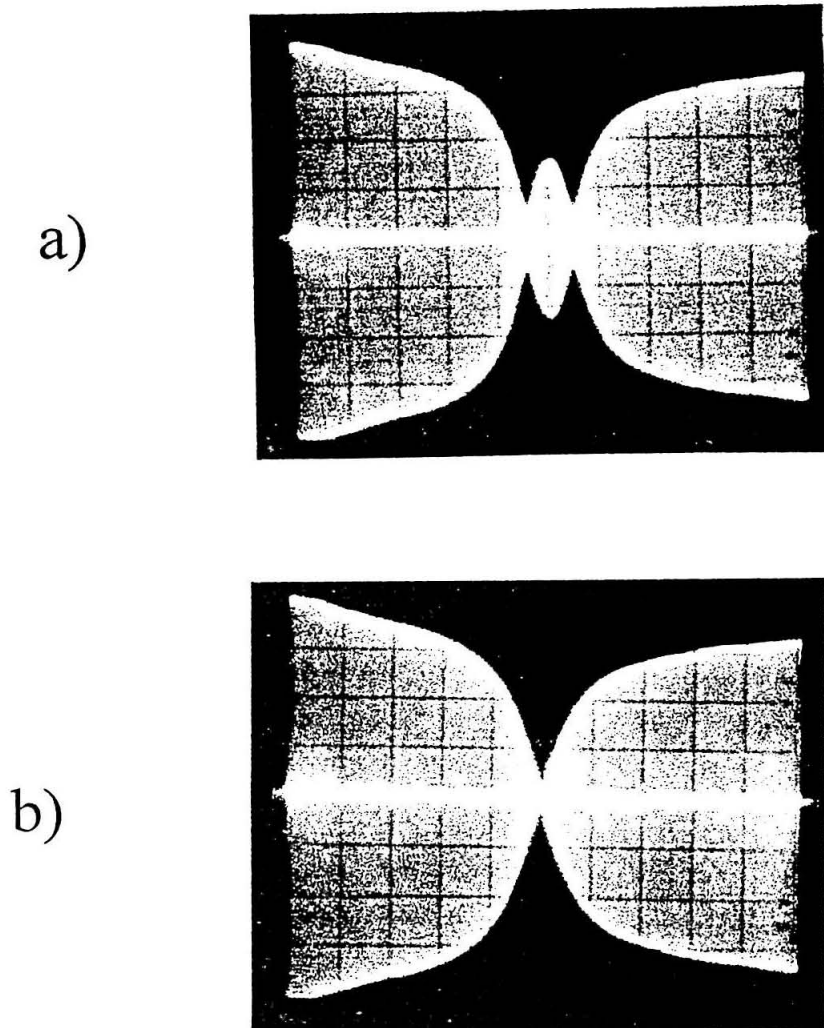


FIG. 1. Reflected voltage from solenoid strongly coupled to, then decoupled from, an adjacent iso-resonant gradient coil.

(a) Reflected voltage versus frequency from a solenoid (8 turns of approximately 2 mm copper strip, 8 mm inner diameter, 25 mm long) centered in a horizontal 4-wire quadrupole gradient coil (no. 16 copper, 28 mm diameter, 45 mm in length). Both coils are series-tuned to 200 MHz and parallel-matched to 50Ω . The reflected voltage shows two dips split by 5 MHz. This bi-resonant behavior is attributable to intercoil coupling, and indicates that it would be impossible to drive the coils independently. (b) The reflected voltage versus frequency of the solenoid returns to that expected for a single tuned and matched circuit if intercoil coupling is mitigated by actively Q -spoiling the adjacent quadrupole-coil circuit.

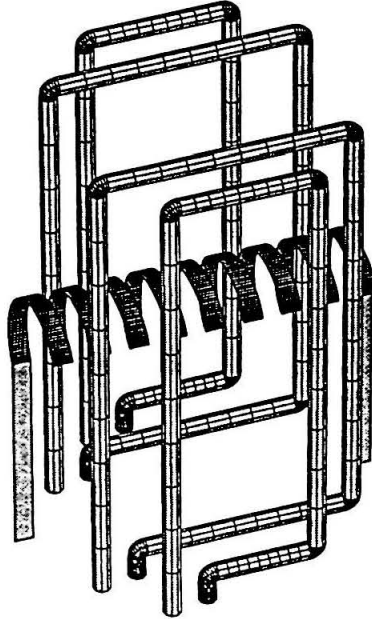


FIG. 2. Homogeneous solenoid and quadrupole gradient coils to be decoupled.

Geometry of a solenoid coil (9 turns of approximately 1.5 mm copper strip, 5.2 mm ID, 26 mm long) and an 8-wire approximation to a quadrupole-gradient coil (no. 16 copper, 20 mm diameter, 35 mm high) prescribed by the desired line-narrowing rf-gradient solids imaging protocol.

Strong coupling between the solenoid and gradient coils seems to preclude pulsing each coil separately. Water magnetization from two capillary tubes placed side-by-side in the solenoid nutates at one well-defined frequency, indicating high rf homogeneity for the bare solenoid. In the presence of an isoresonant horizontal 4-wire quadrupole coil, however, nutation of water magnetization by the solenoid occurs now at two frequencies, indicating that the solenoid drives the quadrupole gradient coil during nutation. More seriously, the quadrupole coil drives the solenoid. In multiple-pulse rf-gradient imaging experiments, as the gradient was increased, the proximate effect was not to spread the image across a larger bandwidth (increasing resolution) but to move the center frequency of the image. This can only be explained by the gradient pulses also producing homogeneous solenoid pulses through intercoil coupling.

Because the solenoid and quadrupole coil are to deliver magnetic field pulses at different times, the deleterious effects of intercircuit coupling may be mitigated through transient Q -spoiling. Q -spoiling is accomplished by placing PIN diodes between the matching capacitor in each circuit, C_M , and ground. See FIG. 3. Under forward bias, the PIN diode behaves as a small resistance in series with C_M and the high- Q circuit operates as usual [14]. Under reverse bias, however, the diode behaves at rf frequencies as a ~ 0.2 pF capacitor which, in series with C_M , serves to overcouple the circuit to its transmission line, spoiling its Q . See FIG. 3.

This strategy was first used to Q -spoil the bare solenoid circuit alone under low-power continuous-wave excitation. The reflected voltage from the probe was observed while a train of DC forward bias pulses ($V_{\text{FOR}} = 10$ V, $I_{\text{FOR}} = 125$ mA through 40Ω) were applied to the PIN diodes. The turn-on time, measured as the time from the beginning of the bias pulse to when the observed reflected voltage had reached $\sim 95\%$ of its well-matched (near zero) value, was 600 ns. Turn-off time, similarly defined, was 11 μ s for no reverse bias ($V_{\text{REV}} = 0$) and an acceptable 700 ns for moderate reverse bias ($V_{\text{REV}} = -25$ V).

This Q -spoiling scheme works under high-power excitation as well. For the diode to remain conducting during rf pulses, the amount of stored charge supplied by the DC bias current I_{FOR} must be greater than charge variations produced by any rf current I_{RF} [16]. This requires that

$$I_{\text{FOR}} \tau \gg \frac{I_{\text{RF}}}{2\pi f}, \quad (1)$$

where τ is the diode's carrier lifetime and f is the rf frequency. For $\tau = 1 \mu$ s, $f = 200$ MHz, and $I_{\text{FOR}} = 125$ mA, the maximum controllable rf current is calculated to be $I_{\text{RF}} = 25$ A. The diode's breakdown voltage ($V_{\text{MAX}} = 500$ V) also constrains the probe's maximum instantaneous power rating P_{MAX} . For the diode placed in the matching arm of the circuit and reversed biased to -25 V, P_{MAX} is 560 W. The observed low-power submicrosecond switching time plus this large estimated diode power rating imply then that Q -spoiling is compatible with the high-power pulses required in multiple-pulse NMR.

Results similar to those of FIG. 1 indicated the efficacy of Q -switching in decoupling line-narrowing and gradient coils under low power excitation. It was next verified that Q -spoiling in fact

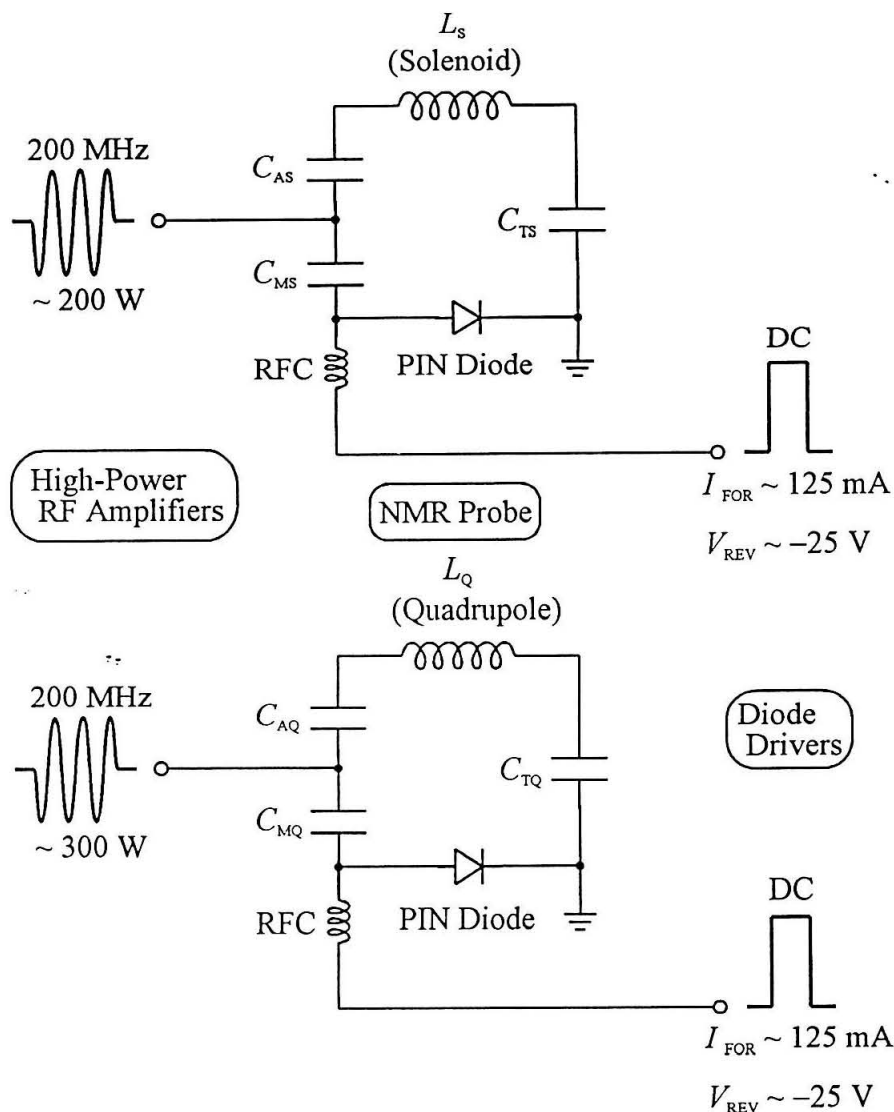


FIG. 3. Tuned circuits associated with FIG. 2 coils.

Capacitors values: $C_{TS} = C_{TQ} = 0.8$ - 10 pF variable (Polyflon NRP-VC-10-12-36 series non-magnetic precision trimmer capacitor, peak working voltage $V_{peak} = 6$ kV); $C_{AS} = 3, 10,$ and 10 pF fixed in series (Centralab series 850 ceramic, $V_{peak} = 5$ kV), $C_{AQ} = 10$ pF fixed (Centralab series 850 ceramic, $V_{peak} = 5$ kV), and $C_{MS} = C_{MQ} = 2$ - 120 pF variable (Voltronics NMTM120CE non-magnetic precision trimmer capacitor, $V_{peak} = 1$ kV). The solenoid-circuit quality factor was ~ 75 . Addition of a PIN diode (actually two heat-sunk M/A-COM MA4P504 PIN diodes) between the matching capacitor and ground enables transient Q -spoiling of each circuit. Radiofrequency choke RFC (~ 1 - 2 μ H, 20 turns, no. 28 copper, 0.68" long, on 1/4" Teflon according to [15]) isolates the diode driver circuitry from high-power rf present in the probe.

decouples the coils under high-power excitation. With the nearby quadrupole coil Q -spoiled (diodes biased $V_{\text{REV}} = -25$ V), the forward-to-reflected voltage ratio for a train of 3 μs 300 W pulses (duty cycle $\sim 1\%$) to the solenoid was greater than 10:1, where with diodes were biased $V_{\text{FOR}} = 10$ V starting 1 μs before and ending with the pulse. Under these conditions, the solenoid coil is easily independently tuned and matched by minimizing reflected power (similar behavior was observed exciting the quadrupole coil), indicating that high-power decoupling has been achieved. Each coil may now be driven independently with the requirement that each coil may not operate at the same time.

Both one-pulse and line-narrowed spectra of adamantane were collected using the solenoid as transmit and receive coil. For an adamantane cylinder 2.3 mm diameter by 6.5 mm long, line narrowing to less than 100 Hz was achieved with a 16-pulse sequence [10] ($\tau_{90} = 3.1$ μs and $\tau_C = 304.8$ μs). In these experiments, the solenoid circuit was held Q -spoiled in the windows of the multiple-pulse sequence when not receiving, as would be required to allow gradient pulses in an imaging experiment. Accounting for filling factor, Q , and coil volume [2], these spectra are identical to those obtained with a conventional single-coil probe on the same spectrometer. Q -spoiling introduces no noise.

The full power of Q -switching in decoupling two isoresonant circuits has been exhibited by successful demonstration of line-narrowing rf-gradient solid-state imaging, reported elsewhere [9, 10]. One motivation for imaging with rf-gradients is that the circuitry for creating rf (gradient) pulses is already part of many spectrometers. As described so far, an rf gradient coil could be added to an existing homogeneous-coil probe, if PIN diodes are added to both coil's circuits for Q -switching. It remains to discuss the requisite diode driver circuitry.

IV Diode Driver Circuit

The diode driver circuit is shown in FIG. 4. Each pair of diodes is driven by two field effect transistors (FETs). Q1 forward biases the diode through a 40 Ω current-limiting resistor, while Q2 is the reverse-biasing switch. Any diode driver has to accommodate the diodes' variable resistance versus voltage. If the diodes are to be grounded as indicated in the probe, then the voltage at the FETs' source

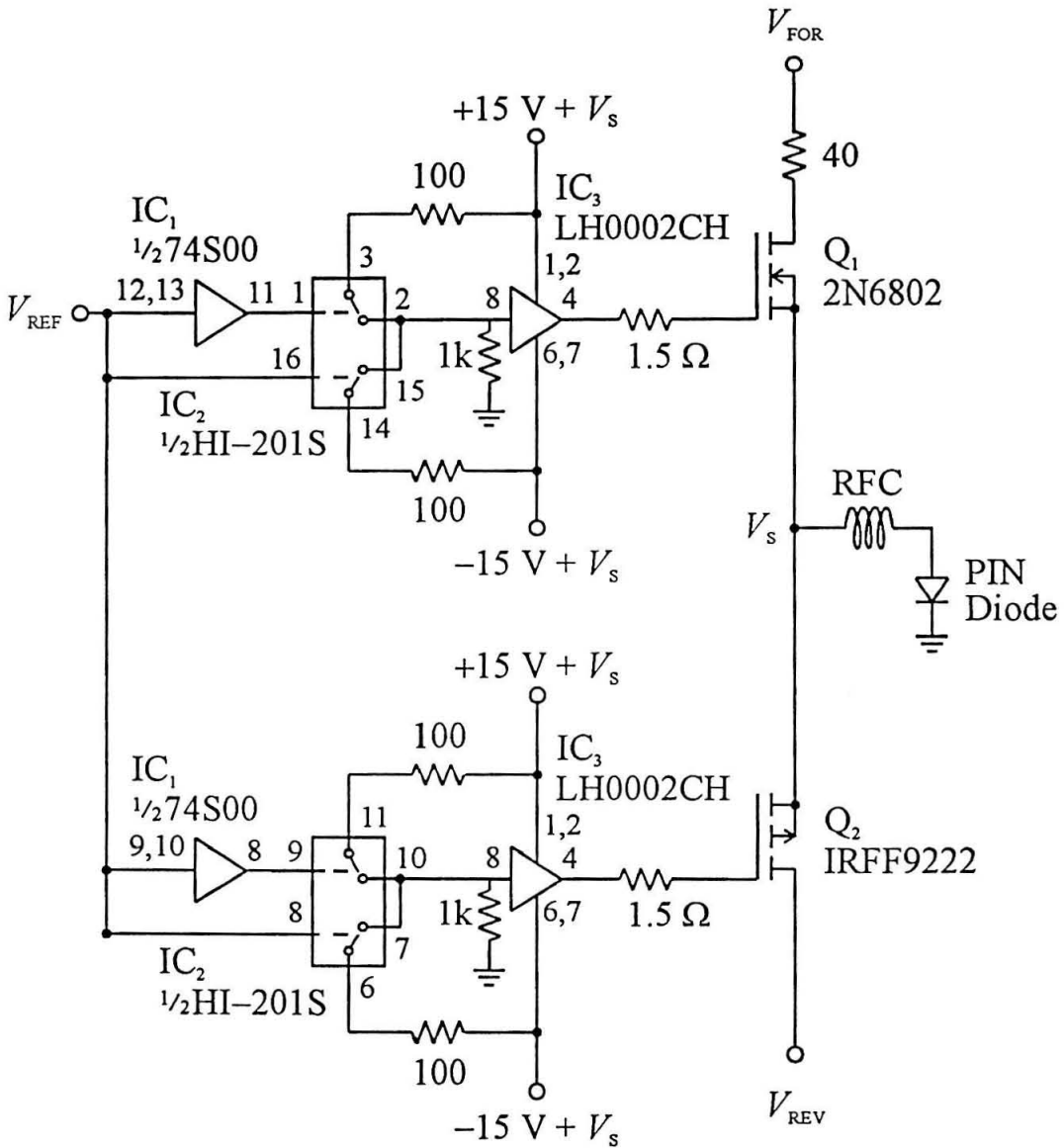


FIG. 4. Bipolar PIN diode driver.

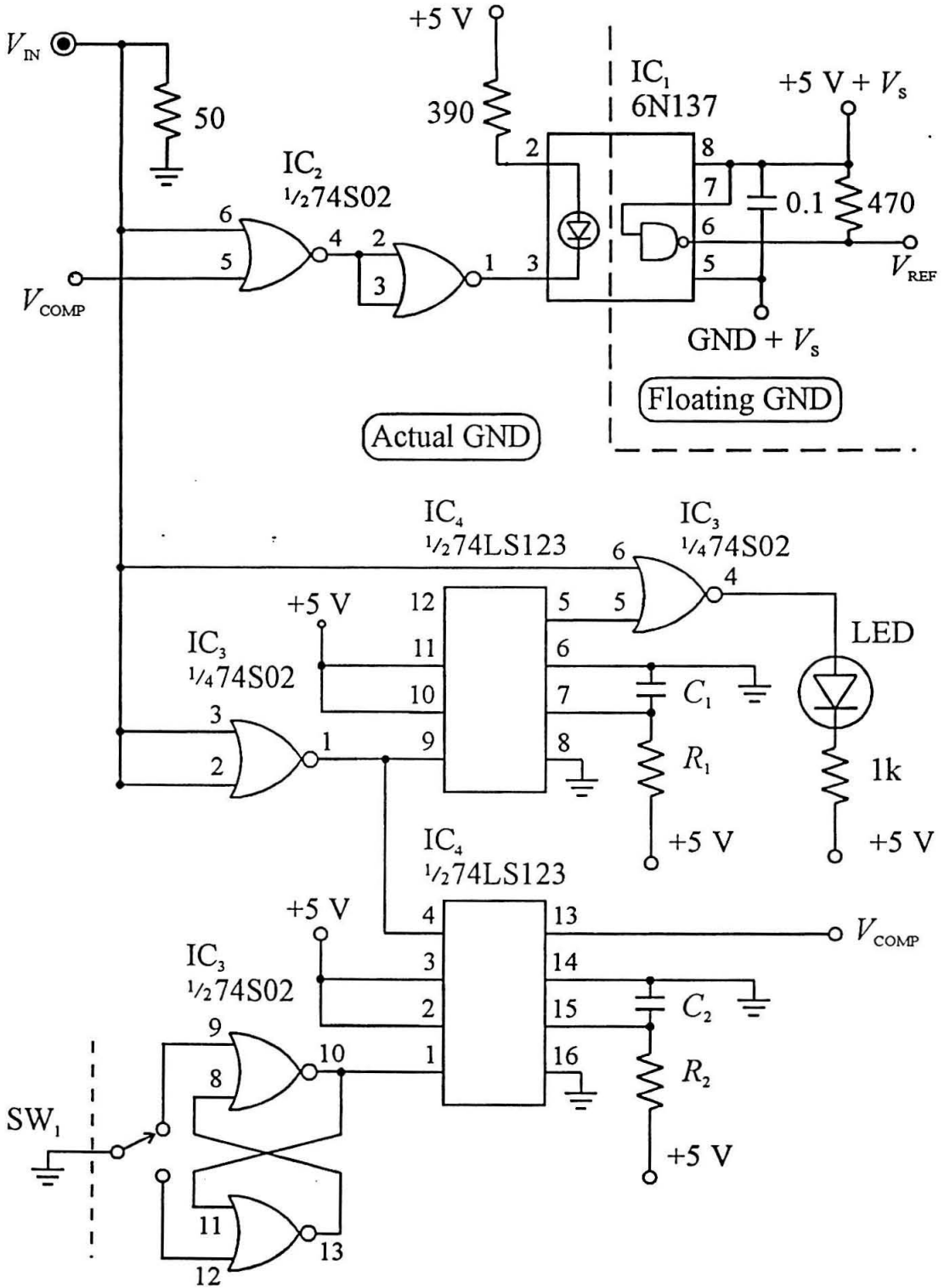


FIG. 5. Optoisolator circuit for bipolar PIN diode driver.

terminals V_S necessarily spikes as the diodes switch on and off. For the diodes to remain biased during this spike, the FETs' gates — and their associated driving circuitry — must float with respect to this source voltage.

Q1 and Q2's switching is triggered by a TTL reference voltage V_{REF} (also referenced to V_S) from another board. Consider biasing Q1's gate. The reference voltage is divided, and one copy inverted by the IC₁ NAND gate. The resulting two voltages drive the fast switch, IC₂, the result of which is to send (current buffered through IC₃) either +15 V (gate open) or -15 V (gate closed) to the gate of the p-channel enhancement-mode transistor Q1 depending on the polarity of V_{REF} . An identical circuit generates a gate voltage from V_{REF} for the n-channel transistor Q2, with a complimentary result: +15 V (gate closed) or -15 V (gate open).

The TTL reference voltage V_{REF} is triggered by a 50- Ω -terminated BNC input V_{IN} . See FIG. 5. The input is first NOR'ed with a comparison voltage V_{COMP} (to be described shortly) to determine whether to trigger. The result is buffered, and sent on to an optical isolator, which allows the TTL triggering voltage to be ground-referenced on the front panel yet V_S -referenced following. The diode driver may also be given a $R_2C_2 \approx 100 \mu\text{s}$ trigger by pressing a front panel switch SW₁ which DC trips a retriggerable monostable multivibrator IC₄ setting V_{COMP} . Each triggering with an external voltage pulse or by front-panel switch results in activation of a front-panel light LED for $R_1C_1 \approx 40 \text{ ms}$.

Two diode-driver prototypes were assembled on home-etched copper-clad circuit board. Each IC chip's voltage supply is high-passed to ground with a 0.47 μF and a 0.01 μF ceramic capacitor at the chip. The FETs Q1 and Q2 were mounted below board with the rest of the circuit above. A generous expanse of ground plane separating the FETs from nearby components is desirable to prevent pickup of voltage arising from the large E-fields generated near the FET's capacitive gate in fast-switching applications.

V Conclusions

A protocol for decoupling two 200 MHz NMR coils has been detailed. The method appears unique in its ability to actively mitigate intercoil coupling in a high-power NMR probe by Q -switching on

a microsecond time scale, enabling independent excitation of solenoid and quadrupole coils in a multiple-pulse rf-gradient imaging experiment. The method might also be employed to decouple transmit and receive coils in conventional liquids magnetic resonance imaging, or to Q-switch a single coil to frustrate radiation damping in a high-Q liquids-NMR probe.

VI Acknowledgments

The author thanks S. W. Sinton and J. H. Iwamiya for advice on implementing NMR imaging on a Bruker MSL-200 spectrometer. This work was supported by grants from Lockheed Missiles and Space Company Incorporated and the National Science Foundation (CHE-9005964).

VII References

[1] Radio Engineers Handbook,

F. E. Terman, McGraw-Hill Book Company, Inc., New York (1943).

[2] Principles of Nuclear Magnetism,

A. Abragam, Clarendon Press, Oxford (1961).

[3] *A New Method For the Decoupling of Multiple-Coil NMR Probes*

A. Haase, Journal of Magnetic Resonance **61** 130-6 (1985).

[4] *Elimination of Coupling Between Cylindrical Transmit Coils and Surface-Receive Coils for in Vivo NMR*

M. R. Bendall, A. Connelly, and J. M. Mckendry, Magnetic Resonance in Medicine **3** 157-63 (1986).

[5] *Active Detune Switch for Complete Sensitive-Volume Localization in Vivo Spectroscopy Using Multiple rf Coils and Depth Pulses*

M. R. Bendall, J. M. Mckendry, I. D. Cresshull, and R. J. Ordridge, Journal of Magnetic **60** 473-8 (1984).

[6] *Electronic Decoupling of Surface-Coil Receivers for NMR Imaging and Spectroscopy*

W. A. Edelstein, C. J. Hardy, and O. M. Mueller, Journal of Magnetic Resonance **67** 156-61 (1986).

[7] *An Efficient Technique For Decoupling NMR Transmit Coils From Surface-Coil Receivers*

L. M. Li and C. H. Sotak, Journal of Magnetic Resonance **93** 207-13 (1991).

[8] *Imaging of Solids with RF-Gradients and Line-Narrowing*

M. H. Werner, T. J. Lenosky, D. N. Shykind, and D. P. Weitekamp, 31st Experimental Nuclear Magnetic Resonance Spectroscopy Conference, Pacific Grove, CA (April 1-5, 1990).

[9] NMR Imaging of Solids with Multiple-Pulse Line Narrowing and Radiofrequency Gradients,

M. H. Werner, Ph.D. Thesis, Department of Chemistry, California Institute of Technology, Pasadena, CA (1993).

[10] *Advances in Multiple-Pulse Radio-Frequency-Gradient Imaging of Solids*

J. A. Marohn, D. N. Shykind, M. H. Werner, and D. P. Weitekamp, in Review of Progress in Quantitative Nondestructive Evaluation, edited by D. O. Thomson and D. E. Chimenti, Plenum Corporation, New York (1993), Vol. 12A, p. 687-94.

[11] *Overcoupling NMR Probes to Improve Transient Response*

G. C. Chingas, *Journal of Magnetic Resonance* **54** 153-7 (1983).

[12] *Nutation Sequences for Magnetic Resonance Imaging in Solids*

H. M. Cho, C. J. Lee, D. N. Shykind, and D. P. Weitekamp, *Physical Review Letters* **55** 1923 (1985).

[13] Experimental Pulse NMR: A Nuts and Bolts Approach,

E. Fukushima and S. B. W. Roeder, Addison-Wesley Publishing Company, Inc., Reading, Massachusetts (1981).

[14] *Applications of PIN Diodes*

Hewlett Packard publication AN922.

[15] The Radio Amateur's Handbook,

G. L. Hall, Ed. , American Radio Relay League, Newington, CT (1984).

[16] *Design with PIN Diodes*

G. Hiller, M/A-COM Semiconductor Products Division publication AG312.

Chapter 4: The Foundations of Optical Nuclear Magnetic Resonance in Semiconductors

I Abstract

This chapter reviews the processes enabling optical detection of nuclear magnetic resonance in semiconductors. Critical to the success of optical NMR is angular momentum transfer between photons, photoexcited conduction-band electron spins, and nuclear spins. The transfer of photon angular momentum to photocarrier electron spin demands favorable selection rules governing optical absorption. Selection rules also allow luminescence polarization to report on recombination-electron spin state. Thus, given a hyperfine interaction of these electrons with nuclei, changes in nuclear magnetization may be observed as variations in luminescence polarization. A fortuitous consequence of this hyperfine interaction is the transfer of the non-equilibrium electron-spin polarization, created by optical pumping with circularly polarized light, to nuclear spins. Large steady-state nuclear magnetization may be obtained in a few seconds through optical pumping. The chapter closes with an experimental demonstration of ultrasensitive optical detection of nuclear magnetic resonance in a gallium arsenide device, and motivates the need for improvements in optical detection protocol required to make the method consistent with modern high-field multiple-pulse NMR.

II Introduction

Photoelectron-induced dynamic nuclear polarization was first observed by Lampel in ^{29}Si [1]. After 22 hours of optically pumping bulk silicon at 77 K, he achieved a record nuclear spin polarization of $\langle I_z \rangle = 2 \times 10^{-6}$. In direct-gap semiconductors at low temperature, where (per photon) optical absorption leads to far more photocarriers, and in cases where the electron spin T_1 's are much longer than the luminescence lifetime, this process is dramatically more efficient [2]. Overhauser-enhanced nuclear spin polarizations of $\langle I_z \rangle \sim 0.1$ can be achieved after only 5 seconds of laser irradiation of GaAs at 2 K [3]. In many direct-gap semiconductors, the resulting large nuclear fields couple strongly to recombination electrons, allowing optical detection of nuclear magnetic resonance.

Two groups, one at the A.F. Ioffe Physico-technical Institute in St. Petersburg and the other at the Ecole Polytechnique in Paris, pioneered studies of optical pumping and optical detection of nuclear magnetization in GaAs [4-15]. This chapter reviews concepts derived in their work, most importantly, the notion of the electron and nuclear hyperfine fields, which underlies all descriptions of optical detection of NMR in semiconductors. Also reviewed is a general treatment of Overhauser enhancement of nuclear magnetization, which is obtained in GaAs via hyperfine coupling to a nonequilibrium electron spin population. Finally, these concepts are brought to bear in introducing the Hanle-effect depolarization of luminescence by nuclear fields, the most successful means of optically detecting NMR in GaAs.

III Selection Rules for Optical Absorption and Emission in Gallium Arsenide

The band structure for GaAs [16-19] is sketched in FIG. 1. The $k = 0$ wavefunctions consist of a $J = 1/2$ conduction band, degenerate $J = 3/2$ heavy-hole and light-hole states, and a $J = 1/2$ split-off band. The dipole-allowed selection rules governing absorption of circularly polarized light [8] are summarized in FIG. 2. One consequence of these selection rules is that absorption of near band-gap circularly-polarized light creates an excess of either spin-up or spin-down conduction-band electrons. The net spin polarization of such conduction-band electrons is described by the vector

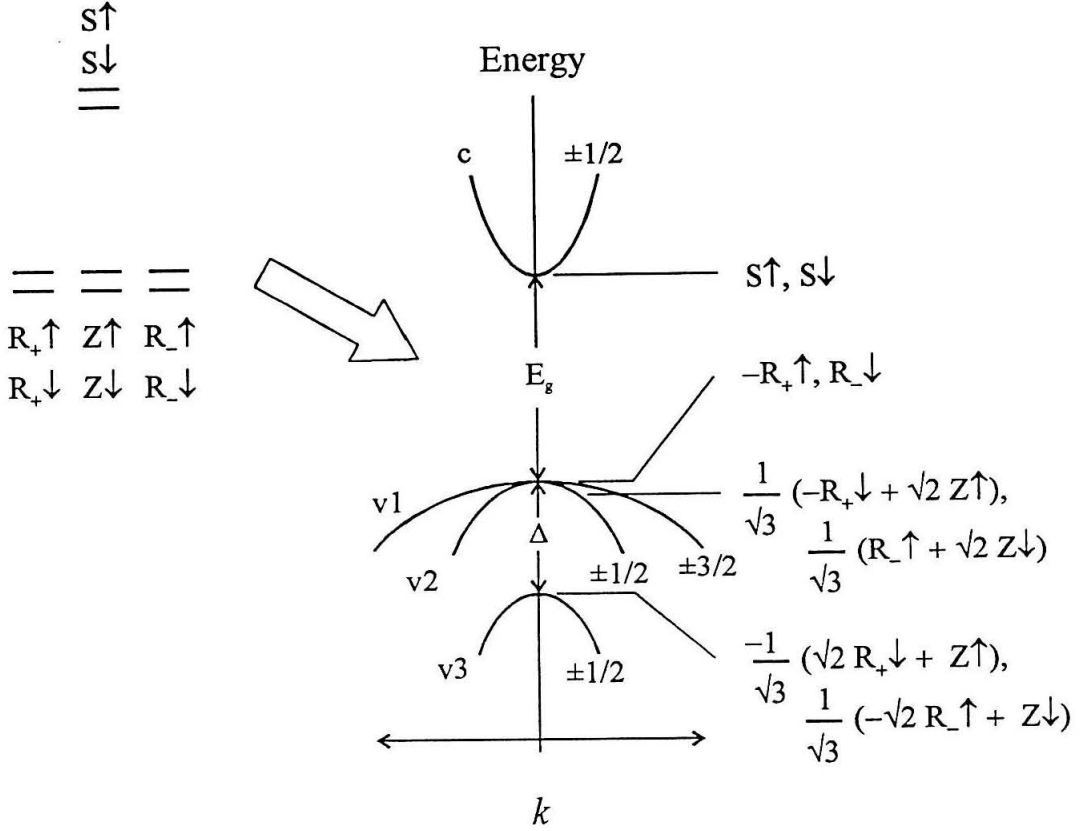


FIG. 1. Electronic energy levels and wavefunctions in GaAs.

Left: Energy diagram for symmetry- and spin-labeled $k = 0$ lattice-periodic one-electron orbitals in the limit of zero spin-orbit interaction. The conduction band in this case is built from $L = 0$ spin-up and spin-down states, $S\uparrow$ and $S\downarrow$. The valence band is built similarly from $L = 1$ spin-up and spin-down states. With $R_{\pm} \equiv (X \pm iY) / \sqrt{2}$, these are $R_{\pm}\uparrow$, $R_{\pm}\downarrow$, $Z\uparrow$, and $Z\downarrow$. Right: Energy versus wavenumber for symmetry-adapted wavefunctions with finite spin-orbit interaction. As in molecular systems, $J = L + S$ commutes with the spin-orbit interaction, meaning (J, m_J) are good wave-function quantum numbers. In the figure, c denotes a $(1/2, 1/2)$ conduction band, $v1$, a $(3/2, 3/2)$ heavy-hole band, $v2$, a $(3/2, 1/2)$ light-hole band, and $v3$, a $(1/2, 1/2)$ split-off band. The $k = 0$ wavefunctions for each band are indicated, as are the 0 K bandgap $E_g = 1.52$ eV, and the spin-orbit splitting $\Delta_{SO} = 0.30$ eV.

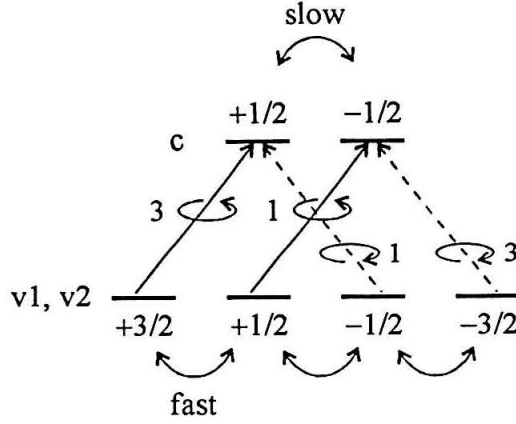


FIG. 2. Selection rules for near band-edge absorption of circularly-polarized light in GaAs. Matrix elements for absorption of σ^+ light (right-handed arrow, solid lines) and σ^- light (left-handed arrows, dashed lines) from the $J = 3/2$ valence-band states to the conduction band are indicated. At 2 K, slow interconversion of conduction-band spin states allows a spin-excess of conduction-band electrons to be established by optical pumping.

$$P_e \equiv \frac{n_\uparrow - n_\downarrow}{n_\uparrow + n_\downarrow} \mathbf{n}_E \quad (1)$$

where n_\uparrow and n_\downarrow are the number of spin-up and spin-down conduction band electrons, respectively, and \mathbf{n}_E is a unit vector along the direction of excitation. For electrons created immediately after optical pumping with σ^+ light (i.e., where the electric field vector rotates clockwise about the direction of propagation), selection rules demand that $P_e = 1/2$. In zero magnetic field the expectation value of the angular momentum of these conduction-electrons, also parallel to the exciting light in zero magnetic field, is

$$\mathbf{S} = \frac{n_\uparrow}{n_\uparrow + n_\downarrow} \left(\frac{1}{2}\right) + \frac{n_\downarrow}{n_\uparrow + n_\downarrow} \left(-\frac{1}{2}\right) = \frac{1}{2} P_e . \quad (2)$$

Conduction-band electrons created immediately after absorption have $\langle S \rangle = 1/4$ along the direction of photon propagation. This value is reduced in steady-state by competition between recombination (at rate $1/\tau$) and electron spin-relaxation (rate $1/\tau_s$). More realistically, at zero magnetic field

$$\mathbf{S} = \frac{1}{2} \frac{\tau_s}{\tau + \tau_s} \mathbf{P}_e . \quad (3)$$

Achieving maximally polarized electrons requires detecting at low temperatures where $\tau_s \gg \tau$.

Selection rules and conservation of angular momentum require that absorption of circularly polarized light also create spin-polarized valence-band states (holes). As this hole polarization is lost rapidly compared to the recombination lifetime of electron-hole pairs [20-22], the polarization of the luminescence in bulk GaAs is determined by the spin of the recombination electron and selection rules alone. The degree of circular polarization of the luminescence is defined as

$$\rho = \frac{I_+ - I_-}{I_+ + I_-} \quad (4)$$

where I_+ and I_- are the number of σ^+ and σ^- photons emitted, respectively. Selection rules predict

$$\rho = -\frac{1}{2} \mathbf{P}_e \cdot \mathbf{n}_D = -\mathbf{S} \cdot \mathbf{n}_D \quad (5)$$

where \mathbf{n}_D is a unit vector describing the direction of observation.

IV The Interaction of Electrons and Nuclei Through Hyperfine Coupling

Relation (5) indicates that the degree of circular polarization of luminescence is proportional to the spin state of the recombination electron. It is the interaction of this electron with nuclei through a hyperfine coupling that allows luminescence polarization to report on nuclear magnetization.

The Fermi-contact hyperfine interaction [23] of nuclei j (gyromagnetic ratio γ_j , spin vector \mathbf{I}_j , located at position \mathbf{r}_j) with a single electron (gyromagnetic ratio γ_e , spin vector \mathbf{S}) at the origin is (in SI units)

$$H_{\text{HF}} = \frac{2}{3} \mu_0 \hbar^2 \gamma_e \sum_j \gamma_j |\psi_e(\mathbf{r}_j)|^2 \mathbf{S} \cdot \mathbf{I}_j , \quad (6)$$

where μ_0 is the magnetic permeability of free space and $\psi_e(\mathbf{r}_j)$ is the electronic wavefunction at the j^{th} nuclear center.

One implication of this hyperfine coupling is that, as a consequence of the electron spending time within nuclei, a given nucleus j experiences an effective field from the electron B_e^j which is

$$B_e^j = -\frac{2}{3} \mu_0 \hbar \gamma_e |\psi_e(r_j)|^2 \langle S \rangle, \quad (7)$$

where the electron spin vector has been replaced by its time average, accounting for recombination and excitation events. In terms of the hyperfine electron field, Eq. (6) may be rewritten as

$$H_{\text{HF}} = -\sum_j \hbar \gamma_j B_e^j \cdot I_j, \quad (8)$$

which makes it clear that B_e^j acts on the nuclei like any magnetic field. When present during the evolution period of an NMR experiment, this field appears as a measurable Knight shift of the nuclear resonance. Paget [10] has made numerical estimates of electron hyperfine fields near shallow donors in GaAs. Near a donor state having occupation probability Γ , and described by a hydrogenic orbital having a Bohr radius a_0 ,

$$B_e^j = \Gamma \langle S \rangle b_e^j(0) \exp(-2r_j / a_0). \quad (9)$$

Here $b_e^j(0) = -(2/3) \mu_0 \gamma_e d_j \Omega / \pi a_0^3$ where Ω is the volume of the unit cell, and d_j is the electron density at each nucleus. Paget takes $\Gamma = 1$ and, taking $a_0 = 10$ nm and using atomic hyperfine constants to estimate d_j , calculates

$$b_e^j(0) = -220 \text{ G}, j = {}^{75}\text{As}. \quad (10)$$

$$b_e^j(0) = -130 \text{ G}, j = {}^{69}\text{Ga}, {}^{71}\text{Ga}. \quad (11)$$

A similar field is felt by the electron. This nuclear hyperfine field is given by

$$B_n = \frac{2}{3} \mu_0 \hbar \sum_j \gamma_j |\psi_e(r_j)|^2 I_j. \quad (12)$$

This is the total nuclear hyperfine field, which may be divided into contributions b_j from each isotope. The hyperfine Hamiltonian, written in terms of the total nuclear hyperfine field, becomes

$$H_{\text{HF}} = \hbar \gamma_e B_n \cdot S, \quad (13)$$

which makes it clear that nuclear hyperfine field acts on the electron also like any magnetic field. Paget has also made an estimate of the nuclear hyperfine fields felt by an electron occupying a shallow donor [10]. Assuming that nuclear spins are equally polarized near the shallow donor, the nuclear hyperfine field is independent of the electron spin state:

$$B_n = b_n \langle I_n \rangle, \quad (14)$$

where the nuclear spin vector has been replaced by its average over the $\sim 10^4$ nuclei contributing to the sum in Eq. (12), and $b_j = (2/3) \gamma_e \gamma_j x_j d_j$, with x_j the fractional concentration of each isotope ($x_j=1$ for $j=^{75}\text{As}$, $x_j=0.6$ for $j=^{69}\text{Ga}$, $x_j=0.4$ for $j=^{71}\text{Ga}$). The estimated contributions to the nuclear hyperfine field are

$$b_j = -18.4 \text{ kG}, j = ^{75}\text{As}, \quad (15)$$

$$b_j = -9.1 \text{ kG}, j = ^{69}\text{Ga}, \text{ and} \quad (16)$$

$$b_j = -7.8 \text{ kG}, j = ^{71}\text{Ga}. \quad (17)$$

The nuclei thus act on the electrons through the hyperfine interaction as a magnetic field of up to a few *Tesla*, which is evident as shifts in conduction-electron spin resonance frequency. A more effective mechanism for B_n to affect S is by the Hanle effect, to be discussed shortly. First, we must consider another consequence of the hyperfine coupling. The coupling mediates the sharing of the large conduction-electron spin polarization created by optical pumping with the nuclei. This is not an increased alignment of the nuclei in the electron hyperfine field, but a dynamic process involving mutual spin flips.

V Optical Nuclear Polarization

The following derivation of the equations describing dynamic nuclear polarization (DNP) of nuclei by electrons follows closely one given by Dyakonov and Perel [8]. Consider that the fluctuating hyperfine interaction causes electron-nuclear spin flips, as illustrated in FIG. 3. Conservation of total spin, satisfied because the hyperfine interaction commutes with total electron-nuclear spin, implies the following balance equation for steady-state population of nuclear-spin level populations N_μ .

$$W_{\mu,\mu-1} N_\mu f_\downarrow = W_{\mu-1,\mu} N_{\mu-1} f_\uparrow, \quad (18)$$

where $f_{\uparrow,\downarrow} = 1/2 \pm \langle S \rangle$ are the fractional populations of the electron spin levels. The transition probabilities W must satisfy detailed balance. If the nuclear spin system is to reach a definite temperature T , then

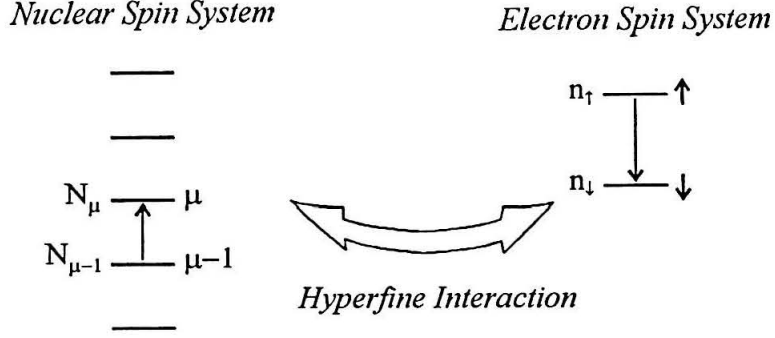


FIG. 3. Dynamic nuclear polarization by hyperfine coupling to out-of-equilibrium electrons. A fluctuating electron-nuclear hyperfine coupling induces mutual spin flips. One such spin flip, driving the electron system from state \uparrow to \downarrow and the nuclear system from state $\mu-1$ to μ , is shown.

$$\frac{W_{\mu,\mu-1}}{W_{\mu-1,\mu}} = \exp\left(-\frac{E}{k_B T}\right), \quad (19)$$

where $E \approx \gamma_e B$ is the energy difference between the two configurations (μ, \uparrow) and $(\mu-1, \downarrow)$. It follows that

$$\frac{N_\mu}{N_{\mu-1}} = \frac{1+2\langle S \rangle}{1-2\langle S \rangle} \exp\left(-\frac{\gamma_e B}{k_B T}\right) \equiv \exp\left(\frac{x}{I}\right), \quad (20)$$

where the variable x is a ratio of Zeeman to thermal energy and I is the nuclear-spin quantum number.

We want to calculate the average nuclear magnetization according to Eq. (21), knowing the ratios of level populations imposed by Eq. (20).

$$\langle I \rangle = \frac{\sum_{\mu=-I}^I \mu N_\mu}{\sum_{\mu=-I}^I N_\mu} \quad (21)$$

From Eq. (20) it follows that

$$\frac{N_\mu}{N_0} = \exp\left(\frac{\mu x}{I}\right), \quad (22)$$

and so Eq. (21) can be rewritten as

$$\langle I \rangle = \frac{I \sum_{\mu=-I}^I \frac{\mu}{I} \exp\left(\frac{\mu x}{I}\right)}{\sum_{\mu=-I}^I \exp\left(\frac{\mu x}{I}\right)} = I \frac{1}{G_I(x)} \frac{\partial}{\partial x} G_I(x), \quad (23)$$

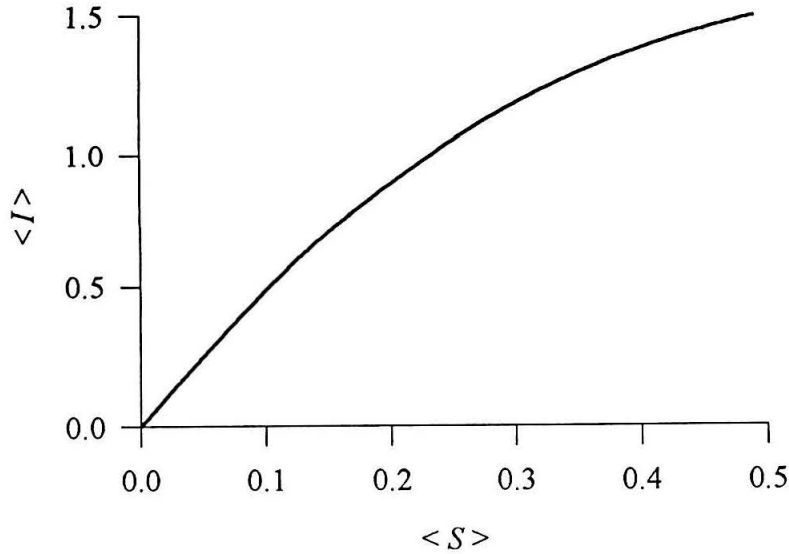


FIG. 4. Maximum achievable dynamic nuclear polarization.

This figure illustrates the average spin $\langle I \rangle$ achievable for a spin $3/2$ nucleus by dynamic nuclear polarization via hyperfine coupling to a spin $\langle S \rangle$ electron.

where

$$G_I(x) \equiv \sum_{\mu=-I}^I \exp\left(\frac{\mu x}{I}\right), \quad (24)$$

is a function depending only on x and I . Series expansion of Eq. (23) in $\langle S \rangle$ near $\langle S \rangle = 0$ and $B = 0$ recovers the oft-quoted result

$$\langle I \rangle = \frac{4}{3} I(I+1) \langle S \rangle, \quad (25)$$

which holds for $\langle S \rangle$ much larger than its thermal value (justifying the approximation $B=0$), but much smaller than its maximum value of $1/2$. The more common DNP, which results from resonant electron spin saturation (i.e., $\langle S \rangle = 0$), also follows from Eq. (23), but is not discussed here.

The average electron spin is oriented along the optical pumping axis. Dynamic nuclear polarization is caused only by the component of \mathbf{S} along the static field \mathbf{B} which orients the nuclei. Vector

generalization of Eq. (25) to the case where the optical orientation and magnetic field axis are not parallel is

$$\langle I \rangle = \frac{4}{3} I(I+1) \frac{(\langle S \rangle \cdot B) B}{B^2}, \quad (26)$$

FIG. 4 plots $\langle I \rangle$ versus $\langle S \rangle$ for the case of optical pumping of a spin 3/2 nucleus by an $S=1/2$ electron, where S and B are taken to be parallel and where $\langle I \rangle$ is given by Eq. (23). Even in the case where nuclear spins in GaAs have achieved $\sim 10\%$ polarization, the value $\langle I \rangle \sim 0.15$ is still in the $\langle I \rangle \ll \langle S \rangle$ regime shown in the figure, indicating that even at these large polarizations Eq. (25) is a good approximation.

Calculation of the rate ($1/T_{1e}$) of polarization transfer from electrons to nuclei through hyperfine coupling requires quantum-mechanical relaxation theory [10, 23]. In the weak-collision limit [23]:

$$\frac{1}{T_{1e}} = \tilde{\omega}^2 \tau_c, \quad (27)$$

where $\tilde{\omega}^2$ is the average of the square of the precession frequency of the nuclei present in the fluctuating field of the electrons, and τ_c is a correlation time for these fluctuations. This equation may be recast in terms of the hyperfine electron field in order to predict the polarization rate for nuclei j at distance r from the center of a donor-state electron

$$\frac{1}{T_{1e}^j(r)} = \Gamma [\gamma_j b_e^j(0)]^2 \tau_c \exp(-4r/a_0). \quad (28)$$

Assuming τ_c in the range 10^{-9} – 10^{-8} and $\Gamma \sim 1$ indicates that $T_{1e}^j(0)$ covers the range 10^{-2} – 10^{-1} .

Taken together, the results of Eqs. (23-26) and (28) predict that near-unity nuclear spin polarization can be created in the vicinity of donor states in GaAs by optical pumping. Even for lightly doped samples, this locally-created nuclear polarization can be shared with bulk nuclei via spin diffusion [23], although this can require many minutes. Polarization can be carried both to and from defect sites [12, 24], so that luminescence originating from electrons located on a defect site (even at sub part-per-million defect concentrations) can report on nuclei from nearly all the sample.

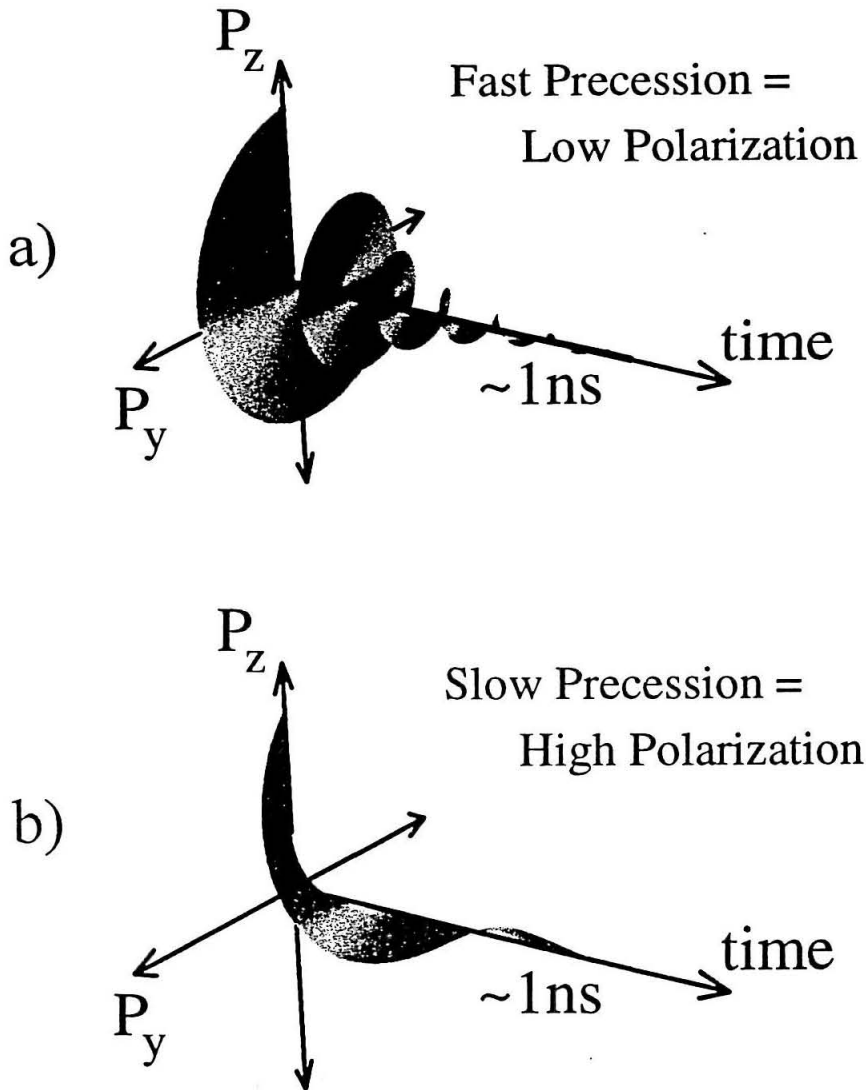


FIG. 5. Time-domain view of the Hanle effect.

A photoexcited electron with spin polarization P_z is created by optically pumping along the z -axis. In the presence of a magnetic field along the x -axis, the spin polarization vector will precess in the y - z plane and dephase in nanoseconds. The figure illustrates the evolution of spin polarization for (a) large transverse magnetic field and (b) small transverse magnetic field. Luminescence polarization ρ measures the time-average component $\langle P_z \rangle$ along the optical detection axis. In case (a), $\langle P_z \rangle \sim 0$ and the luminescence is nearly completely depolarized by the transverse field.

VI The Hanle Effect

The large nuclear fields obtained by optical pumping can result in measurable shifts of the electron precession frequency, which may be monitored by conduction-electron spin resonance (CESR) [25]. Since electron spin polarization is proportional luminescence polarization, optical detection of CESR is one route to ultrasensitive detection of NMR in semiconductors. Unfortunately, this experiment suffers poor sensitivity due to the width of the CESR line ($\sim 1/\tau_S \sim \text{GHz}$).

A more sensitive way to register NMR optically makes use of nuclear magnetization perpendicular to the electron spin axis of interest. Electron spin polarization, initially oriented along the z-axis, precesses in the perpendicular nuclear hyperfine field and dephases before luminescing. If the perpendicular field is large compared to $1/\gamma_e T_{1e}$, (~ 100 Gauss for $T_{1e} \sim \text{ns}$) the dephasing time in magnetic field units, then luminescence is completely depolarized. This non-resonant ‘‘Hanle effect’’ [2, 26, 27] depolarization of luminescence by perpendicular magnetic fields is illustrated schematically in FIG. 5.

In the simplest optical NMR experiment, luminescence polarization is recorded while a transverse radiofrequency field is swept through resonance. Near resonance, nuclear magnetization is deflected into the plane (as in any CW NMR experiment) and, in this experiment, leads to luminescence depolarization by the Hanle effect. An example steady-state NMR spectrum is shown in FIG. 6(a) [28]. While $\sim 10^5$ times more sensitive than conventional detection, steady-state optical NMR gives a spectrum whose line width is ~ 20 times larger than that expected based on spin-spin couplings alone. This is due to the presence of photocarriers during detection, power broadening, and the non-linear nature of the Hanle effect.

Through the use of a transverse reference field, linear response to nuclear fields can be recovered as was done in obtaining the spectrum of FIG. 6(b). In addition, optical pumping, NMR evolution, and optical detection have been executed in distinct time periods and thus may be separately optimized. This introduction of time sequencing [24, 29] to optical NMR resulted in the first-ever optically detected high-resolution NMR spectrum.

The remainder of this thesis describes Larmor beat detection (LBD) [3], an alternative optical detection technique. Unlike time-sequenced NMR, LBD is capable of observing real-time NMR transients

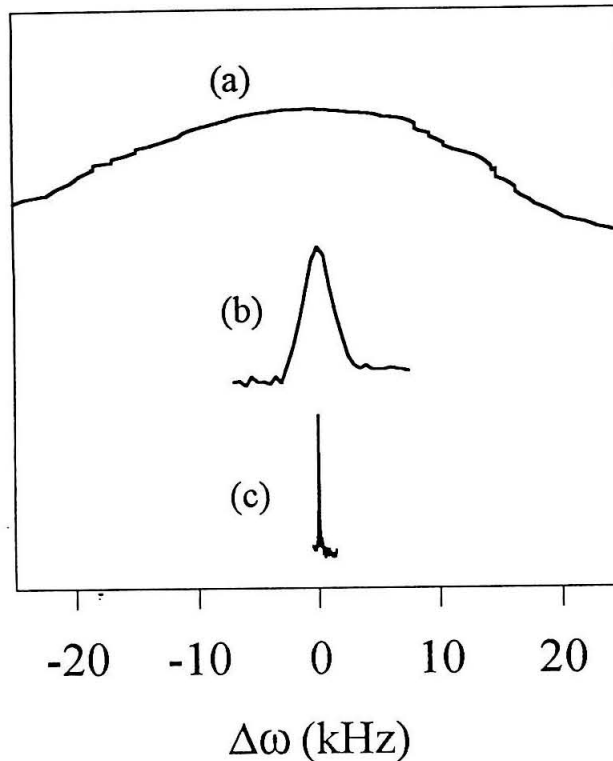


FIG. 6. Optically detected NMR spectra of GaAs.

(a) Steady-state optical detection of ^{69}Ga resonance (A. I. Ekimov and V. I. Safarov, 1972), (b) Time-sequenced Fourier-transform optical NMR of ^{71}Ga (S. K. Buratto, D. N. Shykind, and D. P. Weitekamp, 1991), and (c) ^{71}Ga multiple-pulse line narrowing with Larmor beat detection (J. A. Marohn, P. J. Carson, J. Y. Hwang, M. A. Miller, D. N. Shykind, and D. P. Weitekamp, 1995).

at high magnetic field. This provides the practical advantage that cycling of field orientation is not required, and it makes the method far less susceptible to drift. The resolution obtainable using LBD in concert with multiple-pulse line narrowing techniques at moderate field (~ 0.2 T) is shown in FIG. 6(c). The NMR line shown has a full width at half maximum of < 50 Hz, an improvement by a factor of ~ 50 in resolution compared to simple FT spectra acquired by time-sequencing.

VII References

- [1] *Nuclear Dynamic Polarization by Optical Electronic Saturation and Optical Pumping in Semiconductors*
G. Lampel, Physical Review Letters **20** 491 (1968).
- [2] Optical Orientation,
F. Meier and B. P. Zakharchenya, Eds., Elsevier, Amsterdam (1984).
- [3] *Optical Larmor Beat Detection of High-Resolution Nuclear Magnetic Resonance in a Semiconductor Heterostructure*
J. A. Marohn, P. J. Carson, J. Y. Hwang, M. A. Miller, D. N. Shykind, and D. P. Weitekamp, Physical Review Letters **75** 1364-7 (1995).
- [4] *Spin Orientation of Electrons Associated with the Interband Absorption of Light in Semiconductors*
M. I. Dyakonov and V. I. Perel, Soviet Physics JETP **33** 1053 (1971).
- [5] *Hyperfine Interaction in Optical Orientation of Electrons in Semiconductors*
M. I. Dyakonov and V. I. Perel, Soviet Physics JETP **36** 995 (1973).
- [6] *Optical Orientation in a System of Electrons and Lattice Nuclei in Semiconductors. Theory*
M. I. Dyakonov and V. I. Perel, Soviet Physics-JETP **38** 177 (1974).
- [7] *Optical Effects Due to Polarization of Nuclei in Semiconductors*
M. I. Dyakonov, V. I. Perel, V. L. Berkovits, and V. I. Safarov, Soviet Physics - JETP **40** 950 (1974).
- [8] *Theory of Optical Spin Orientation of Electrons and Nuclei in Semiconductors*
M. I. Dyakonov and V. I. Perel, in Optical Orientation, edited by F. Meier and B. P. Zakharchenya, North-Holland, Amsterdam (1984), p. 11-71.
- [9] *Optical Orientation in a System of Electrons and Lattice Nuclei in Semiconductors. Experiment*
V. L. Berkovits, A. I. Ekimov, and V. I. Safarov, Sov. Phys.-JETP **38** 169 (1974).
- [10] *Low Field Electron-Nuclear Spin Coupling in Gallium Arsenide Under Optical Pumping Conditions*
D. Paget, G. Lampel, B. Sapoval, and V. I. Safarov, Physical Review B **15** 5780 (1977).

[11] *Optical Detection of NMR in High-Purity GaAs Under Optical Pumping: Efficient Spin-Exchange Averaging Between Electronic States*

D. Paget, Physical Review B **24** 3776 (1981).

[12] *Optical Detection of NMR in High-Purity Gaas: Direct Study of the Relaxation of Nuclei Close to Shallow Donors*

D. Paget, Physical Review B **25** 4444 (1982).

[13] *Optical Investigation of Hyperfine Coupling Between Electronic and Nuclear Spins*

D. Paget and B. L. Berkovits, in Optical Orientation, edited by F. Meier and B. P. Zakharchenya, North-Holland, Amsterdam (1984), Vol. 8, p. 173-258.

[14] *Optical Polarization of Nuclei in GaAs/AlGaAs Quantum Well Structures*

V. K. Kalevich, V. L. Korenev, and O. M. Fedorova, JETP Letters **52** 349 (1990).

[15] *Optically Induced NMR In Semiconductors*

V. K. Kalevich, V. L. Korenev, and V. G. Fleisher, Izvest. Akad. Nauk. SSSR. Ser. Fiz. **52** 434 (1988).

[16] *Spin-Orbit Effects in Zinc Blende Structures*

G. Dresselhaus, Physical Review **100** 580-6 (1955).

[17] *Band Structure in Indium Antimonide*

E. O. Kane, Journal of the Physical Chemistry of Solids **1** 249-61 (1957).

[18] Quantum Theory of Solids, 1st Edition

C. Kittel, John Wiley and Sons, Inc., New York (1963).

[19] Physics of III-V Compounds, 1st Edition

O. Madelung, John Wiley and Sons, Inc., New York (1964).

[20] *Spin Relaxation under Optical Orientation in Semiconductors*

G. E. Pikus and A. N. Titkov, in Optical Orientation, edited by F. Meier and B. P. Zakharchenya, North-Holland, Amsterdam (1984), p. 73-131.

[21] *Hole Relaxation and Luminescence Polarization in Doped and Undoped Quantum Wells*

T. Uenoyama and L. J. Sham, Physical Review Letters **64** 3070-3 (1990).

[22] *Spin Relaxation Dynamics in GaAs Quantum Wells: Free Carriers and Excitons*

L. Vina, T. C. Damen, J. E. Cunningham, J. Shah, and L. J. Sham, *Superlattices and Microstructures* **12** 379-86 (1992).

[23] Principles of Nuclear Magnetism, 1st Edition

A. Abragam, Clarendon Press, Oxford (1961).

[24] *Fourier-Transform Time-Sequenced Optical Nuclear Magnetic Resonance of Gallium Arsenide*

S. K. Buratto, J. Y. Hwang, N. D. Kurur, D. N. Shykind, and D. P. Weitekamp, *Bulletin of Magnetic Resonance* **15** 190 (1993).

[25] *Optical Detection of Conduction Electron Spin Resonance in Semiconductors and its Application to $k.p$ Perturbation Theory*

C. Hermann and C. Weisbuch, in Optical Orientation, edited by F. Meier and B. P. Zakharchenya, North-Holland, Amsterdam (1984), p. 11-71.

[26] *Über Magnetische Beeinflussung der Polarization der Resonanzfluoreszenz*

W. Hanle, *Z. Phys.* **30** 93 (1924).

[27] *Band-to-Band Optical Pumping in Solids and Polarized Photoluminescence*

R. R. Parsons, *Physical Review Letters* **23** 1132 (1969).

[28] *Optical Electron-Nuclear Resonance in Semiconductors*

A. I. Ekimov and V. I. Safarov, *JETP Letters* **15** 319 (1972).

[29] *Time-Sequenced Optical Nuclear Magnetic Resonance of Gallium Arsenide*

S. K. Buratto, D. N. Shykind, and D. P. Weitekamp, *Physical Review B* **44** 9035 (1991).

Chapter 5: Optical Detection of Nuclear Magnetic Resonance in III-V Semiconductors

I Abstract

We describe theoretically and demonstrate experimentally Larmor beat detection, a method for optically recording real-time NMR transients from III-V semiconductors. With one nuclear field spin-locked as a reference, it is demonstrated that evolution of the second nuclear field can be recorded as a modulation of luminescence polarization at the Larmor beat frequency. A theoretical treatment is given for the Fourier components of luminescence valid for any value of the two nuclear fields, allowing estimation of linear-response criteria and dynamic range for this nuclear hyperfine field magnetometer. A protocol for encoding precession of a single nuclear field in Larmor-frequency oscillation of luminescence polarization is proposed which could allow real-time optical detection of NMR to be extended to group IV semiconductors.

II Introduction

Optical pumping of semiconductors with circularly polarized light can create a thousand-fold Overhauser-effect enhancement of nuclear magnetization at low temperatures [1, 2]. This dramatic enhancement increases the sensitivity of nuclear magnetic resonance (NMR) enough to probe nuclei near semiconductor interfaces by *conventional* detection at high magnetic field [3-5]. NMR in these systems reports on important material properties: conduction electron polarization and density through the Knight shift [3-8] and through the relaxation time [3-5]; lattice-mismatch [9] and defect-associated strain [10] through electric-field-gradient-induced quadrupole splittings of nuclear magnetic resonances for spins with $I > 1/2$; and, in analogy with bulk studies [11], should even allow quantification of electric fields by measuring an induced electric field gradient. It has been proposed that the isotropic optically induced Knight shift could be used to map the excited-state electronic wavefunction in a quantum well with atomic resolution [12].

While optical detection of NMR in semiconductors provides another crucial orders-of-magnitude sensitivity boost [2, 13], such methods suffered until recently a concomitant loss in needed spectral resolution by encoding NMR nonlinearly in luminescence polarization. The high resolution of conventional NMR may be restored by time-sequencing [6, 10, 12] and separately optimizing periods of optical pumping, NMR evolution, and optical detection. This gain, however, is mitigated by the inconvenience of the requisite field cycling and by a loss in throughput associated with point-wise acquisition of the desired interferogram.

We recently demonstrated a new optical detection method, Larmor beat detection (LBD), which lifts these restrictions and allows for the *real-time* optical detection of NMR transients in semiconductors at fixed magnetic field [14]. In LBD, modulation of the circular polarization of luminescence at the difference between two nuclear spin precession frequencies is induced by rf pulses. One isotope provides a spin-locked reference field, while NMR transients of the second isotope are observed in real time.

This paper presents a detailed look at the theory and motivation for LBD, along with experimental verification of the effect. It is shown that LBD may obtain small-signal sensitivity equivalent

to the best competing method, time-sequenced optical NMR. The theoretical treatment is extended beyond small-signal response, enabling the calculation of a dynamic range estimate for the LBD magnetometer. Finally, a complementary optical detection method is detailed which modulates luminescence polarization at the precession frequency of a single nuclear field, allowing convenient real-time optical detection when two NMR sensitive isotopes are unavailable, as in group-IV semiconductors.

III Equation of Motion for Recombination-Electron Spin Under External and Internal Magnetic Fields

A theoretical description of Larmor beat detection begins with the Bloch equation governing evolution of electron spin polarization \mathbf{S} [2]

$$\frac{d}{dt}\mathbf{S} = -\frac{1}{T_{1e}}(\mathbf{S} - \mathbf{S}_0) - \gamma_e (\mathbf{S} \times \mathbf{B}) . \quad (1)$$

Here, γ_e is the electron's gyromagnetic ratio, \mathbf{B} is magnetic field, and T_{1e} is a time constant governing relaxation of \mathbf{S} to an equilibrium spin polarization \mathbf{S}_0 . For optically-pumped electrons, angular momentum conservation requires that \mathbf{S}_0 be directed along the optical excitation axis with a magnitude determined by selection rules and by competition between recombination with holes (at rate $1/\tau$), assumed unpolarized [15, 16], and the usual magnetic-field dependent spin-dephasing processes (at rate $1/\tau_S(B)$).

$$\mathbf{S}_0 = \frac{1}{2} C \frac{\tau_S(B)}{\tau + \tau_S(B)} \mathbf{n}_E \quad (2)$$

where \mathbf{n}_E is a unit vector parallel to the optical excitation axis and C is a constant depending on the band structure of the semiconductor ($C = 1/2$ for bulk GaAs and the heterojunction studied here). Both recombination and spin dephasing rates contribute to T_{1e} :

$$1/T_{1e} = 1/\tau + 1/\tau_S(B) . \quad (3)$$

The total magnetic field \mathbf{B} experienced by the electron includes the usual static magnetic field \mathbf{B}_0 as well as nuclear hyperfine fields [8, 17] $\mathbf{B}_N^j(t)$ (from isotopes j) which can rival the static field in magnitude and which may be manipulated as in any NMR experiment with resonant rf pulses $\mathbf{B}_1(t)$.

$$\mathbf{B} = \mathbf{B}_0 + \mathbf{B}_1(t) + \sum_j \mathbf{B}_N^j(t) \quad (4)$$

In considering how S may be made to respond linearly to changes in a nuclear hyperfine field, it is enough to consider the steady-state solution to equation (1). This solution is valid under the condition that S follows B adiabatically:

$$\left| \frac{1}{B} \frac{\partial}{\partial t} B \right| \ll \frac{1}{T_{1e}}. \quad (5)$$

Since $T_{1e} \sim$ nanoseconds, a nuclear hyperfine-field magnetometer relying on the steady-state behavior of electron spin polarization can have an operating bandwidth of up to many hundreds of MHz.

The following solution for steady state electron spin polarization has been derived by Fleisher and Merkulov [18].

$$S = \frac{B_H^2 S_0 + (S_0 \cdot B)B + B_H (B \times S_0)}{B_H^2 + B^2} \quad (6)$$

The solution introduces as a parameter the Hanle width $B_H = 1/\gamma_e T_{1e}$ which represents a magnetic field scale for competition between precession and decay of electron spin polarization. The degree of circular polarization of luminescence, ρ , measures the component of S along a unit vector n_D describing the direction of observation:

$$\rho = -2C S \cdot n_D = \rho_0(B) \frac{B_H^2 (n_E \cdot n_D) + (B \cdot n_E)(B \cdot n_D) + B_H B \cdot (n_E \times n_D)}{B_H^2 + B^2} \quad (7)$$

where

$$\rho_0(B) \equiv -2CS_0(B) \quad (8)$$

represents the equilibrium polarization at a given magnetic field in an experiment where the magnetic field, optical excitation, and optical detection axes are all parallel. This equation is the starting point for understanding optical detection of NMR in semiconductors. Luminescence polarization is influenced by the magnitude and direction of at least three vectors: 1) S_0 , parallel to the exciting laser, 2) n_D , parallel to the optical detection axis and 3) B , the total magnetic field, including Zeeman- and hyperfine-field contributions.

Previous optical detection protocols applied to the study of a GaAs/AlGaAs heterojunction have been found to be inadequate. These experiments will be reviewed both as a basis for understanding the principles of optical detection of NMR in semiconductors and as motivation for the development of Larmor beat detection.

IV Conventional Optical Detection of NMR in GaAs Heterostructure

The sample studied was a single p-channel GaAs/AlGaAs heterojunction grown along the [001] axis by molecular beam epitaxy [7, 19, 20]. A substrate of semi-insulating GaAs supports a 2500 nm layer of undoped GaAs, followed by a 6.5 nm layer of undoped $\text{Al}_x\text{Ga}_{1-x}\text{As}$ ($x = 0.36$), a 30 nm layer of p-type $\text{Al}_x\text{Ga}_{1-x}\text{As}$ ($x = 0.36$) doped with $6 \times 10^{17}/\text{cm}^3$ of Be, and a 21 nm layer of undoped GaAs. The photoluminescence spectrum of the sample reveals the expected lines at 818 nm (bulk exciton luminescence) [7], and 825 nm and 830 nm (*e*-line and *d*-line respectively of *H*-band luminescence) [19, 20] which have been assigned to transitions involving the recombination with electrons of the 2D heavy holes localized near the interface between GaAs and undoped AlGaAs.

The sample was attached by high vacuum grease to a G-10 fiberglass probe immersed in 2 K superfluid ^4He . The 240 mT Zeeman field, optical detection axis, and sample growth axis were nominally parallel. A GaAs/AlGaAs laser diode delivered ~ 5 mW CW of circularly polarized 780 nm light over ~ 1 mm², incident 15° off axis. Sample luminescence passed through a 50 kHz photoelastic modulator, a linear polarizer, an 830 nm bandpass filter (FWHM 10 nm), and was detected with a silicon avalanche photodiode in linear mode. For steady-state experiments described in this section, the photocurrent was demodulated by 50 kHz. For Larmor beat experiments to be described subsequently, the photocurrent was demodulated by the relevant beat frequency plus and minus 50 kHz. The demodulated signal, proportional to the time-dependent difference in intensity between left and right circularly polarized luminescence, and hence, assuming constant total luminescence ρ , was digitized.

The highest sensitivity optical detection protocols have employed Hanle-effect depolarization of luminescence by transverse magnetic fields [2, 6, 13]. FIG. 1 illustrates the experiment, where we consider for generality that there are two transverse fields, a signal field $\mathbf{B}_N^{\text{sig}}$ and a reference field $\mathbf{B}_N^{\text{ref}}$, transverse to optical pumping \mathbf{n}_E , detection \mathbf{n}_D , and magnetic field \mathbf{B}_0 axes, all parallel to the *z* axis.

Neglecting any dependence of ρ_0 on total magnetic field, equation (7) predicts

$$\rho = \rho_0 \frac{B_H^2 + |\mathbf{B}_0 + \mathbf{B}_N^{\text{misc}}|^2}{B_H^2 + |\mathbf{B}_0 + \mathbf{B}_N^{\text{misc}}|^2 + |\mathbf{B}_N^{\text{ref}} + \mathbf{B}_N^{\text{sig}}|^2}, \quad (9)$$

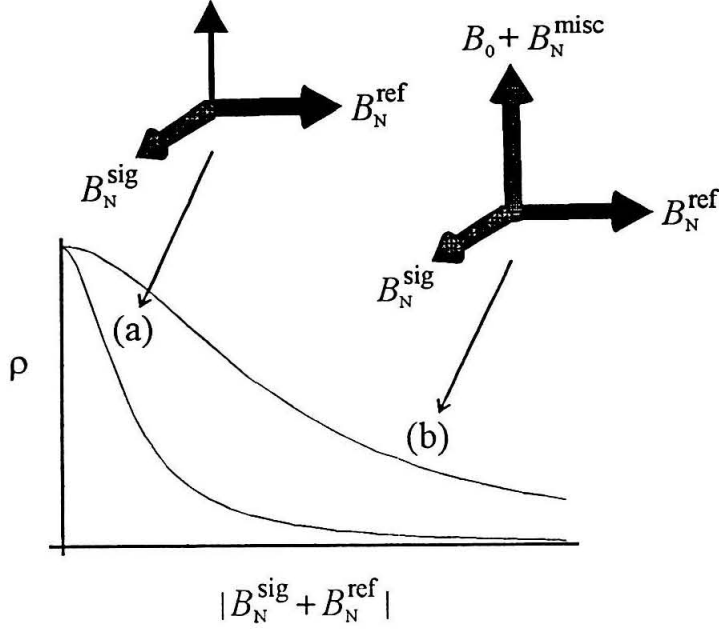


FIG. 1. Hanle-effect depolarization of luminescence by transverse magnetic fields.

(a) Depolarization in zero longitudinal field is described by a Lorentzian with $\text{FWHM} = B_H$. (b) The FWHM for depolarization in the presence of a z-axis static magnetic field B_0 and miscellaneous nuclear hyperfine fields B_N^{misc} increases to $\sqrt{B_H^2 + |B_0 + B_N^{\text{misc}}|^2}$.

where B_N^{ref} represents any remaining nuclear hyperfine or other fields along the z-axis.

This may be rewritten

$$\rho = \rho_0 \frac{1}{1 + |b_N^{\text{ref}} + b_N^{\text{sig}}|^2}, \quad (10)$$

where

$$b_N^{\text{ref, sig}} = \frac{B_N^{\text{ref, sig}}}{\sqrt{B_H^2 + |B_0 + B_N^{\text{misc}}|^2}}. \quad (11)$$

are the transverse reference and signal fields in reduced units.

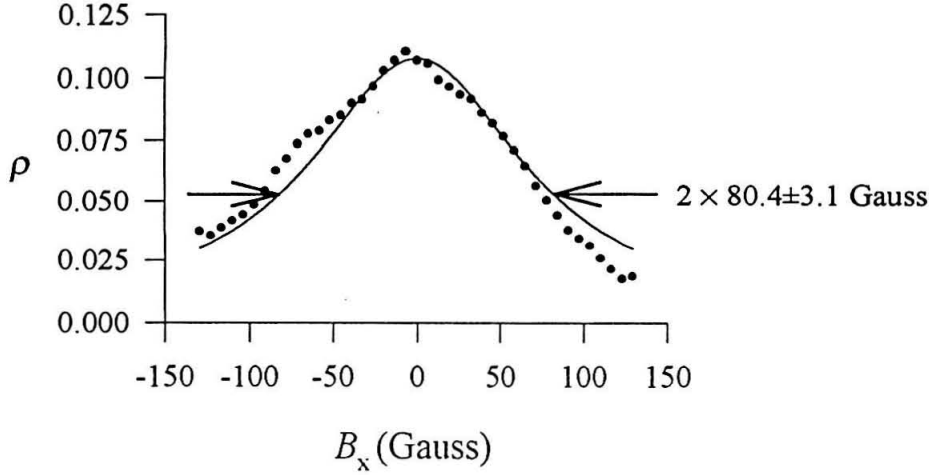


FIG. 2. Hanle-effect depolarization of luminescence in a GaAs heterojunction by a single transverse magnetic field.

With $B_0=0$, a transverse field B_x is swept as the circular polarization of luminescence ρ is monitored. Optical pumping along the z -axis can provide no enhancement in nuclear magnetization B_N quantized along a transverse field B_x larger than the electron hyperfine field (~ 1 -10 Gauss). Consequently, ρ is well-fit to equation (10) with $B_N = B_0 = 0$ and $B_H = 80.4 \pm 3.1$ Gauss .

FIG. 2 exhibits a determination of B_H for the heterostructure. In this experiment, a single external transverse field B_x is swept as ρ is monitored. The observed depolarization is well-described by the last two equations, with $B_0 = B_N^{\text{misc}} = B_N^{\text{sig}} = 0$ and $B_N^{\text{ref}} = B_x \hat{x}$:

$$\rho = \rho_0 \frac{B_H^2}{B_H^2 + B_x^2}. \quad (12)$$

The value $B_H = 80.4 \pm 3.1$ Gauss thus inferred is small compared to obtainable laboratory magnetic fields, indicating the feasibility of employing time-sequenced optical NMR [6, 10, 12] to record evolution of nuclear magnetization in the heterostructure.

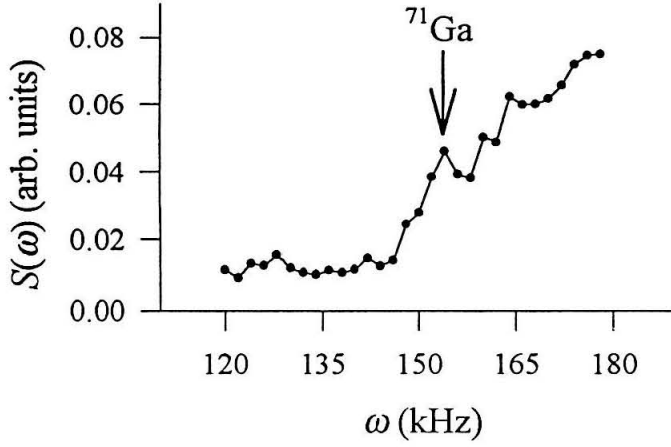


FIG. 3. Time-sequenced continuous-wave (CW) optical NMR spectrum of the heterostructure. Following $\tau_L = 120$ sec of optical nuclear polarization in a field $\mathbf{B}_0 = B_0 \hat{z}$ ($B_0 = 11.2$ mT), irradiation at frequency ω diminishes nuclear magnetization for isotopes at resonance as in any CW-NMR experiment. The static field is then cycled to a value $\mathbf{B}_N^{\text{ref}} = B_0^{\text{d}} \hat{x}$ ($B_0^{\text{d}} = 10.3$ mT), and ρ is recorded as remaining nuclear magnetization $\mathbf{B}_N^{\text{sig}}(\omega)$ decays. The integrated transient ρ , $S(\omega) \propto B_N^{\text{sig}}(\omega)$, is plotted versus ω in the figure. A peak in the thus recorded CW NMR spectrum appears for ^{71}Ga on top of an unexpected baseline.

A time-sequenced optical NMR (TSONMR) experiment employs a static laboratory reference field to turn the Hanle effect into a linear-response magnetometer as follows. After a period τ_L of optical nuclear polarization in a z -axis field \mathbf{B}_0 , irradiation at frequency ω diminishes longitudinal magnetization as in a conventional CW-NMR experiment. After allowing for any transverse nuclear field to dephase, the static field is rotated onto the x -axis such that the remaining nuclear field $\mathbf{B}_N^{\text{sig}}(\omega)$ follows adiabatically. The observed luminescence polarization is described by FIG. 1(a) and equation (10), with $\mathbf{B}_0 = \mathbf{B}_N^{\text{misc}} = 0$ and $\mathbf{B}_N^{\text{ref}} = B_0^{\text{d}} \hat{x}$ in equation (11) representing the externally applied transverse static

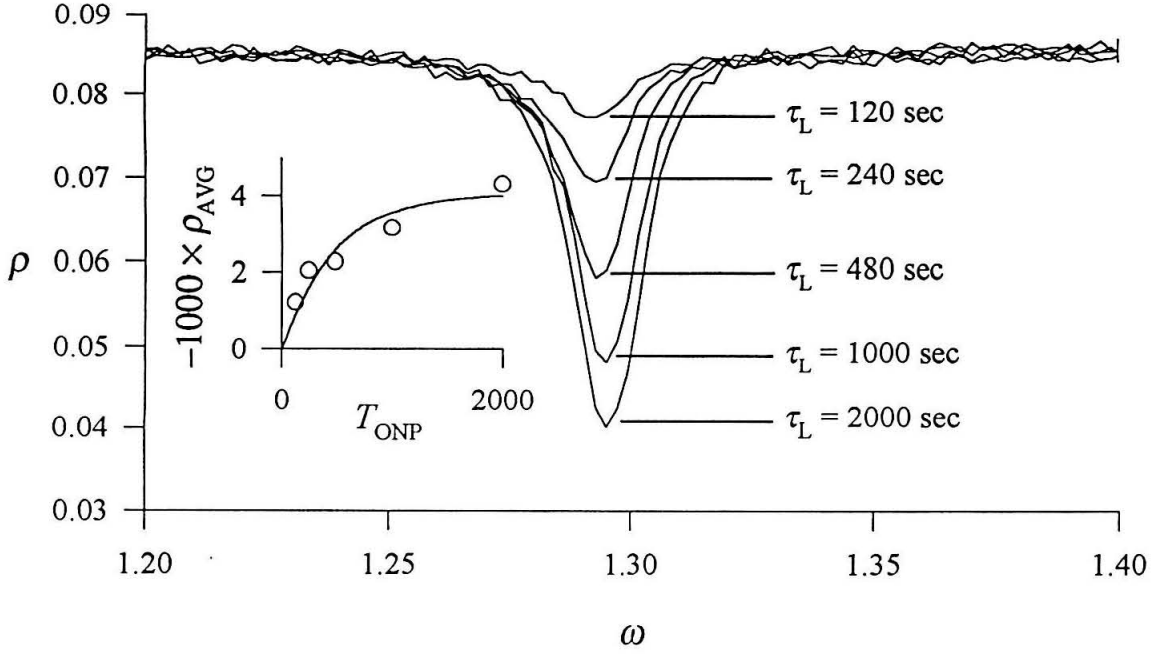


FIG. 4. Adiabatic rapid passage steady-state optical NMR of the heterostructure.

Following τ_L seconds of optical nuclear polarization at high field $\mathbf{B}_0 = B_0 \hat{z}$ ($B_0 = 98.3$ mT), a weak transverse rf magnetic field is swept in adiabatically through resonance for the ^{71}Ga isotope (0.2 MHz in 10 sec). ^{71}Ga magnetization $\mathbf{B}_N^{\text{sig}}$ follows the rf's effective field in the rotating frame, such that at half-passage it is transverse to the z -axis, leading to a Hanle-effect depolarization of luminescence. This figure exhibits ρ recorded during rapid passage for $\tau_L=120$ -2000 sec. The average amount of depolarization is plotted versus τ_L in the inset, indicating a time constant for light-on growth of nuclear magnetization $T_{\text{ion}} = 475 \pm 150$ sec .

magnetic field during detection. Expanding this special case of equation (10) in a Taylor series about

$B_N^{\text{sig}}(\omega) = 0$ gives

$$\rho = \rho_0 \left\{ \frac{1}{[b_N^{\text{ref}}]^2 + 1} - 2 \frac{b_N^{\text{ref}}}{\{[b_N^{\text{ref}}]^2 + 1\}^2} b_N^{\text{sig}}(\omega) + \frac{(3[b_N^{\text{ref}}]^2 - 1)}{\{[b_N^{\text{ref}}]^2 + 1\}^3} [b_N^{\text{sig}}(\omega)]^2 + O([b_N^{\text{sig}}]^3) \right\}. \quad (13)$$

This equation suggests that ρ will respond linearly (to third order) in changes of $b_N^{\text{sig}}(\omega) \ll 1$ about zero when $B_N^{\text{ref}} = B_H / \sqrt{3}$. Such behavior is not in fact observed in the CW TSONMR experiment on the heterojunction.

FIG. 3 exhibits a CW TSONMR spectrum for the heterojunction. While a resonance for ^{71}Ga appears at the expected frequency, it appears on top of an unexpectedly rising baseline. One hypothesis is that this baseline reflects the long-time growth (~ 30 minutes) of miscellaneous nuclear fields during optical pumping. These fields would add to B_N^{ref} after field rotation, and if they became larger than the Hanle width, would move detection off the sensitive point $B_N^{\text{ref}} = B_H / \sqrt{3}$.

That optical pumping leads to large nuclear fields on this timescale is confirmed by optically detecting NMR during adiabatic passage [21] through resonance at high field (~ 0.2 T). In this experiment, following a time τ_b of optical nuclear polarization, a transverse rf magnetic field is swept through resonance such that nuclear magnetization of the resonant isotope, B_N^{sig} , follows the applied field in the rotating frame (and is inverted by the rapid passage). At half passage, when the rf is at resonance, B_N^{sig} is transverse to the static plus off-resonance miscellaneous nuclear fields and leads to a Hanle-effect depolarization of luminescence as in FIG. 1(b). Equation (10) with $B_N^{\text{ref}} = 0$ describes ρ .

FIG. 4 illustrates the observed depolarization versus τ_L for different optical polarization times τ_L . The data imply a timescale for light-on buildup of optical nuclear polarization of $T_{1\text{on}} = 475 \pm 150$ sec (8 minutes). Not only is the depolarization at resonance for B_N^{sig} (^{71}Ga) dependent on τ_L , but it is also sensitive to prior rapid passage through resonance of other isotopes comprising B_N^{misc} (^{69}Ga and ^{71}As ; data not shown). This is explained by the fact that $B_N^{\text{misc}} \sim B_0$, from which it is concluded that nuclear fields $B_N^{\text{tot}} \sim 0.2$ T are obtained after ~ 120 sec of optical nuclear polarization.

Observed modulation of ρ by longitudinal magnetic fields, exhibited in FIG. 5, corroborates this hypothesis. Variation of ρ_0 with longitudinal field results from the dependence of electron spin relaxation on magnetic field. Equations (2) and (8) predict

$$\rho_0 = \frac{1}{4} \frac{\tau_S(B)}{\tau + \tau_S(B)} \quad (14)$$

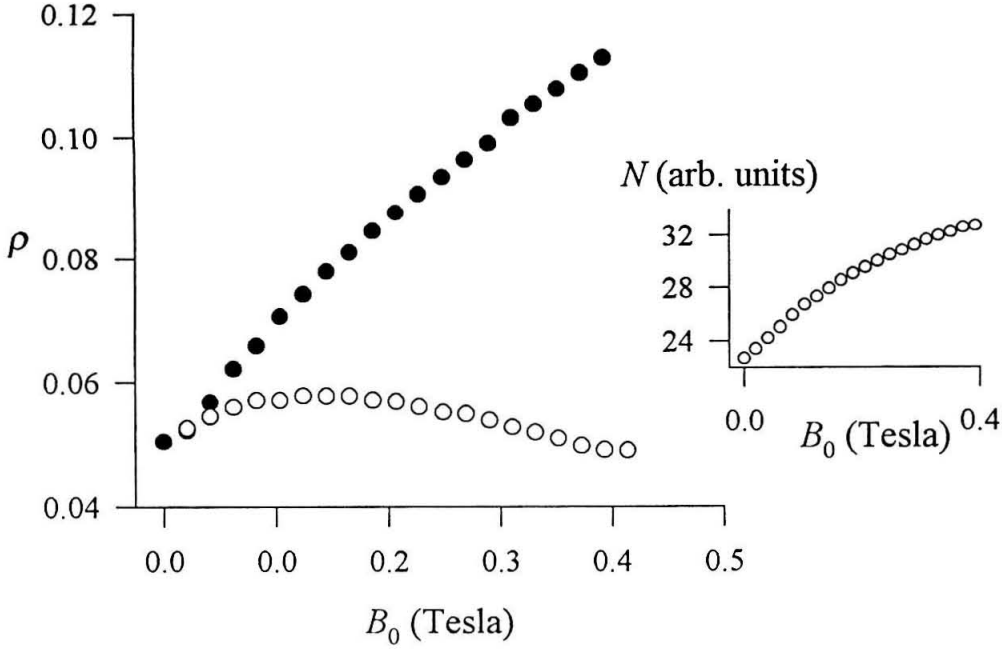


FIG. 5. Modulation of ρ in a GaAs heterojunction by longitudinal magnetic fields.

The figure illustrates luminescence polarization obtained after ~ 120 sec of optical pumping (per point) with the static field either parallel (closed circles) or antiparallel (open circles) to the axis of optically-oriented nuclear magnetization. The inset illustrates variation of total luminescence N versus static field.

with $B = B_0 + B_N^{tot}$ for the static field parallel to the axis of optical nuclear orientation, and $B = B_0 - B_N^{tot}$ for the antiparallel geometry. Berkovits [22] fits similar data using a model for $\tau_s(B)$ in which [21]

$$\tau_s(B) = \tau_s(0) \left(1 + \left[\frac{B}{B_\gamma} \right]^2 \right) \quad (15)$$

where $\tau_s(B)$ is a zero-field electron dephasing time and B_γ is correlation time for the fluctuating magnetic field responsible for electron spin relaxation converted to field units through the electron gyromagnetic ratio. Fitting FIG. 5's data using Berkovits procedure returns unreasonably large nuclear fields, perhaps due to the observed increase of total luminescence with magnetic field, unaccounted for in his model.

This increase has been observed before [19], and is hypothesized to be due to mixing of valence band light- and heavy-hole states by the magnetic field. Nevertheless, the behavior of a $B_N^{tot} = 0$ curve, gleaned by averaging the two observed curves, indicates qualitatively that $B_y \geq 0.1$ T. Assuming this, the difference in the two curves must be due to nuclear fields large compared to B_0 and B_y .

Such nuclear fields, large compared to B_H , are incompatible with linear-response TSONMR, which requires that $B_N^{sig} \leq B_H$. Linear response may be restored by providing a reference field controlled by time-dependent feedback to keep $|B_N^{ref} - B_N^{sig}| \leq B_H$ as the signal field decays. For the GaAs/AlGaAs heterojunction, this would require cycling a field $B_N^{ref} \sim 0.1$ T in a few seconds, which is challenging, but not impossible. Even with linear response restored, optical pumping to steady state to achieve a state of reproducible spin order for each data point would result in acquisition times in excess of 8 hours per 64-point spectrum. Optical pumping of nuclear magnetization could be arrested after a short time (once $B_N^{sig} \leq B_H$) prior to field cycling, but the resulting signal would be undesirably sensitive to residual magnetization.

We desire instead a nuclear field magnetometer with larger dynamic range, capable of responding linearly to large hyperfine fields in real time. Large dynamic range is already observed in optical detection of NMR during adiabatic rapid passage. Indeed, sensitivity to a signal field can even be adjusted by reorienting B_N^{misc} or changing B_0 , effecting the denominator in equation (11). While large depolarizations are observed for $B_N^{sig} \sim B_0 \gg B_H$ in this experiment, it is at the expense of linear response. Larmor beat detection recovers linear response with similarly adjustable dynamic range by introducing a reference field in the form of a second in-plane nuclear hyperfine field, with the consequence that an entire NMR interferogram can be acquired in real time.

V Larmor-Beat Optical Detection of NMR

Larmor beat detection relies on the depolarization of semiconductor luminescence by two precessing hyperfine nuclear fields: a reference field B_N^{ref} and a signal field B_N^{sig} corresponding to two

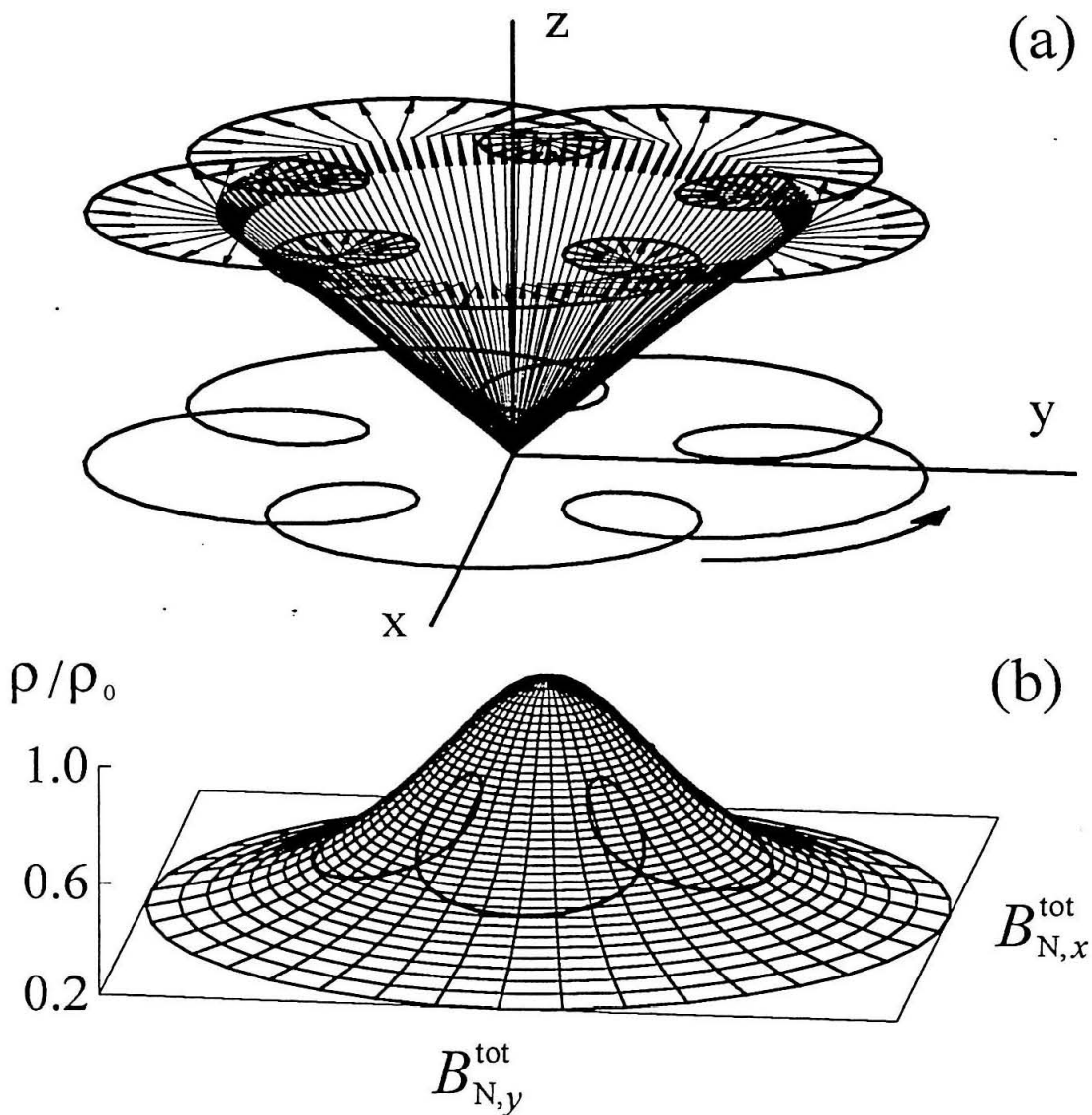


FIG. 6. Evolution of nuclear fields and luminescence polarization during Larmor beat detection. (a) Schematic depiction of the evolution of ^{71}Ga and ^{75}As nuclear hyperfine fields during Larmor beat detection. The "reference" field (^{75}As) is shown precessing in a cone about the z -axis defined by the static magnetic field (not shown), in steady state response to weak off-resonance irradiation. The "signal" field (^{71}Ga) is shown as a purely transverse field precessing about the static field. The vector sum of the two fields is shown as an elevated rosette, and its projection, of relevance to the Hanle effect, is shown in the xy -plane. (b) The transverse component of the vector sum trajectory is shown projected onto the 2D Hanle curve describing luminescence depolarization. The vertical component of the projected curve gives ρ which now oscillates, primarily at the Larmor beat frequency.

distinct nuclear species. FIG. 6 illustrates schematically the orientations for the signal and reference nuclear fields during Larmor beat detection.

The solution to equation (7), applicable to two single-frequency circularly polarized nuclear hyperfine fields, is

$$\rho = \rho_0 \frac{1}{1 + (b_N^{\text{ref}})^2 + (b_N^{\text{sig}})^2 + 2b_N^{\text{ref}}b_N^{\text{sig}} \cos \omega_{rs} t} \quad (16)$$

where equation (11) defines the nuclear fields in reduced units. Expanding this result in a Taylor series

about $b_N^{\text{sig}} = 0$ and generalizing the result to include an arbitrary set of signal fields $b_N^{\text{sig},j}$ gives

$$\rho(t) = \rho_0 \left\{ \frac{1}{1 + [b_N^{\text{ref}}(t)]^2} - 2 \sum_j \left(\frac{b_N^{\text{ref}}(t)}{\{1 + [b_N^{\text{ref}}(t)]^2\}^2} b_N^{\text{sig},j}(t) + O((b_N^{\text{sig},j})^3) \right) \cos \omega_{rs,j} t \right\} \quad (17)$$

where $\omega_{rs,j} = \omega_{s,j} - \omega_r$ is the difference in Larmor frequencies between the reference and signal fields,

and the index j indexes lines in the spectrum, including lines from more than one isotope if applicable.

As written, the time dependence of the magnitudes of b_N^{ref} and $b_N^{\text{sig},j}$ is due to transverse relaxation of

each separate nuclear hyperfine field. With weak irradiation or spin locking, b_N^{ref} changes slowly

($T_{1\rho} \sim 1$ sec) compared to the decay of $b_N^{\text{sig},j} < 1$ ms. Under these conditions, the Fourier components are essentially those present in the transients of the *signal* nuclei alone.

Linear response to $b_N^{\text{sig}} \ll b_N^{\text{ref}}$ is optimized for $b_N^{\text{ref}} = 1/\sqrt{3}$, as in TSONMR. For $B_N^{\text{misc}} = -B_0$, the small-signal response is identical to that of TSONMR. For other situations, LBD achieves worse response than TSONMR, but has larger dynamic range, requiring only $B_N^{\text{sig}} \ll \sqrt{B_H^2 + |\mathbf{B}_0 + \mathbf{B}_N^{\text{misc}}|^2}$.

FIG. 7 shows a real-time ^{71}Ga free induction decay (FID) recorded using optical Larmor beat detection and the timing sequence SAT– τ_L – $\pi/2$ –DET. Here SAT represents a train of ten $\pi/2$ pulses (10 ms apart) applied to each of the principle isotopes (^{69}Ga , ^{71}Ga , and ^{75}As) to provide a reproducible condition of saturation or null spin order before each shot. A period τ_L of optical nuclear polarization is followed by a $\pi/2$ pulse delivered to ^{71}Ga , and DET represents Larmor-beat detection of the ^{71}Ga NMR free induction decay during weak ^{75}As irradiation off resonance.

VI Larmor-Beat Optical Detection: Beyond Small-Signal Response

In order to make quantitative a dynamic range estimate for LBD and in order to assess the validity of the small-signal response derived above, Fourier components of ρ must be calculated, valid for

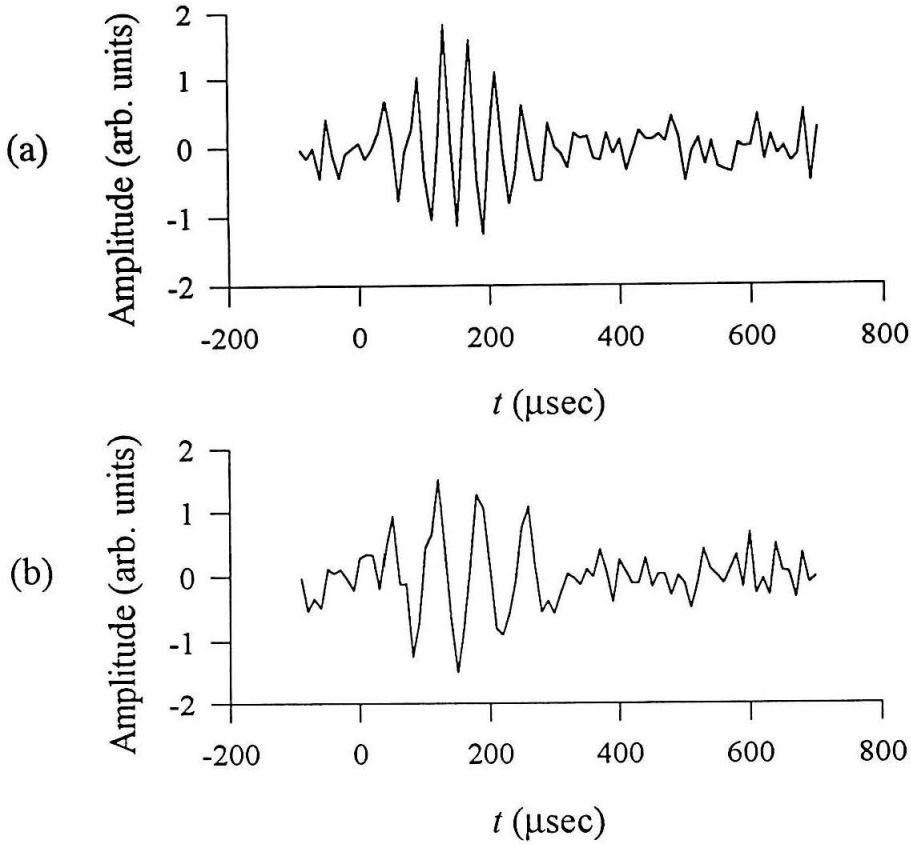


FIG. 7. Real-time optical detection of the ^{71}Ga free induction decay in a GaAs heterojunction. Following $\tau_L = 5$ seconds of optical nuclear polarization, a $3.6 \mu\text{s}$, 3.152 MHz $\pi/2$ pulse to ^{71}Ga at time zero creates the transverse nuclear "signal" field. A 0.6 mT , 1.824 MHz ^{75}As spin lock 56 kHz off resonance provides the transverse "reference" field. Luminescence polarization, sampled during free evolution and demodulated by a frequency 24 kHz below the Larmor beat frequency, is digitized to give the observed transient. The transient shown represents 100 averages taken in 10 minutes total time. The transients' risetime is due to filter response. Evolution frequency varies proportionally to gyromagnetic ratio $\gamma(^{71}\text{Ga})$ for a change ΔB in static field, as expected. (a) $\Delta B\gamma(^{71}\text{Ga}) = 0 \text{ kHz}$ and (b) $\Delta B\gamma(^{71}\text{Ga}) = 10 \text{ kHz}$.

any value of the two nuclear fields. For simplicity, consider LBD with just two nuclear fields b_N^{ref} and b_N^{sig} . Begin by rewriting equation (16) as

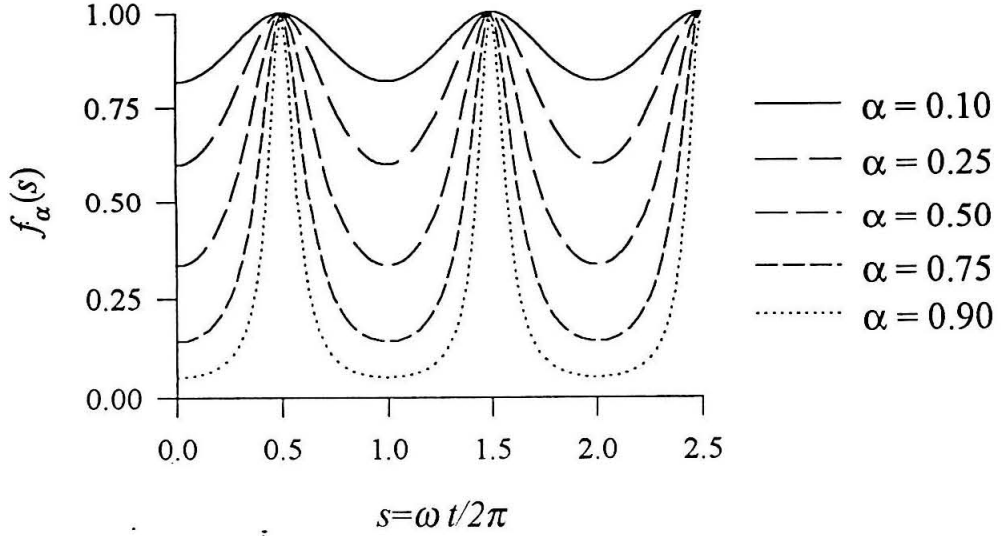


FIG. 8. Short-time evolution of luminescence polarization.

The function $f_\alpha(t) = (1-\alpha)/(1+\alpha \cos(\omega_{rs}t))$ describing rapid oscillations of luminescence polarization during the Larmor beat experiment is plotted over two and a half Larmor beat periods for different values of the parameter α . For larger values of α the oscillations begin to resemble trains of equally-spaced delta functions, which must contain Fourier components at many harmonics of the Larmor beat frequency.

$$\rho = \rho_0 \left\{ \frac{1}{1+\beta(t)^2} \right\} \left\{ \frac{1 \mp \alpha(t)}{1+\alpha(t) \cos \omega_{rs} t} \right\} \equiv \rho_0 \left\{ \frac{1}{1+\beta(t)^2} \right\} f_\alpha(t) \quad (18)$$

where

$$\alpha(t) \equiv \frac{2 b_N^{\text{sig}}(t) b_N^{\text{ref}}(t)}{1 + [b_N^{\text{sig}}(t)]^2 + [b_N^{\text{ref}}(t)]^2} \quad (19)$$

and

$$\beta(t) \equiv b_N^{\text{sig}}(t) \mp b_N^{\text{ref}}(t) \quad (20)$$

where the equation with the minus sign holds for positive α , and the plus sign for negative α . By reorganizing terms in this way, the rapid time dependence during LBD depends on a single parameter $-1 \leq \alpha(t) \leq +1$ through a bounded function $0 \leq f_\alpha(t) \leq 1$. The Fourier expansion for $\rho(t)$ is defined as

$$\hat{\rho}(\omega) = \int_0^\infty dt \exp(i \omega t) \rho(t). \quad (21)$$

Considering now positive α , substituting (18) into (21) gives

$$\hat{\rho}(\omega) = \rho_0 \int_0^\infty dt \exp(i \omega t) \left\{ \frac{1}{1 + \beta(t)^2} \right\} \left\{ \frac{1 - \alpha(t)}{1 + \alpha(t) \cos \omega_{rs} t} \right\}. \quad (22)$$

That the integrand has Fourier components at many harmonics of the Larmor beat frequency, ω_{rs} , is made evident by expanding the denominator of $f_\alpha(t)$ in a Taylor series in $\alpha(t)$ about $\alpha(t) = 0$:

$$f_\alpha(t) = \frac{1 - \alpha(t)}{1 + \alpha(t) \cos \omega_{rs} t} = (1 - \alpha(t)) \sum_{n=0}^{\infty} (-\alpha(t))^n \cos^n \omega_{rs} t. \quad (23)$$

By applying double angle formulas, each term $\cos^n \omega_{rs} t$ could be reduced to a sum of cosines of up to order $\cos(n \omega_{rs} t)$. The larger $\alpha(t)$, the more harmonics of ω_{rs} contribute to the sum. This observation corroborates the sketch of $f_\alpha(t)$ appearing in FIG. 8. Such an expansion of the integrand's last term would be an approximate route to evaluating this Fourier integral.

An approach to deriving a *closed-form* expression for this Fourier integral is detailed in Appendix A. This approach makes use of the fact that $\alpha(t)$ and $\beta(t)$ evolve experimentally on a timescale long compared to the Larmor beat period $1 / \omega_{rs}$. This is equivalent to asking only for Fourier components of ρ in narrow frequency range centered about one of the Larmor beat harmonics. The result of Appendix A is that such Fourier components may be written as

$$\hat{\rho}(\omega + m \omega_{rs}) = \int_0^\infty dt \exp(i \omega t) \rho^{(m)}(t), \quad (24)$$

valid for $\omega \ll \omega_{rs}$, where

$$\rho^{(m)}(t) = \rho_0 \frac{1}{1 + \beta(t)^2} \sqrt{\frac{1 - \alpha(t)}{1 + \alpha(t)}} \left(\frac{1 - \sqrt{1 - \alpha(t)^2}}{\alpha(t)} \right)^m. \quad (25)$$

The Fourier spectrum about each Larmor beat harmonic is now computable in terms of the long-time behavior of $\alpha(t)$ and $\beta(t)$. The functions $\rho^{(m)}(t)$ may be rewritten in terms of b_N^{ref} and b_N^{sig} using equations (19) and (20). The result for $m=0$ and $m=1$ appear below:

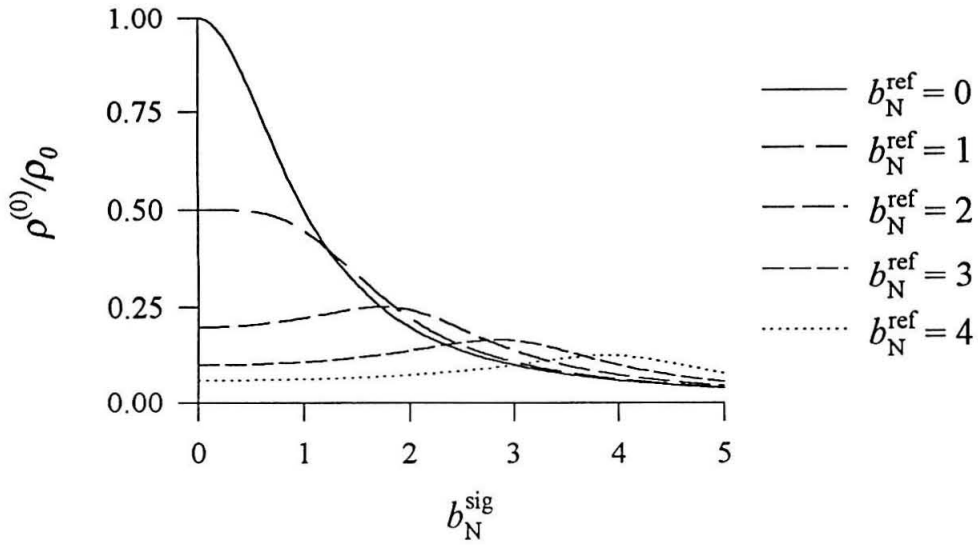


FIG. 9. Function determining the DC component of luminescence polarization during LBD experiment.

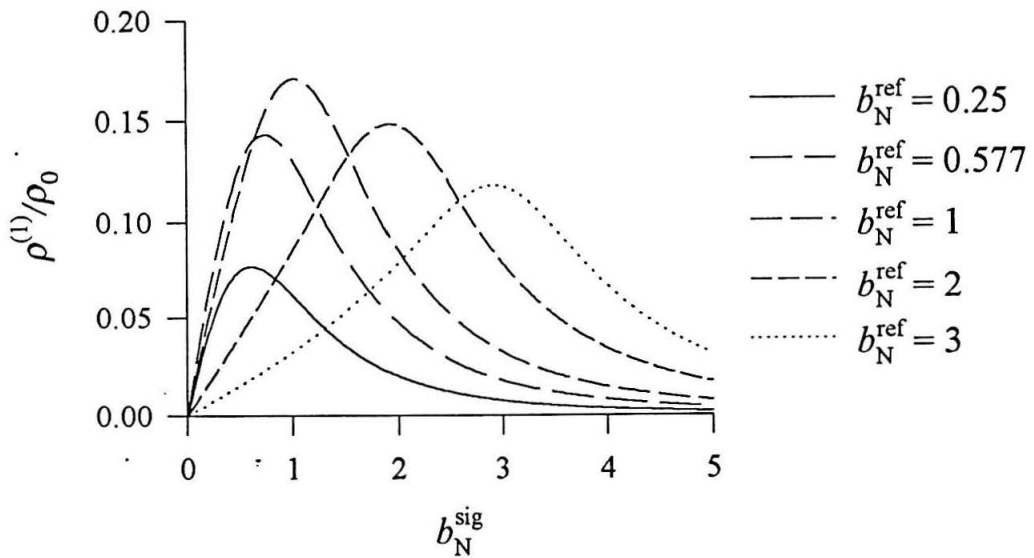


FIG. 10. Function determining the Fourier component of luminescence polarization at the Larmor-beat frequency.

technique	b_r	signal	largest b_s 1% dev.	largest b_s 10% dev.
LBD	$1/\sqrt{3}$	$0.65b_s - 0.609b_s^3 + 0.228b_s^5 + O(b_s^7)$	0.103	0.318
	$\sqrt{2}$	$0.314b_s - 0.0194b_s^5 + 0.00345b_s^7 + O(b_s^9)$	0.624	1.07
TSONMR	$1/\sqrt{3}$	$0.75 - 0.65b_s + 0.487b_s^3 - 0.422b_s^4 + O(b_s^5)$	0.249	0.536
	$\sqrt{2}$	$0.333 - 0.314b_s + 0.185b_s^2 - 0.0698b_s^3 + O(b_s^4)$	0.129	0.369

TABLE I. Small-signal expansions for LBD and TSONMR.

The LBD signal is the Fourier component of the luminescence polarization at the Larmor beat frequency, while the TSONMR signal is DC luminescence polarization. The last two columns indicate the largest signal fields for which the exact solution differs from linear response by 1% and 10%.

$$\rho^{(0)}(t) = \rho_0 \frac{1}{\sqrt{\{1 + [b_N^{\text{ref}}(t)]^2 + [b_N^{\text{sig}}(t)]^2\}^2 - \{2b_N^{\text{ref}}(t)b_N^{\text{sig}}(t)\}^2}} \quad (26)$$

$$\rho^{(1)}(t) = \rho_0 \frac{1 + [b_N^{\text{ref}}(t)]^2 + [b_N^{\text{sig}}(t)]^2 - \sqrt{\{1 + [b_N^{\text{ref}}(t)]^2 + [b_N^{\text{sig}}(t)]^2\}^2 - \{2b_N^{\text{ref}}(t)b_N^{\text{sig}}(t)\}^2}}{2b_N^{\text{ref}}(t)b_N^{\text{sig}}(t)\sqrt{\{1 + [b_N^{\text{ref}}(t)]^2 + [b_N^{\text{sig}}(t)]^2\}^2 - \{2b_N^{\text{ref}}(t)b_N^{\text{sig}}(t)\}^2}} \quad (27)$$

The function $\rho^{(0)}$, relevant to detection of luminescence polarization near zero frequency, is plotted in FIG. 9 for various fixed values of b_N^{ref} and b_N^{sig} . With either the reference or signal field zero, $\rho^{(0)}$ recovers the well-known Lorentzian describing depolarization of luminescence by a single transverse nuclear field. Likewise, the function $\rho^{(1)}$, relevant to signal at the Larmor beat frequency, is plotted in FIG. 10. Note that inserting equations (26) and (27) into equation (24) and expanding the result in a Taylor about $b_N^{\text{sig}} = 0$ recovers as leading terms the small-signal response of equation (17).

$$\hat{\rho}(\omega) = \int_0^\infty dt \exp(i\omega t) \left\{ \frac{1}{[b_N^{\text{ref}}(t)]^2 + 1} + \frac{[b_N^{\text{ref}}(t)]^2 - 1}{\{[b_N^{\text{ref}}(t)]^2 + 1\}^3} [b_N^{\text{sig}}(t)]^2 + O([b_N^{\text{sig}}(t)]^4) \right\} \quad (28)$$

$$\hat{\rho}(\omega + \omega_{rs}) = \rho_0 \int_0^\infty dt \exp(i\omega t) \left\{ \frac{b_N^{\text{ref}}(t)}{\{[b_N^{\text{ref}}(t)]^2 + 1\}^2} b_N^{\text{sig}}(t) + \frac{b_N^{\text{ref}}(t)\{[b_N^{\text{ref}}(t)]^2 - 2\}}{\{[b_N^{\text{ref}}(t)]^2 + 1\}^4} [b_N^{\text{sig}}(t)]^3 + O([b_N^{\text{sig}}(t)]^5) \right\} \quad (29)$$

TABLE 1 lists the first few terms in the small-signal expansion relevant to TSONMR and LBD, for two values of the reference field. One value, $b_r = 1/\sqrt{3}$, maximizes the linear-response coefficient for both LBD and TSONMR while the other value, $b_r = \sqrt{2}$, guarantees LBD linear response to fifth order in the signal field. Also indicated is the largest signal field for which the exact solution differs from linear response by 1% and 10%. This value is a measure of dynamic range, in that it indicates what the values of the signal field begin to introduce modulation-frequency harmonics into the spectrum. While dynamic range is larger, in reduced field units, for TSONMR at $b_r = 1/\sqrt{3}$, the table indicates that LBD's dynamic range is large for a much broader range of reference fields.

VII Other Sources of Larmor Beats

So far, the dependence of the equilibrium polarization ρ_0 on total field has been neglected. Actually, since it depends on field quadratically through $\tau_s(B)$, it is a potential source of Larmor beats. The total field during Larmor beat detection may be inserted into equations (14) and (15) describing ρ_0 and $\tau_s(B)$ respectively, and series-expanded in signal fields. The result may be written

$$\rho_0 = \frac{1}{4} \left\{ \frac{1}{1 + \theta / \{1 + [b_0 + b_N^{\text{misc}}]^2 + [b_N^{\text{ref}}]^2\}} + 2 \sum_j \theta \frac{b_N^{\text{ref}}}{\{1 + [b_0 + b_N^{\text{misc}}]^2 + [b_N^{\text{ref}}]^2 + \theta\}^2} b_N^{\text{sig},j} \cos \omega_j t \right\} \quad (30)$$

where $\theta = \tau/\tau_s(0)$. Here $b_N^j = B_N^j / B_\gamma$, and $b_0 = B_0 / B_\gamma$ are the fields in reduced units, where now B_γ sets the field scale. For this Larmor-beat modulation of ρ to be small compared to Hanle-effect modulation, B_γ should be large compared to $\sqrt{B_H^2 + |B_0 + B_N^{\text{misc}}|^2}$. Working near $B_N^{\text{misc}} = -B_0$ with $B_H \ll B_\gamma$ would guarantee this.

Consider finally what signal artifacts could arise from optically pumping at an angle $\theta_E \neq 0$ to the detection axis. With optical pumping, detection, and magnetic fields oriented as in FIG. 11, the relevant solution for ρ becomes

$$\rho = \rho_0 \frac{1}{1 + (b_N^{\text{sig}})^2 + (b_N^{\text{ref}})^2 + 2b_N^{\text{sig}} b_N^{\text{ref}} \cos \omega_r t} \left\{ \cos(\theta_E) + \sin(\theta_E) b_N^{\text{sig}} [(b_0 + b_N^{\text{misc}}) \cos \omega_s t + b_H \sin \omega_s t] \right. \\ \left. + \sin(\theta_E) b_N^{\text{ref}} [(b_0 + b_N^{\text{misc}}) \cos \omega_r t + b_H \sin \omega_r t] \right\} \quad (31)$$

where all fields appear in reduced units, as in (16). Off-axis pumping introduces terms oscillating at frequencies ω_r and ω_s which multiply the leading term oscillating primarily at the Larmor beat frequency.

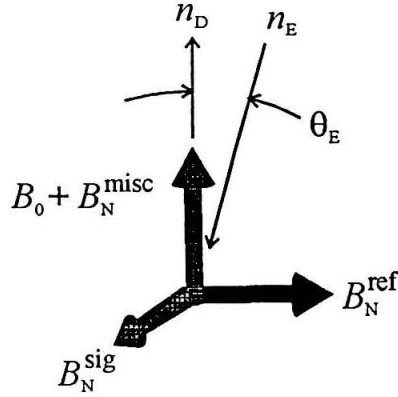


FIG. 11. Vectors relevant to calculation of Larmor beat signal.

Nuclear hyperfine fields B_N^{sig} and B_N^{ref} evolve in a plane perpendicular to the axis along which lie miscellaneous nuclear fields B_N^{misc} , the static Zeeman field B_0 , and the optical detection axis along n_D . The optical excitation axis along n_E is inclined at an angle θ_E from the z-axis.

The net result is to mix energy from the Larmor beat harmonics into sidebands $n\omega_{rs} \pm \omega_r$ and $n\omega_{rs} \pm \omega_s$, which are different enough from the ω_s that they are filtered out by the spectrometer during detection.

VIII Zeeman Frequency Detection of NMR in Semiconductors

Consider a single nuclear field B_N precessing at frequency ω_N in a plane inclined at an angle θ with respect to Hanle plane. Equation (7) predicts

$$\rho = \rho_0 \left\{ \frac{\sin^2 \theta + [b_N(t)]^2 \cos^2 \theta / 2}{1 + [b_N(t)]^2} + \frac{b_N(t)}{1 + [b_N(t)]^2} \sin 2\theta \cos \omega_N t + \frac{[b_N(t)]^2 / 2}{1 + [b_N(t)]^2} \cos^2 \theta \cos 2\omega_N t \right\} \quad (32)$$

where the nuclear field is expressed in reduced units, as in equation (16). This expression is exact. The Fourier component of ρ at the Zeeman frequency is maximized by setting $\theta = 45^\circ$. In analogy with equation (24), the Zeeman-frequency Fourier component is governed by time evolution of the function

$$\rho^{(1)} = \rho_0 \frac{b_N(t)}{1 + [b_N(t)]^2} \cong \rho_0 b_N(t) \quad (33)$$

The second expression is obtained by expanding the first in b_N , and predicts that this Zeeman frequency oscillation exhibits linear response to a single nuclear field $b_N \ll 1$.

A possible complication to implementing Zeeman frequency detection is that large nuclear fields are not built up along B_0 if it is much inclined to the optical pumping axis n_E . Large nuclear fields could be easily achieved by first optically pumping with B_0 parallel to n_E , and then adiabatically cycling B_0 to $\theta = 45^\circ$ before inducing precession of B_N . Alternatively, two lasers could be used: one to optically pump parallel to B_0 and a second to induce luminescence along an axis $\theta = 45^\circ$.

IX Conclusions

In conclusion, optical Larmor beat detection makes use of two precessing nuclear hyperfine fields to convert the excited-state Hanle effect into a high-sensitivity linear optical NMR method capable of real-time detection. The method applies to all samples where optical NMR by the Hanle effect is observable for two nuclear hyperfine fields, each comparable to the larger of the static field or Hanle width, a prerequisite satisfied by many known samples up to static fields of greater than 1 T [2]. LBD in such samples may be made to have small-signal response comparable to that of time-sequenced optical NMR. A theoretical treatment analyzes the LBD signal for all relevant Fourier components, and indicates that LBD achieves linear response over a surprisingly large range of nuclear fields. Analysis indicates that another source of Larmor beats in luminescence arises from variation of luminescence polarization with total magnetic field. Further experiments are necessary to estimate this contribution to the observed LBD transients. Finally, an optical detection geometry is introduced which encodes precession of a single nuclear field as a Zeeman frequency oscillation of luminescence polarization.

X Acknowledgments

This work was funded by the NSF program in Materials Synthesis and Processing and by NASA through the Caltech President's Fund. We thank A. Ksendzov, J. Liu, and F. Grunthner of the NASA Jet Propulsion Laboratory's Center for Space Microelectronics Technology for sample preparation and

luminescence characterization, L. Burnett and A. Perry for cryogenics advice, and S. Pedersen for proofreading.

XI Appendix A

We wish to compute the following integral:

$$\hat{\rho}(\omega) = \rho_0 \int_0^{\infty} dt \exp(i\omega t) \left\{ \frac{1}{1 + \beta(t)^2} \right\} \left\{ \frac{1 - \alpha(t)}{1 - \alpha(t) \cos \omega_{rs} t} \right\}. \quad (\text{A1})$$

Write the integral as an infinite series of integrals over time periods $\Delta \equiv 2\pi / \omega_{rs}$:

$$\int_0^{\infty} dt () = \sum_{n=0}^{\infty} \int_{n\Delta}^{(n+1)\Delta} dt (). \quad (\text{A2})$$

Let α_n be the average value of $\alpha(t)$ in the interval where $t \in (n\Delta, (n+1)\Delta)$, and similarly for β_n . As long as $\alpha(t)$ and $\beta(t)$ do not change much over the time intervals of integration in (A2), we can write the following. This approximation is equivalent to demanding that α and β have Fourier components at no frequencies near or above ω_{rs} .

$$\hat{\rho}(\omega) = \rho_0 \sum_{n=0}^{\infty} \int_{n\Delta}^{(n+1)\Delta} dt \exp(i\omega t) \left\{ \frac{1}{1 + \beta_n^2} \right\} \left\{ \frac{1 - \alpha_n}{1 - \alpha_n \cos \omega_{rs} t} \right\} \quad (\text{A3})$$

Now make a change of variables, $t = t' + n\Delta$, so that all the integrals in (A3) are over the same time interval. Notice that α_n , β_n , and $\cos(\omega_{rs} t)$ are unaffected by this change of variables. We now have (dropping the prime on the variable t):

$$\hat{\rho}(\omega) = \rho_0 \sum_{n=0}^{\infty} \exp(i\omega n \Delta) \frac{1 - \alpha_n}{1 + \beta_n^2} \int_0^{\Delta} dt \exp(i\omega t) \frac{1}{1 - \alpha_n \cos \omega_{rs} t}. \quad (\text{A4})$$

We are primarily interested in the Fourier components near harmonics of the Zeeman beat frequency, i.e., near $\omega \approx m \omega_{rs}$. We are therefore interested in computing, for $\omega \ll \omega_{rs}$, the quantity $\hat{\rho}(\omega + m \omega_{rs})$, where $m=0,1,2,\dots$. For example, $m=0$ corresponds to detecting the DC component of the luminescence, while $m=1$ corresponds to detecting the component near the Zeeman beat frequency, and so on. We write:

$$\hat{\rho}(\omega + m \omega_{rs}) = \rho_0 \sum_{n=0}^{\infty} \exp(i\omega n \Delta) \frac{1 - \alpha_n}{1 + \beta_n^2} \int_0^{\Delta} dt \exp(im\omega_{rs} t) \exp(i\omega t) \frac{1}{1 - \alpha_n \cos \omega_{rs} t}. \quad (\text{A5})$$

In the approximation $\omega \ll \omega_{rs}$,

$$\exp(i\omega t) \approx 1 \text{ for } t \in (n\Delta, (n+1)\Delta), \quad (\text{A6})$$

which lets us drop the first term in the integrand. The result is rewritten, after a change of variables

$\theta = 2\pi / \Delta$, as

$$\hat{\rho}(\omega + m \omega_{rs}) = \rho_0 \sum_{n=0}^{\infty} \exp(i\omega n \Delta) \frac{1 - \alpha_n}{1 + \beta_n^2} \frac{\Delta}{2\pi} \int_0^{2\pi} d\theta \exp(im\theta) \frac{1}{1 - \alpha_n \cos \theta}. \quad (\text{A7})$$

The remaining integral is computed in Appendix B. The result inserted into (A7) gives:

$$\hat{\rho}(\omega + m \omega_{rs}) = \rho_0 \sum_{n=0}^{\infty} \Delta \exp(i \omega n \Delta) \frac{1}{1 + \beta_n^2} \sqrt{\frac{1 - \alpha_n}{1 + \alpha_n}} \left(\frac{1 - \sqrt{1 - \alpha_n^2}}{\alpha_n} \right)^m, \quad (\text{A8})$$

which is written as

$$\hat{\rho}(\omega + m \omega_{rs}) = \sum_{n=0}^{\infty} \rho_n^{(m)} \Delta \exp(i \omega n \Delta), \quad (\text{A9})$$

$$\rho_n^{(m)} = \rho_0 \frac{1}{1 + \beta_n^2} \sqrt{\frac{1 - \alpha_n}{1 + \alpha_n}} \left(\frac{1 - \sqrt{1 - \alpha_n^2}}{\alpha_n} \right)^m. \quad (\text{A10})$$

We recognize the sum in (A9) as a Riemann sum, which approaches an integral as Δ goes to zero. We take this limit loosely, i.e., only on the RHS of (A8) because we do not want the limit to affect ω_{rs} on the LHS. We must be very careful of what we mean by this limit because, strictly speaking, it destroys the periodicity of ω with respect to ω_{rs} inherent in Fourier series (A9) *as written*. This limit is therefore only valid for $\omega \ll \omega_{rs}$. But we were only considering solutions to (A9) such that $\omega \ll \omega_{rs}$ to start with, so this represents no additional restriction. Replacing the sum in (A9) with the appropriate integral gives

$$\hat{\rho}(\omega + m \omega_{rs}) = \int_0^{\infty} dt \exp(i \omega t) \rho^{(m)}(t), \quad (\text{A11})$$

$$\rho^{(m)}(t) = \rho_0 \frac{1}{1 + \beta(t)^2} \sqrt{\frac{1 - \alpha(t)}{1 + \alpha(t)}} \left(\frac{1 - \sqrt{1 - \alpha(t)^2}}{\alpha(t)} \right)^m. \quad (\text{A12})$$

Note that the restriction that $\omega \ll \omega_{rs}$ can be lifted if the integral in (A5) can be calculated.

XII Appendix B

We wish to compute the following integral. The integrals I_0 and I_1 appear in standard tables [23, 24], but the general form does not.

$$I_n = \int_0^{2\pi} d\theta \frac{\exp in\theta}{1 - \alpha \cos(\theta)} \quad (\text{B1})$$

It is well known that any integral of trigonometric functions over $(0, 2\pi)$ can be computed as a contour integral over $|z|=1$ in the complex plane [25]. To this end, make the substitution

$$z = \exp i\theta. \quad (\text{B2})$$

As θ goes from 0 to 2π , the variable z traces the contour defined by $|z|=1$. Compute

$$d\theta = -i \frac{dz}{z}, \quad (\text{B3})$$

$$\cos \theta = \frac{1}{2} (\exp i\theta + \exp^{-i\theta}) = \frac{1}{2} \left(z + \frac{1}{z} \right). \quad (\text{B4})$$

Substitutions (B2) through (B4) into (B1) gives

$$I_n = 2i \oint_{|z|=1} dz \left(\frac{z^n}{\alpha \left(z^2 - \frac{2}{\alpha} z + 1 \right)} \right). \quad (\text{B5})$$

This integral may be evaluated using the Residue theorem. The denominator of the integrand has two simple poles at:

$$z_1 = \frac{1}{\alpha} (1 - \sqrt{1 - \alpha^2}), \quad (\text{B6})$$

$$z_2 = \frac{1}{\alpha} (1 + \sqrt{1 - \alpha^2}). \quad (\text{B7})$$

The integral may be rewritten as:

$$I_n = 2i \oint_{|z|=1} dz \left(\frac{z^n}{\alpha (z - z_1)(z - z_2)} \right). \quad (\text{B8})$$

For $-1 \leq \alpha \leq 1$ only the pole at $z=z_1$ satisfies $|z|<1$ and is inside the contour $|z|=1$. The Residue theorem states

$$\oint_{\Gamma} dz f(z) = 2\pi i \sum_{j=1}^n \text{Res}(f; z_j), \quad (\text{B9})$$

where z_j are the n non-analytic points of $f(z)$ inside the contour Γ , and $\text{Res}(f; z_j)$ represents the coefficient of the $1/(z-z_j)$ term in the Laurent expansion of $f(z)$ about z_j . In computing I_n , only the residue at $z=z_1$ need be considered. This residue is

$$\text{Res}\left(\frac{z^n}{\alpha(z-z_1)(z-z_2)}; z_1\right) = \frac{z_1^n}{\alpha(z_1-z_2)}. \quad (\text{B10})$$

Using (B10) and applying the Residue theorem (B9) to compute the integral (B5) gives the following result after substituting (B6) for z_1 and z_2 :

$$I_n = \frac{-4\pi z_1^2}{\alpha(z_1-z_2)} = \frac{2\pi}{\sqrt{1-\alpha^2}} \left(\frac{1-\sqrt{1-\alpha^2}}{\alpha}\right)^n. \quad (\text{B11})$$

XIII References

- [1] *Nuclear Dynamic Polarization by Optical Electronic Saturation and Optical Pumping in Semiconductors*
G. Lampel, Physical Review Letters **20** 491 (1968).
- [2] Optical Orientation,
F. Meier and B. P. Zakharchenya, Eds., Elsevier, Amsterdam (1984).
- [3] *Directly Detected Nuclear-Magnetic-Resonance of Optically Pumped GaAs Quantum-Wells*
S. E. Barrett, R. Tycko, L. N. Pfeiffer, and K. W. West, Physical Review Letters **72** 1368-71 (1994).
- [4] *Electronic States in Gallium-Arsenide Quantum-Wells Probed by Optically Pumped NMR*
R. Tycko, S. E. Barrett, G. Dabbagh, L. N. Pfeiffer, and K. W. West, Science **268** 1460-3 (1995).
- [5] *Optically Pumped NMR Evidence For Finite-Size Skyrmions in GaAs Quantum-Wells near Landau-Level Filling $\nu=1$*
S. E. Barrett, G. Dabbagh, L. N. Pfeiffer, K. W. West, and R. Tycko, Physical Review Letters **74** 5112-5 (1995).
- [6] *Time-Sequenced Optical Nuclear Magnetic Resonance of Gallium Arsenide*
S. K. Buratto, D. N. Shykind, and D. P. Weitekamp, Physical Review B **44** 9035 (1991).
- [7] *Optically Detected Nuclear Magnetic Resonance and Knight Shift in $Al_xGa_{1-x}As/GaAs$ Heterostructures*
M. Krapf, G. Denninger, H. Pascher, G. Weimann, and W. Schlapp, Solid State Communications **78** 459 (1991).
- [8] *Low Field Electron-Nuclear Spin Coupling in Gallium Arsenide Under Optical Pumping Conditions*
D. Paget, G. Lampel, B. Sapoval, and V. I. Safarov, Physical Review B **15** 5780 (1977).
- [9] *Optically Detected Nuclear Magnetic Resonance of Nuclei within a Quantum Well*
G. P. Flinn, R. T. Harley, M. J. Snelling, A. C. Tropper, and T. M. Kerr, Semiconductor Science and Technology **5** 533 (1990).
- [10] *Fourier-Transform Time-Sequenced Optical Nuclear Magnetic Resonance of Gallium Arsenide*
S. K. Buratto, J. Y. Hwang, N. D. Kurur, D. N. Shykind, and D. P. Weitekamp, Bulletin of Magnetic Resonance **15** 190 (1993).

[11] *Electric Shifts in Magnetic Resonance*

N. Bloembergen, Proc. Colloq. Ampere (Atomes Mol. Etudes Radio Elec.) **11** 39-57 (1962).

[12] *Can Nuclear Magnetic Resonance Resolve Epitaxial Layers?*

S. K. Buratto, D. N. Shykind, and D. P. Weitekamp, Journal of Vacuum Science and Technology B **10** 1740 (1992).

[13] *Optical Detection of Dynamic Polarization of Nuclei in Semiconductors*

A. I. Ekimov and V. I. Safarov, JETP Letters **15** 179 (1972).

[14] *Optical Larmor Beat Detection of High-Resolution Nuclear Magnetic Resonance in a Semiconductor Heterostructure*

J. A. Marohn, P. J. Carson, J. Y. Hwang, M. A. Miller, D. N. Shykind, and D. P. Weitekamp, Physical Review Letters **75** 1364-7 (1995).

[15] *Hole Relaxation and Luminescence Polarization in Doped and Undoped Quantum Wells*

T. Uenoyama and L. J. Sham, Physical Review Letters **64** 3070-3 (1990).

[16] *Spin Relaxation Dynamics in GaAs Quantum Wells: Free Carriers and Excitons*

L. Vina, T. C. Damen, J. E. Cunningham, J. Shah, and L. J. Sham, Superlattices and Microstructures **12** 379-86 (1992).

[17] *Theory of Optical Spin Orientation of Electrons and Nuclei in Semiconductors*

M. I. D'yakonov and V. I. Perel', in Optical Orientation, edited by F. M. a. B. P. Zakharchenya, North-Holland, Amsterdam (1984), Vol. 8, p. 173-258.

[18] *Optical Orientation of the Coupled Electron-Nuclear Spin System of a Semiconductor*

V. G. Fleisher and I. A. Merkulov, in Optical Orientation, edited by F. M. a. B. P. Zakharchenya, Elsevier, Amsterdam (1984), Vol. 8, p. 173-258.

[19] *Radiative Recombination of a 3D-Electron with a 2D-Hole in p-Type GaAs/(GaAl)As Heterojunctions*

W. Ossau, E. Bangert, and G. Weimann, Solid State Communications **64** 711 (1987).

[20] *New Photoluminescence Effects of Carrier Confinement at an AlGaAs/GaAs Heterojunction Interface*

Y. R. Yuan, M. A. A. Pudensi, G. A. Vawater, and J. L. Merz, Journal of Applied Physics **58** 397 (1985).

[21] Principles of Nuclear Magnetism, 1st Edition

A. Abragam, Clarendon Press, Oxford (1961).

[22] *Optical Orientatation in a System of Electrons and Lattice Nuclei in Semiconductors. Experiment*

V. L. Berkovits, A. I. Ekimov, and V. I. Safarov, Sov. Phys.-JETP **38** 169 (1974).

[23] Table of Integrals, Series, and Products, 5th Edition

I. S. Gradshteyn and I. M. Ryzhik, Academic Press, Boston, MA (1994).

[24] Mathematica: A System for Doing Mathematics by Computer, 2nd Edition

S. Wolfram, Addison-Wesley Publishing Company, NY (1991).

[25] Fundamentals of Complex Analysis for Mathematics, Science, and Engineering,

E. B. Saff and A. D. Snider, Prentice-Hall, Inc., Englewood Cliffs, NJ (1976).

Chapter 6: Heterodyne RF Spectrometer for Optical Larmor Beat Detection of Nuclear Magnetic Resonance

I Abstract

We have developed a spectrometer capable of optical Larmor beat detection of nuclear magnetic resonance in semiconductors. The spectrometer employs a modified rf heterodyne receiver to demodulate 0-10 MHz oscillations in luminescence polarization from a 2K sample. By ratioing current between a helium-immersed superconducting magnet longitudinal to the optical axis and a second rotatable perpendicular electromagnet outside the dewar, the magnitude and direction of the total magnetic field at the sample may be varied, allowing rotation studies in a way compatible with optical detection. Complex phase-coherent trinuclear NMR pulse trains, constructed by direct digital synthesis, excite a single untuned transverse rf coil also immersed in helium. Computer synchronization of light shuttering, variations of total magnetic field orientation and magnitude, rf irradiation, and data acquisition enables implementation of both time sequenced and real-time optical NMR experiments.

II Introduction

Epitaxial growth of semiconductor structures allows atomic-layer control of material composition in the design of electronic and optical devices [1, 2]. This effort would be aided by a correspondingly precise method of measuring defects, electron distributions and electric fields. Nuclear magnetic resonance (NMR) could in principle supply this information, but to do so on a single epitaxial structure of $\sim 1 \text{ mm}^2$ requires sensitivity $\sim 10^{12}$ nuclear spins.

Such sensitivity is well beyond the limits of conventional detection of precessing equilibrium magnetization by magnetic induction [3]. Fortunately, large nonequilibrium nuclear magnetizations may be obtained in a semiconductor by optically pumping interband transitions with circularly polarized light [4, 5]. This enhancement alone has allowed high-field pulsed NMR of stacked arrays of quantum wells by magnetic induction [6]. Optical pumping often entails simple modification of a conventional low-temperature NMR probe to accept pumping light delivered by a fiber-optic.

Optical detection of nuclear magnetization provides a large additional enhancement in sensitivity [5, 7]. The degree of circular polarization of luminescence ρ from many direct-gap semiconductors is known to be modulated by nuclear magnetization perpendicular to the optical pumping axis. This mechanism (a non-resonant Hanle-effect depolarization by nuclear hyperfine fields) has been used in steady-state experiments to optically detect low resolution NMR spectra [5, 8-11] and in time-sequenced experiments to record high-resolution NMR spectra [12, 13]. Signal to noise in these experiments is now not limited by Johnson noise in an inductor, but by shot noise in photoluminescence and by the strength of the hyperfine coupling between recombination-electrons and nuclei. Steady-state optical detection involves monitoring luminescence polarization near DC while sweeping CW through nuclear magnetic resonances. Time-sequenced optical NMR additionally demands cycling of the magnetic field orientation between the NMR evolution and luminescence detection periods, thus requiring pointwise acquisition of the desired interferogram.

We recently reported a new optical NMR experiment, utilizing Larmor beat detection (LBD) [14], which lifts these restrictions and allows for the *real-time* optical detection of NMR transients in

semiconductors at fixed magnetic field. This paper describes the associated homebuilt spectrometer, sketched in FIG. 1. A brief summary of LBD facilitates the description of spectrometer requirements.

III Spectrometer Requirements

The LBD method relies on the depolarization of semiconductor luminescence by two precessing nuclear hyperfine fields: a reference field B_N^{ref} , and a signal field B_N^{sig} , each corresponding to distinct nuclear species. The general form of the Lorentzian describing depletion of ρ by a single transverse magnetic field to the case of two single-frequency, circularly-polarized nuclear hyperfine fields is:

$$\rho = \rho_0 \frac{1}{1 + (b_N^{\text{ref}})^2 + (b_N^{\text{sig}})^2 + 2b_N^{\text{ref}} b_N^{\text{sig}} \cos \omega t} \quad (1)$$

where the transverse nuclear field magnitudes in reduced units are defined as

$$b_N^k = \left(\frac{(B_{N,x}^k)^2 + (B_{N,y}^k)^2}{B_H^2 + (B_0 + B_N^{\text{misc}})^2} \right)^{1/2} \quad (k = \text{ref, sig}) \quad (2)$$

and where $\omega = \omega_{\text{sig}} - \omega_{\text{ref}}$ is the difference between signal and reference Larmor frequencies, and ρ_0 is the zero-field luminescence polarization. The denominator in Eq. (2) includes the net miscellaneous (i.e., non-signal and non-reference) nuclear hyperfine field components B_N^{misc} , which remain along the z -axis and add vectorally to B_0 . Together these fields frustrate luminescence depolarization. The Hanle width, $B_H = 1/(\gamma_e T_{1e})$, is the inverse lifetime ($1/T_{1e}$) of the oriented electron converted to field units through its gyromagnetic ratio γ_e . In order to generalize this result to an arbitrary signal spectrum, it is convenient to isolate the components of this response which are linear in an arbitrary set of signal fields $b_N^{\text{sig},i}$, where i indexes resonances in the NMR spectrum. Expanding a generalized version of Eq. (1) in a sum of Taylor series about $b_N^{\text{sig},i} = 0$ and assuming $b_N^{\text{sig},i} \ll b_N^{\text{ref}}$ gives

$$\rho(t) = \rho_0 \frac{b_N^{\text{ref}}(t)}{[b_N^{\text{ref}}(t)]^2 + 1} - 2\rho_0 \sum_i \left(\frac{b_N^{\text{ref}}(t)}{\{[b_N^{\text{ref}}(t)]^2 + 1\}^2} b_N^{\text{sig},i}(t) + O[(b_N^{\text{sig},i})^3] \right) \cos(\omega_i t - \phi_i) \quad (3)$$

where only terms linear in $\cos \omega_i t$ are kept. Also included is an initial phase difference ϕ_i in precession of the isotopes.

From this description of LBD, it follows that: 1) The experiment should be performed at low temperature, where ρ_0 is maximized as in any photoluminescence experiment. 2) Linear response with

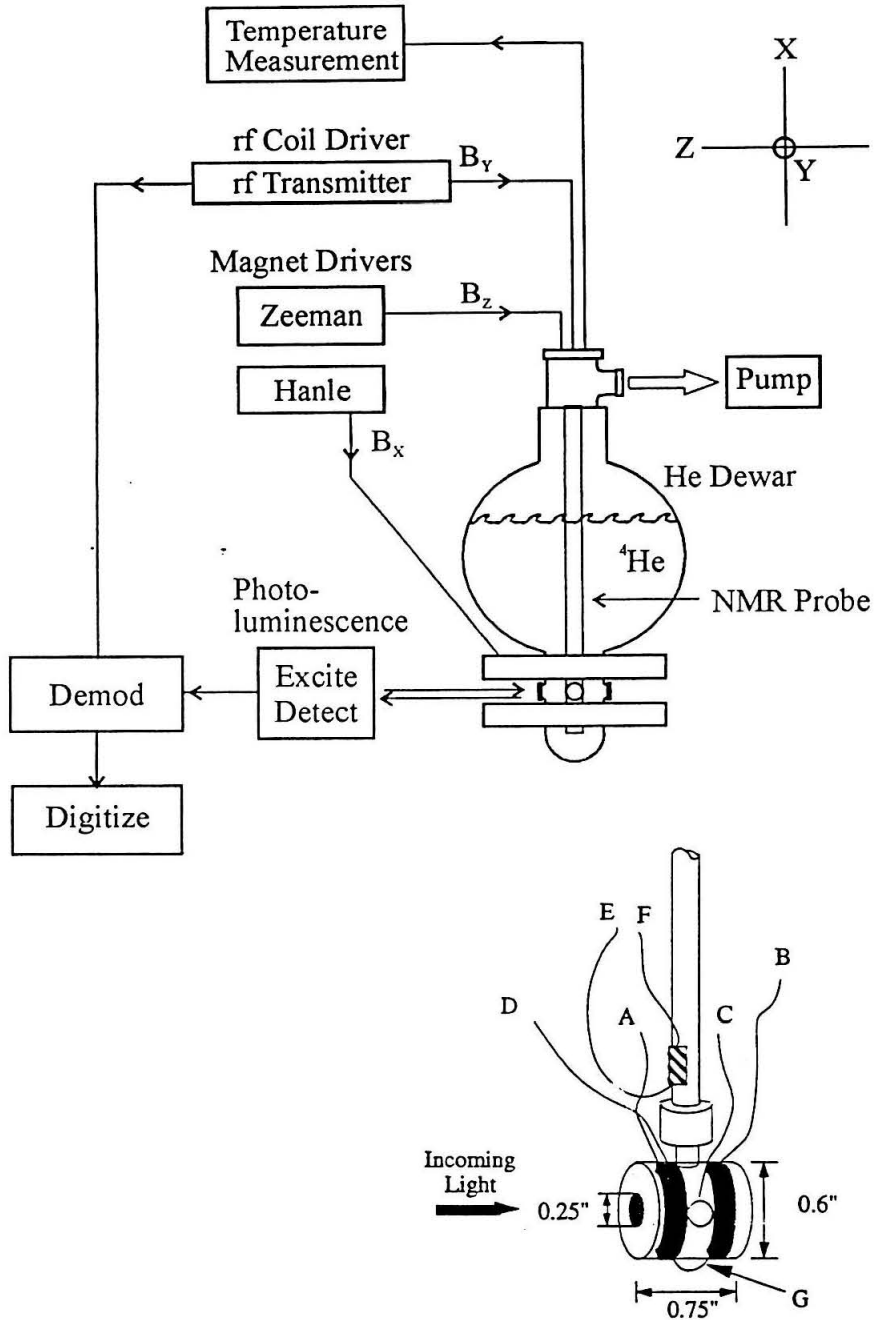


FIG. 1. Block diagram of the optical nuclear magnetic resonance spectrometer.

Inset: Close-up schematic of the probe tip, showing leads for superconducting magnets (A,B), rf coil (C,D), carbon resistor (E,F), and the connection between the superconducting magnets (G).

good sensitivity requires that $b_N^{\text{ref}} \approx 1$ and $b_N^{\text{sig},j} \ll 1$. Magnetization should precess in a longitudinal field no larger than the largest available miscellaneous nuclear field (~ 1 Tesla for many samples). At these static fields, LBD encodes NMR as oscillations of ρ in the frequency range 0.1-10 MHz. 3) As written in Eq. (3), the time dependence of the magnitudes b_N^{ref} and $b_N^{\text{sig},j}$ is due to the transverse relaxation for each separate nuclear hyperfine field. However, if the Fourier components of ρ near the beat frequencies are to be those present in the transients of the *signal* nuclei alone, then it is required that b_N^{ref} change slowly compared to the decay of $b_N^{\text{sig},j}$ (< 1 ms). This is accomplished with either weak on-resonance irradiation or spin-locking of the reference nucleus. 4) Sensitivity to transverse nuclear fields includes dependence on miscellaneous magnetization parallel to the z-axis; therefore, maintenance of *driftless* sensitivity demands that each experiment begin with saturation of magnetization from all isotopes in the sample. 5) As the signal depends on the difference in frequency and phase between precessing nuclear magnetizations, successful signal averaging requires application of phase-reproducible pulses to both signal and reference nuclei. Constructing pulses phase-locked at two frequencies is most easily accomplished by digital synthesis.

IV Cryogenic Equipment

A sample temperature below 2 K is obtained by immersion in liquid helium. The helium is housed in a 4-walled liquid-nitrogen jacketed optical dewar (borosilicate glass, wall thickness 0.23 cm, capacity 10 liters; Pope Scientific custom order). In order to minimize light scatter by boiling liquid helium, the helium is evaporatively cooled into its optically-transparent superfluid phase ($T_\lambda = 2.17$ K) by pumping above the l-He surface through a 1.5" orifice at the top of the dewar. This orifice is connected through approximately 30 feet of 1.5" ID copper pipe to a high-capacity mechanical pump (maximum flow rate of 17.7 CFM or 500 liters/minute; Welch 1397). Experimentally, a pump rate of only ~ 180 liters/minute succeeds in adiabatically cooling the helium below the λ point in about 30 minutes by drawing $\sim 40\%$ (4L) of the liquid helium.

Optical access to the sample is provided by one of three pairs of windows in the dewar tail. Light passes through an outer window, 1.25" in diameter (affixed by Dekhotinski cement), a 1.5" vacuum space, and a 0.75" diameter inner window.

The sample was suspended in the liquid by affixation to a non-magnetic low thermal conductivity 3/16" G-10 fiberglass rod and affixed to the rod with either high vacuum grease (Dow Corning) or varnish (GE 7031). The rod slides down the hollow center of an associated homebuilt G-10 probe supporting a superconducting magnet, an rf coil, and a thermistor. The probe is fed through a copper cap (7.2 cm diameter, 3.4 cm thick) sealed by compression fitting to the copper-topped glass dewar. Because the probe's 9.5 mm outer-diameter central tube takes up such a small fraction of the dewar's neck (4.6 cm ID upper, and 2.8 cm ID lower), it is necessary to minimize convective heat losses by attaching to the probe five horizontal G-10 disks, which serve as baffles positioned at approximately 3.5 cm intervals within the transition region from 77 K to 1-He temperature. A 5 mm ID metal tube passing through the baffles allows liquid helium transfer into the dewar's main chamber. All probe parts were cemented together with an expansion-matched epoxy consisting of 1 part resin (CIBA 6010), 1 part hardener (CIBA 825), and 1 part fine quartz powder or "chop" hardened in air for 8 hours after application.

Electrical access to the probe is via vacuum feed-throughs made from threaded G-10 plugs, center-drilled to pass appropriate leads. The wire or cable is held in place with the expansion-matched epoxy described above and the plug is coated top and bottom with varnish (GE 7031). Two of the leads carry 12 Amps of current to and from a superconducting magnet. The top six inches of each lead is constructed from no. 13 copper wire, while the remaining length is constructed from superconducting wire multiply connected to a parallel no. 16 brass wire by solder joints. Current is carried to an rf coil through a single no. 24 stainless steel coaxial cable, and to a carbon resistor by no. 28 copper wire.

Temperature is measured with a 260 Ω carbon resistor located a few inches above the superconducting magnet [15]. Resistance R versus temperature T , calibrated at 5 temperatures (260 Ω , 293 K; 330 Ω , 77 K; 500 Ω , 10 K; 4.3 k Ω , 4.2 K; 28.5 k Ω , 2.17 K) and fit to the equation $T(R) = \ln(R) / (a + b \ln(R))^2$ with $a = -2.35$ and $b = 0.448$, indicates an average operating temperature for $R = 33 \text{ k}\Omega$ of $T = 1.94 \text{ K}$. With the dewar vacuum space evacuated before running to $\sim 10^{-6}$ Torr and the

outer glass walls of the dewar cooled to 77 K, hold times of ~8 hours were achieved for superfluid helium at this operating temperature following an initial fill of ~12 liters.

V Longitudinal and Transverse Magnets

The Zeeman field B_z was provided by a helium-immersed superconducting Helmholtz pair whose dimensions are indicated in FIG. 1. The pair delivers an NMR-calibrated 20.49 mT/Amp at the sample. Current for the coils (12 A typical) is provided by a DC power supply (Hewlett Packard, model 6264B, 20V/20A) routed through a home-built analog-controlled current limiter. Switching of the limiter's control voltage allowed field cycling from zero to 0.25 T (typical) with risetime $\tau_{\text{RISE}} = 625$ sec, and a fall time $\tau_{\text{FALL}} \leq 100$ msec.

The Hanle field B_x was provided by water-cooled magnets external to the dewar. Each half of the pair (near Helmholtz configuration) consists of 31×31 windings of copper magnet wire (square cross section 1.7 mm on a side) supported by a copper yolk (31 cm outer diameter, 19 cm inner diameter, 5/7 cm wide, 12 cm between coils center-to-center) held in a stainless-steel stand. The rotatable stand allows approximately ± 15 degrees of magnetic field rotation about an axis parallel to the z-axis defined by the Zeeman. The pair delivers an NMR-calibrated 5.65 mT/Amp at the sample. Cycling of the Hanle field (to 67 mT typically, $\tau_{\text{RISE}} = 2.5$ sec, $\tau_{\text{FALL}} = 0.6$ sec) is made possible by modulating an analog control voltage on its associated current source (Hewlett Packard, 6675A, 120V/18A). Analog control voltages for field cycling both magnets is provided by PC-addressable D/A ports on a lock-in amplifier (Stanford Research Systems SR510).

VI The Radiofrequency Magnetic Field

Multifrequency (1-3 MHz) magnetic field pulse trains were delivered to the sample by a single untuned rf coil. The coil is comprised of a pair of 3×3 arrays (i.e., nine turns each, no. 36 copper wire) wound around a hollow 0.25" diameter G-10 plug and separated by 3.6 mm. Multifrequency pulse trains are generated by one channel of a PC-resident D/A board (2 channel, 12-bit, 50 MHz; Signatec AWG502)

while the other channel provides a demodulating reference signal. Rf pulses are attenuated by 17 dB (KAY, 432D), routed through an rf switch (Merrimac, FSCM 12427), and amplified (ENI, A-500) before being sent to the coil. The rf switch protects the sample from exposure audio-frequency pulses inadvertently produced while the D/A board is loading. It is observed that 0.385 Vpp into the rf amplifier results in a linearly-polarized magnetic field at the coil of $2B_1 = 11.6$ mT at 3.264 MHz and $2B_1 = 16.0$ mT at 0.872 MHz.

VII Optics and Determination of Photoluminescence Polarization

The optics employed for excitation and detection of polarization-resolved photoluminescence are illustrated in FIG. 2. Excitation is at a fixed 780 nm. Optical interference filters provide wavelength selection for detection. A standard luminescence modulation protocol [16, 17] is employed to avoid low-frequency noise by modulating and lock-in detecting both the total luminescence and its circularly-polarized components.

Demodulation of photocurrent by the 50 kHz PEM frequency via lock-in amplifier (Stanford Research Systems, SR-530) gives a signal V_{PEM} proportional to the difference ($N_+ - N_-$) between the numbers of σ^+ and σ^- luminescence photons. Demodulation of detector photocurrent by the 2-4 kHz chopper frequency via lock-in amplifier (Stanford Research Systems, SR-510) gives a signal V_{chop} proportional to total luminescence $N_+ + N_-$. The degree of the circular polarization of the luminescence ρ is defined as

$$\rho = \frac{N_+ - N_-}{N_+ + N_-}.$$

The relationship between ρ and the measured voltages is

$$\rho = \frac{V_{\text{PEM}}}{V_{\text{chop}}} \times \frac{(1/2)^{-1} (J_1(\pi/2))^{-1}}{(2/\pi)^{-1} (1/2)^{-1}} = \frac{V_{\text{PEM}}}{V_{\text{chop}}} \times 1.12,$$

where J_1 is a Bessel function.

This demodulation scheme was used in experiments studying variation of steady-state ρ by static longitudinal and transverse magnetic fields. A more complicated scheme is required to demodulate luminescence in the LBD experiment.

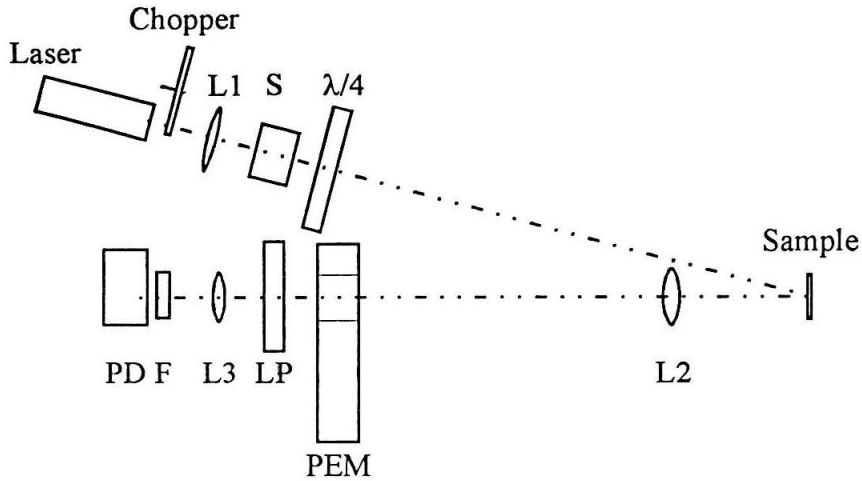
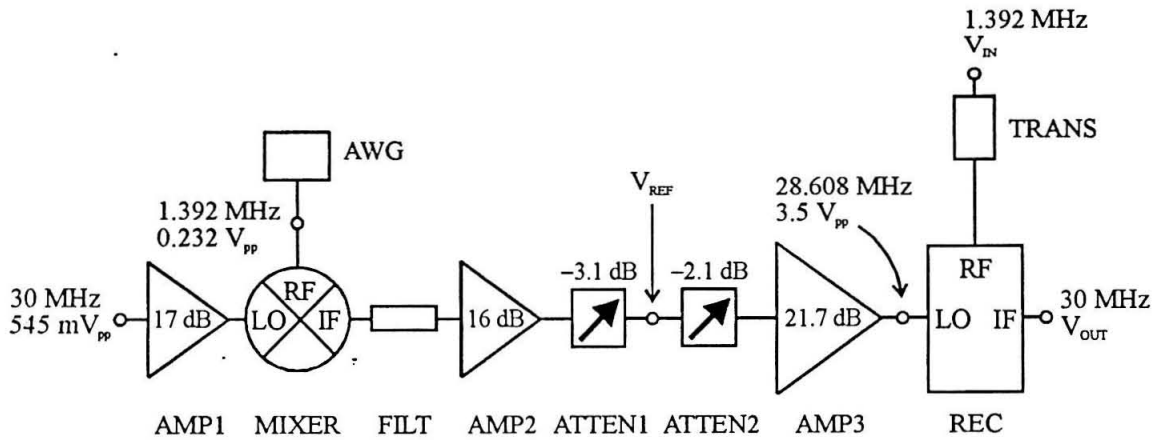


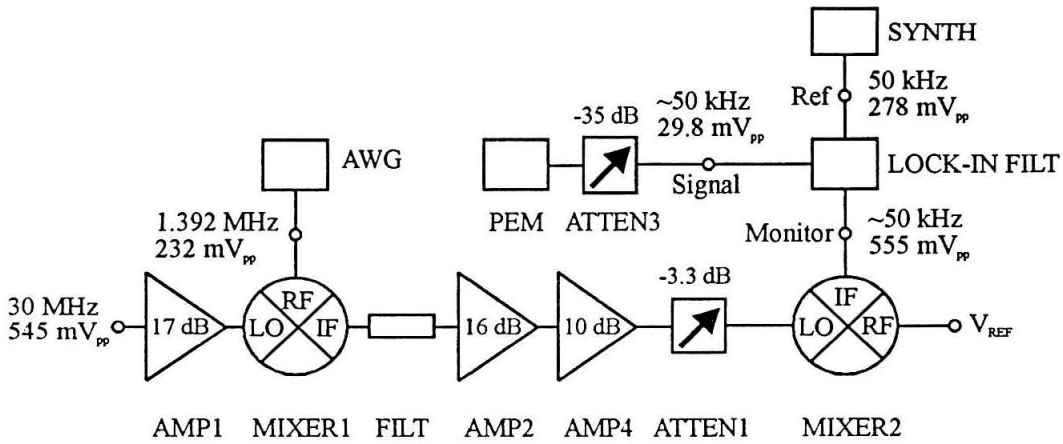
FIG. 2. Optics for excitation and detection photoluminescence.

A laser (Spindler and Hoyer, Inc., model DL25C, single mode GaAs/GaAlAs laser diode) provides ~ 2 mW of continuous 780 nm irradiation, which passes through a chopper (Stanford Research Systems, model SR-540 with SR-541 controller), collimating lens L1, shutter S (Newport, model 846 HP), and $\lambda/4$ plate (Newport, model RSA-1) before striking the sample as circularly polarized light (~ 1 mm diameter spot size). Luminescence is collimated by lens L2, and passes through a photoelastic modulator PEM (Hinds International, Inc., Model 0101 with PEM-80 controller) and linear polarizer LP (Newport, RSA-2). Lens L3 focuses luminescence through an optical interference filter F (Melles Griot, 10 nm FWHM bandpass) and onto photodetector PD (EG&G Optoelectronics, model C30998-030 silicon avalanche photodiode, 400-1000 nm range, 30 MHz bandwidth). The photodetector was mounted on a translation stage (Newport, model 460-XYZ, 10 μm resolution) and biased to -234 V at 22 $^{\circ}\text{C}$ (Hewlett Packard, model 6209B, 320V/1A) through a 10 k Ω current-limiting resistor. Floating the photodiode's DC bias supply with respect to its AC-power ground (i.e., at the wall plug) was required to remove spurious 60 Hz oscillations in photocurrent. During optical NMR experiments (discussed in text), the chopper was removed and the PEM was either left in place or replaced with a single quarter-wave plate (Newport, model RSA-1).



Part	Manufacturer	Serial Number
AMP1	Anzac	AM147
AMP2	Anzac	AMC-143
AMP3	Mini-Circuits	ZFL-2000
ATTEN1	Telonic-Berkeley	8122A
ATTEN2	Kay	0/400A
AWG	Signatec	AWG502
FILT	Cirqtel	FLT/21-28-13/50-3A/3A
MIXER	Mini-Circuits	ZAD-1H
TRANS	TTE	H579-80K-6220

FIG. 3. Detection circuit for demodulation of luminescence oscillating at the Larmor beat frequency.



Part	Manufacturer	Serial Number
AMP4	Anzac	AMC-103
ATTEN3	Kay	432D
LOCK-IN FILT	Stanford Research Systems	SR-510
MIXER	Mini-Circuits	ZAD-1H
SYNTH	General Radio	1168

FIG. 4. Detection circuit for demodulation of luminescence oscillating at the Larmor beat plus PEM frequency.

VIII Demodulating Photoluminescence Polarization During LBD

In order to gain greater detection bandwidth, both the chopper and the PEM are removed from the optical path during the LBD experiment. With the PEM replaced by a single $\lambda/4$ plate, detector photocurrent is related to only one circular component of the luminescence (σ^+ and σ^-), which oscillates at the LBD frequency alone.

A conventional NMR receiver would now use heterodyne demodulation to mix the signal down to audio frequency before digitization [18]. In heterodyne detection, the signal of interest, usually at a radiofrequency (RF, at 60-200 MHz for example), is demodulated once by a local oscillator frequency (LO, at 30-170 MHz for example) to a fixed intermediate frequency (IF, 30 MHz is standard). Demodulation of IF to audio takes place with phase-sensitive detection. Heterodyne detection minimizes the effects of pickup by moving the signal of interest away from the transmitter frequency as early in the detection process as possible. Its primary advantage for our application, however, is that it enables convenient phase-sensitive detection over a range of RF frequencies.

Implementing heterodyne detection in the LBD experiment required modification of a conventional high-frequency NMR receiver to produce an LO which is phase-coherent with signal at the Larmor beat (LB) frequency. The required circuitry is illustrated in FIG. 3. A 30 MHz reference, phase coherent with the spectrometer's IF (30 MHz), is mixed with the LB (1.392 MHz) reference produced by the same D/A board that synthesizes transmitter pulses. Of two resulting sidebands, only the lower one (28.608 MHz) survives the 30 MHz lowpass filter (FILT), and contributes to the reference voltage V_{REF} , which is sent to the single-sideband receiver (REC). A 10:1 transformer (TRANS) impedance matches the 500 Ω photodiode amplifier to the 50 Ω receiver port RF, and serves also as an 80 kHz high-pass filter to keep unmodulated signal from saturating the receiver. Following REC, the signal is demodulated from IF as usual and digitized (Nicolet, model 4094A 2 MHz digital oscilloscope with no. 4562 insert).

For some experiments, the PEM was left in the optical path. In this case detector photocurrent contains ± 50 kHz PEM-frequency sidebands of the LB frequency, each proportional to $N_+ - N_-$. The required demodulation circuitry appears in FIG. 4. The square-wave PEM reference is 50 ± 5 kHz center-pass filtered into a sine wave using a lock-in amplifier (SYNTH determines the center-pass frequency,

while the width of the pass-band is determined internally), and mixed to put ± 50 kHz sidebands on the LO reference, synthesized as above. When mixed with photocurrent signal, V_{REF} gives rise to four signals at V_{OUT} : two at 30 MHz and two extraneous signal in ± 100 kHz sidebands, filtered out at the audio stage before digitization.

IX Time-Sequencing and Computer Control

The timeline for a representative experiment appears in FIG. 5. Following saturation pulses SAT, optical pumping (for a time τ_L) builds up nuclear magnetization at high magnetic field B_Z . The field is cycled adiabatically to a low-field transverse geometry B_X , and signal-nucleus magnetization evolves for a time t_1 in the dark in this transverse field. The light is turned back on while the field is cycled to a longitudinal geometry after which remaining magnetization is read out during t_2 by Larmor beat optical detection at high field. Here SAT represents a train of ten $\pi/2$ pulses (10 ms apart) applied to each of the principle isotopes (^{69}Ga , ^{71}Ga , ^{75}As) to provide a reproducible condition of saturation or null spin order before each shot. The evolution period here encodes a spin-echo, where magnetization begins and ends along the transverse static field. An optional θ -pulse before the echo may be used to destroy a fraction of magnetization, providing a test for linear response.

Pulses given at high field to the principle isotopes ($\text{RF}_{\text{sig,Z}}$, RF_{misc} , and RF_{ref}), as well the low-field pulses evolving the signal nucleus ($\text{RF}_{\text{sig,X}}$), originate in one channel of a PC-resident D/A board. The other channel provides a reference frequency directly to the receiver at the Larmor beat frequency ($\text{RF}_{\text{ref,sig}}$). An external logic generator (Interface Technology, 40 MHz, model RS-670) is used to trigger the shutter, D/A board, and a transmitter-protecting rf-switch (as described in section VI), and also controls acquisition of each data point via pulses to a digital oscilloscope.

As noted previously, longitudinal and transverse field values are set via an analog input on the appropriate power supply, where the control voltage is provided by a GPIB-addressable D/A port on a lock-in amplifier. A field cycling event is initiated when the PC sends the appropriate GPIB command to the lock-in. The PC uses software polls to the system timer [19] (an *ftime()* call in C or C++), updated

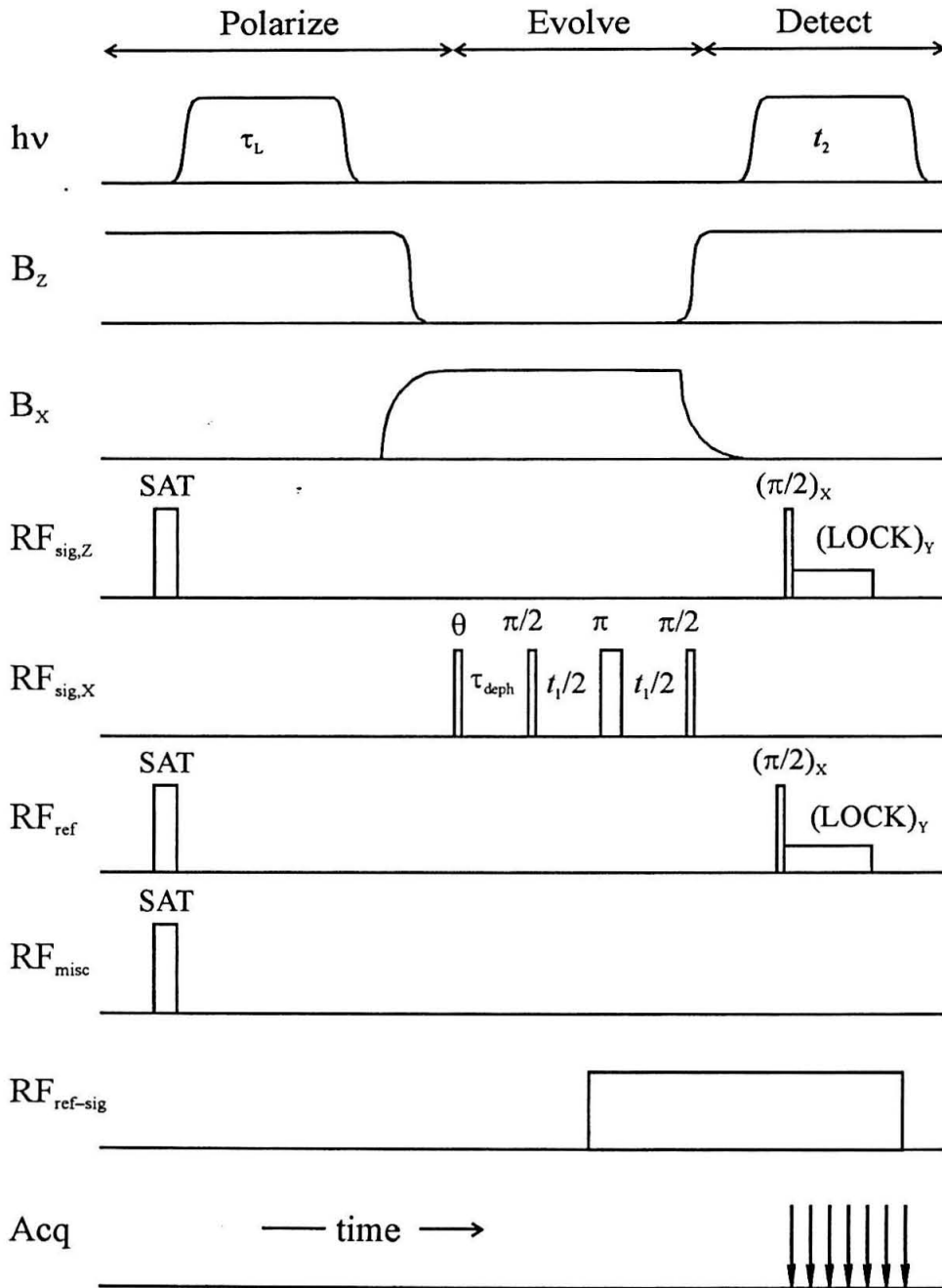


FIG. 5. Timeline of a representative optical NMR experiment.

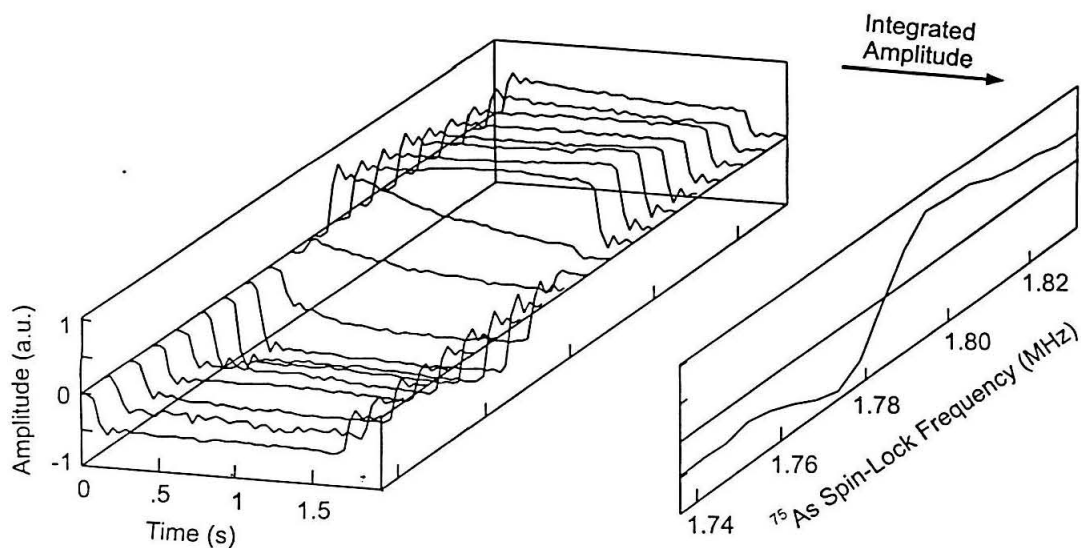


FIG. 6. “Tuneup” experiment for Larmor beat optical detection.

Following $\tau_L = 5$ s of optical nuclear polarization, a $3.35 \mu\text{s}$, 3.184 MHz, $\pi/2$ pulse to ^{71}Ga creates transverse nuclear “signal” field, sustained in-plane by a phase-shifted on-resonance 0.65 mT spin lock. A ~ 0.7 mT ^{75}As spin lock provides the transverse “reference” field. Luminescence polarization is demodulated by the appropriate beat frequency, filtered, and digitized to give the observed transients. Each transient shows a slow decay to an asymptote. The decay ($T_{1\rho} \sim 1$ s) is due to dephasing of spin-locked ^{71}Ga magnetization, while the asymptote observes in-plane magnetization resulting from steady-state response of both nuclear magnetizations to their respective spin locks. The ^{75}As irradiation frequency is swept to empirically optimize the Larmor beat response for given ^{71}Ga magnetization.

18.2 times per second, to determine event timing. Care must be taken in writing pulse programs to allow for the resulting worst-case 60 ms jitter in synchronization of field-cycling events with rf output.

Each experiment is run by a compiled C-language program. An example “pulse program” appears in the Appendix.

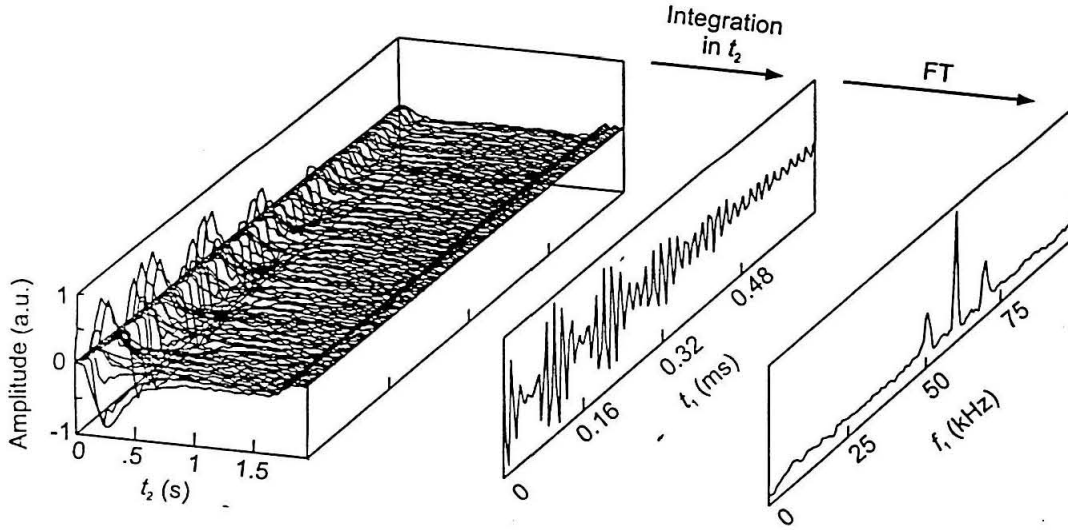


FIG. 7. Time-sequenced spin-echo spectrum recorded by Larmor beat detection.

With LBD optimized as in FIG. 6., ^{71}Ga is evolved under a spin-echo sequence for an incremented time t_1 prior to Larmor beat detection in t_2 . The entire data set was recorded in less than 30 minutes. Each transient in t_2 is integrated and plotted versus t_1 to yield a ^{71}Ga spin-echo interferogram. The Fourier transform of the interferogram gives the spin echo spectrum.

X Experiments

FIG 6. shows data from a simple “tuneup” experiment, in which, with no evolution period, and optical pumping and detection occurring at a fixed 0.24 T, Larmor beat transients are recorded in t_2 as spin-locked ^{71}Ga magnetization decays. Equation (3) predicts optimal small-signal response to ^{71}Ga magnetization when $b_{\text{N}}^{\text{ref}} = 1/\sqrt{3}$ or

$$\left(\frac{(B_{\text{N},x}^{\text{ref}})^2 + (B_{\text{N},y}^{\text{ref}})^2}{B_{\text{H}}^2 + (B_0 + B_{\text{N}}^{\text{misc}})^2} \right)^{1/2} = \frac{1}{\sqrt{3}}. \quad (4)$$

It would appear that optimizing small signal response to ^{71}Ga magnetization requires detailed knowledge of reference, miscellaneous, static, and Hanle fields. The experiment of FIG. 6 demonstrates, however, that LBD can be optimized empirically by sweeping the reference-nucleus (^{75}As) irradiation frequency. For fixed ^{75}As spin-lock power, subsequent experiments are run with the ^{75}As offset frequency that shows the largest LBD response during decay of ^{71}Ga magnetization.

Data from a time-sequenced ^{71}Ga spin-echo experiment is shown in FIG. 7. In this experiment, the phases of the first two pulses of the spin echo sequenced are stepped with each t_1 point. The net effect of such time-proportional phase incrementation (TPPI) [20], is to shift the spectrum away from zero frequency in ω_1 , and separate it from artifacts due to drifts in the total signal amplitude. For the spin echo sequence $(\pi/2)_{\phi_1} - (\pi)_{\phi_2} - (\pi/2)_X$, where $\phi_1 = \omega_{\text{TPPI},1} t_1$ and $\phi_2 = \omega_{\text{TPPI},2} t_1$, the spectrum is shifted to a frequency $\omega_{\text{eff}}/2\pi = (\omega_{\text{TPPI},1} - 2\omega_{\text{TPPI},2})/2\pi = 60 \text{ kHz}$ in the Figure.

The triplet structure in this spin echo spectrum has been assigned to a quadrupole coupling of the ^{71}Ga nucleus to an electric field gradient [14]. The observed mean quadrupole splitting varied between Dewar cooling cycles, implicating strain as the source of electric field gradient. This is corroborated by the observation here that the splitting can be made to vanish by affixing the sample to the G-10 probe using a small amount of vacuum grease and slow cooling the sample from room temperature to 77 K over a six-hour period. Cooling to 1-He temperature occurs over a 20 minute span.

XI Shot-Noise-Limited Detection

In experiments where t_1 noise is negligible compared to noise during Larmor beat detection (t_2 noise), calculations show that the dominant source of noise in the experiment is shot noise [2] from the detected luminescence. Two other possible sources of noise during Larmor beat detection are found to be negligible. They are (1) noise from the pre-amplifier of the heterodyne rf spectrometer used to mix down the luminescence signal modulated at the Larmor beat frequency, and (2) thermal Johnson noise in the feedback resistor of the avalanche photodiode (at room temperature).

Shot noise in this experiment has two contributing sources: the photon counting statistics (Poisson statistics) associated with optical detection, and the current counting statistics (also Poisson) associated with the dark current in the avalanche photodiode. The optical shot noise current is given by

$$I_{n,\text{optical}} = \left[2qP_o R^o M^2 FB_c \right]^{1/2} \quad (5)$$

where q is the electronic charge, P_o is the optical power, R^o is the unity gain responsivity of the photodiode, M is the avalanche gain, F is the excess noise factor intrinsic to the avalanche process, and B_c is the bandwidth cutoff frequency. The unity gain responsivity is given by

$$R^o = \frac{\eta q}{h\nu} \quad (6)$$

where η is the quantum efficiency of the photodiode, and $h\nu$ is the photon energy. For these experiments, $\eta = 0.77$, $M = 124$, and $F = 4.43$. In a typical experiment, the total luminescence power detected (P_o) is 1.5 nW (6×10^9 photons/sec for $\lambda = 830\text{nm}$). The resulting optical shot noise density is

$$\tilde{I}_{n,\text{optical}} = 2.9 \text{ pA}/\sqrt{\text{Hz}} \quad (7)$$

where

$$\tilde{I}_n = I_n / \sqrt{2B_c} . \quad (8)$$

The shot noise associated with the dark current of the avalanche photodiode is given by

$$I_{n,\text{dark}} = \left[2q(I_{\text{ds}} + I_{\text{db}} M^2 F) B_c \right]^{1/2} \quad (9)$$

where I_{ds} is the dark surface current and I_{db} , the dark bulk current. For these experiments the dark current shot noise density is

$$\tilde{I}_{n,\text{dark}} = 0.8 \text{ pA} / \sqrt{\text{Hz}} = (\text{NEP}) R^o M , \quad (10)$$

where the second equation relates it to noise equivalent power (NEP).

The total shot noise density $\tilde{I}_{n,\text{shot}}$ is the rms sum of the optical and dark current shot noise contributions:

$$\tilde{I}_{n,\text{shot}} = \left(\tilde{I}_{n,\text{optical}}^2 + \tilde{I}_{n,\text{dark}}^2 \right)^{1/2} = 3.0 \text{ pA}/\sqrt{\text{Hz}} \quad (11)$$

The measured noise during Larmor beat detection (i.e., during t_2) is found to be

$$\tilde{I}_{n,\text{measured}} = 3.3 \text{ pA}/\sqrt{\text{Hz}} \quad (12)$$

which is within 10% of the calculated shot noise. The sensitivity is thus said to be shot noise limited. Another point of reference is that the resulting SNR is within a factor of 2 of a hypothetical ultrafast photon counter with the same quantum efficiency. This indicates that the sources (e.g., laser fluctuations at the Larmor beat frequency) are no more than 50% of the shot noise density (accounting for rms summation of the two noise densities).

XII Conclusions

We have developed a spectrometer capable of optical Larmor beat detection of nuclear magnetic resonance in semiconductors. The spectrometer includes a 2 K probe with superconducting magnetic field coils, an orthogonal electromagnet allowing field-rotation studies, optics for exciting and detecting polarization-resolved photoluminescence, a transmitter for delivering complex multinuclear pulse sequences, and a heterodyning receiver. Computer synchronization of light shuttering, variation of magnetic field orientation and magnitude, rf irradiation, and data acquisition enables implementation of both time-sequenced and real-time optical NMR experiments. Noise levels can be understood quantitatively in terms of luminescence shot noise and the physics of avalanche photodiodes.

XIII Acknowledgments

This work was funded by the NSF program in Materials Synthesis and Processing and by NASA through the Caltech President's Fund. We thank A. Ksendzov, J. Liu, and F. Grunthaner of the NASA Jet Propulsion Laboratory's Center for Space Microelectronics Technology for sample preparation and luminescence characterization, and L. Burnett and A. Perry for cryogenics advice.

XIV Appendix**CMREX15a.C**

John Marohn
06-19-95

SPIN ECHO t1 with LARMOR BEAT DETECTION IN t2, with incrementation of:
- t1 during evolution
- reference nucleus frequency during evolution

INCLUDE FILES

```
#include "srcmr.h"      SR function prototypes
#include "iticmr.h"     ITI function prototypes
#include "awgcmr.h"     AWG function prototypes
#include "niccmr.h"     NIC function prototypes
```

USEFUL MASKS

The "<<" operator is a C-language construct meaning "left shift". You will see below how these masks are used to define an ITI state. The number to the right of the "<<" operator corresponds to the channel number on the ITI pulse distribution box.

ITI CHANNEL ASSIGNMENTS

```
#define BLANK (0)
#define TRG_AWG (1 << 2)
#define TRG_NIC (1 << 3)
#define TRG_REC (1 << 4)
#define OPEN_S (1 << 6)
#define CLOSE_S (1 << 7)
#define SW1_RF (1 << 8)
#define SW2_RF (1 << 9)
#define EP_NIC (1 << 11)
#define TRG_SCP (1 << 13)
```

OTHER MASKS

```
#define PI 3.141592
#define hPI 1.570796
```

These masks are used below to determine if you get a copy of all ITI GPIB cmds sent to the screen.

```
#define ECHO 1
#define NOECHO 0
```

DEBUGGING FLAGS

These logical debugging flags activate code near the end of the program which prints out useful diagnostics.

```
#define PAUSE 0      1 = pause every loop increment, 0 = don't pause
#define ITIDIAG 0    1 = print iti diagnostics, 0 = don't
#define AWGDIAG 0    1 = print awg diagnostics, 0 = don't
#define EVENTS 1     Print message during main events
```

Debugging tricks to see pulse sequence on scope:

- 1) Set PAUSE 1 above
- 2) Edit all amplitudes down to half or less of normal value, except the first pulse. This assures that scope triggers on first pulse.
- 3) Edit tONP down to one microsecond
- 4) Edit pulse times to ca 10-100 microseconds [as long as possible]
- 5) Edit delay times to ca 100 microseconds [as short as possible]
- 6) Run pulse program and manually edit main loop count to 1000
- 7) Remember to edit things back to reasonable values for real expt

MAIN PROGRAM

The main program writes to two files, temp.nic and temp.dat, which should be renamed when the program is done.

```
main( int argc, char *argv[] )
{
    ititype iti;  Interface Technology RS-670 data structure from "iticmr.h"
    awgtype awg;  Signatech AWG502 data structure from "awgcmr.h"
    nictype nic;  Nicolet 4094A data structure "niccmr.h" */
    srtype sr;   Stanford Research Systems lock-in amp data struct "srcmr.h"
    tcntr ticker; Timer function from "gpibcmr.h"
    int loop;    Main loop counter
```

```
FILE *fpNIC=stdout; Output file pointer for NIC settings
FILE *fpDAT=stdout; Output file pointer for NIC data
```

FREE VARIABLES

```
#define ifCYC 1    1=include field cycling code, 0=don't
#define nMAIN 1   Number of times to run ITI [usually 1]
#define DT1 2     Number of dummy t1 points [no lim]
#define NT1 25    Number of real t1 points [no lim]
#define NT2 20    Number of t2 points [0-7936]
```

```
SR510 x5 controls the zeeman field (zV parameters)
SR510 x6 controls the hanle field (hV parameters)
```

The lock-in x5/x6 resolution is 0.0025 Volts; you should set values to be exact to within this resolution.

```
#define LOCK_IN "SR510"
```

```
#define zPort 5
#define hPort 6
```

```
#define zVpolarize 2.4900
#define hVpolarize 0
#define zVevolve 0
#define hVevolve 2.7550
#define zVdetect 2.4900
#define hVdetect 0
```

All times in the pulse program below -- for both the AWG and the ITI -- are really in units of 40 MHz clock cycles (timetype = unsigned long int). It's really tedious to enter times in these funny units. The macros TIME(), SEC(), MILLISEC(), and MICROSEC() convert the time in brackets into time in clock ticks, so you don't have to worry about the conversion.

The LONGEST TIME that can be represented this way is about 100 seconds. The #define is a C-language construct which allows you to symbolically represent

constants in the program. The text following the variable is pasted literally into the code where the variable appears, *_before_* compilation. Keep in mind that the "variable" name following and #define statement is gone from the code by compile time, so be very careful to treat such "variables" as constants in the code. The precompiler construct #if (nonzero number) --> #endif allows for conditional compilation. The construct is handy for editing out large blocks of code without resorting to commenting them out.

```
#define tONP1      TIME(1,500,1,0) ONP Time (0.25-63.75s)
#define tONP2      TIME(0,500,1,0) ONP Time (0.25-63.75s)
#define tShut      TIME(0,100,0,0) Delay for shutter to open (25-6375ms)
#define tVcycleUP  TIME(2,500,0,0) Delay for Hanle field Bx cyc (25-6375ms)
#define tVcycleDLY TIME(0,200,0,0) Incr for Zeeman field Bz cyc (25-6375ms)
#define tVcycleDOWN TIME(1,200,0,0) Delay for Bx,Bz field cyc (25-6375ms)
#define tVcyclePLAY TIME(0,200,0,0) Extra delay for Bx,Bz cycle (25-6375ms)
```

We want short variable names for what follows. I'll try to stick to some convention.

```
t_ time variable
a_ amplitude variable
c_ carrier, or frequency variable
p_ phase variable
```

```
_S_ signal nucleus variable, typically for Ga(71)
_M_ miscellaneous nucleus variable, typically for Ga(69)
_R_ signal nucleus variable, typically for As(75)
```

```
#define tSi      TIME(0, 0, 10, 0) Initial pulse TIME
#define tDeph    TIME(0, 12,500, 0) Dephasing TIME
#define tSre     TIME(0, 0, 3,950) Preparation pulse TIME
#define tSpe     TIME(0, 0, 3,950) Signal Pulse TIME
#define tSpd     TIME(0, 0, 3,950) Signal Pulse TIME
#define tMp      TIME(0, 0, 3,750) Misc Pulse TIME
#define tRp      TIME(0, 0, 6, 50) Ref Pulse TIME
timetype t1 =  TIME(0, 0,150, 0); Initial Evolution TIME
#define delt1    TIME(0, 0, 0, 0) HALF Evolution TIME STEP

#define delt2    TIME(0, 50, 0, 0) EPI(fast=200us-500ns) EPII(slow=inf-200us)
#define tLock    TIME(0,500, 0, 0) Lock time [50-12750ms]
#define tPLock   TIME(0,500, 0, 0) Post lock time [50-12750ms]
```

There is need in the AWG pulse program for a long table which is looped many times to give a delay. If you want the pulses before and after the delay to be phase coherent, then the carrier must be cyclic modulo this table length. tLong of 125 microseconds requires carriers be modulo 8 KHz.

```
#define tLong    MICROSEC(125)
#define tVeryLong MICROSEC(500)
```

Remember that carriers must be in multiples of 8 kHz

```
#define cSe      1.000 Sig Carrier (MHz) EVOLUTION FREQ
#define cSd      3.184 Sig Carrier (MHz) DETECTION FREQ
#define cM       2.504 Misc Carrier (MHz) FREQ
double cR =     1.856; Ref Carrier (MHz) FREQ
#define delcR    0.000 Ref Carrier (MHz) step FREQ
#define oBsr     0.000 Beat offset (MHz) FREQ
#define oBmr     0.000 Beat offset (MHz) FREQ
#define tppi1    0.020 2x tppi of pi/2 pulse
#define tppi2    -0.040 2x tppi of pi pulse
```

```

#define pBsr          0    Phase of beat signal
#define pBmr          0    Phase of beat signal
#define pSl           hPI   Phase of signal nucleus spin lock
#define pRl           hPI   Phase of reference nucleus spin lock

#define aSi          1400   Initial dephasing AMP
#define aSr           400   Preparation pulse AMP
#define aSp           400   Pulse AMP
#define aMp           0     Pulse AMP
#define aRp           0     Pulse AMP
#define aSl           150   Lock pulse AMP
#define aMl           0     Lock pulse AMP
#define aRl           150   Lock pulse AMP
#define aSd           300   Dephase pulse AMP
#define aMd           0     Dephase pulse AMP
#define aRd           0     Dephase pulse AMP

#define aBsr          307   Beat reciever AMP
#define aBmr          0     Beat reciever AMP

```

CONSTRAINED VARIABLES

```

timetype tWaitUntil1 = TIME(0, 1, 0, 0);
timetype tWaitUntil2 = TIME(0, 1, 0, 0);
timetype tWaitUntil3 = TIME(0, 1, 0, 0);

double   cBsr        = 1.000;  Beat carrier (MHz)  FREQ
double   cBmr        = 1.000;  Beat carrier (MHz)  FREQ

double   p1          = 0.0;    phase of Signal pi/2 pulse, computed from tppi1
double   p2          = 0.0;    phase of Signal pi pulse, computed from tppi2

int      t2          = -2*NT2;  Initial t2 point count

fvars V1={0,0,0,0,0}; Stores V1 vars for F1 macro: .freq,.amp,.ph,.dc,.slope
fvars V2={0,0,0,0,0}; Stores V2 variables for F2 macro
fvars V3={0,0,0,0,0}; Stores V3 variables for F3 macro
fvars V4={0,0,0,0,0}; Stores V4 variables for F4 macro
fvars V5={0,0,0,0,0}; Stores V5 variables for F5 macro
fvars V6={0,0,0,0,0}; Stores V6 variables for F6 macro

```

SR LOCK-IN PRELIMINARIES

```

find_SR(&sr,LOCK_IN);          Get SR GPIB address and clear

sr.header.x5init=zVpolarize;   Volts -10.24 to +10.24
sr.header.x6init=hVpolarize;   Volts -10.24 to +10.24
sr.header.display=0;           0=(x,y) and 2=(r,phi)
sr.header.bandpass=1;          0=OUT, 1=IN
sr.header.dynres=0;             0=LOW, 1=NORM, 2=HIGH
sr.header.sens=MILLIVOLTS(50); gain
sr.header.pretc=srMILLISEC(30); time constant
sr.header.posttc=0;             0=none

write_param_SR(&sr); if (EVENTS) printf("\ninitialize SR510");

```

NIC PRELIMINARIES

```

fpNIC=myopen("temp.nic","w");  Open file for NIC settings output
fpDAT=myopen("temp.dat","w");  Open file for NIC data output

alloc_NIC(&nic);               Allocate memory for 2 x 8k NIC data.

```

```

find_NIC(&nic);           Initialize NIC structure
beep_NIC(&nic);          Is NIC working? MakeNIC beep
enslave_NIC(&nic);       Put NIC under computer control
read_param_NIC(&nic);    Get NIC parameters: number of channels, etc
read_norm_NIC(1,&nic);   Get NIC CH1 normalization constants
read_norm_NIC(2,&nic);   Get NIC CH2 normalization constants
release_NIC(&nic);       Release NIC from computer control

```

```

print_param_NIC(fpNIC,1,&nic);
print_param_NIC(fpNIC,2,&nic);
print_norm_NIC(fpNIC,1,&nic);
print_norm_NIC(fpNIC,2,&nic);

```

```
enliven_NIC(&nic);  Put NIC in live-hold-next mode
```

AWG and ITI PRELIMINARIES

```

alloc_AWG(&awg);  Allocate memory for AWG 2 x 64k waveform data
find_ITI(&iti);   Get ITI GPIB address and clear

```

BEGIN MAIN LOOP

```

for ( loop = 0 ; loop <= (NT1+DT1); loop++ )
{

```

INCREMENT VARIABLES

```

printf("\nLOOP:%d",loop);
printf("\n");

```

```

if ( loop > DT1 )
{

```

```

    cR = cR + delcR;
    t1 = t1 + delT1;
    p1=2*PI*tpp11*ttoMICROSEC(t1);
    p2=2*PI*tppi2*ttoMICROSEC(t1)+PI;

```

```

    printf("\n    t1=%f usec",ttoMICROSEC(t1));
    printf("\n    cR=%E MHz",cR);
    printf("\n    p1=%E rads",p1);
    printf("\n    p2=%E rads",p2);
    printf("\n");
}

```

```

cBsr = cSd - cR + oBsr;           Cycle ref FREQ during detection

```

```

cBmr = cSd - cM + oBmr;           Cycle ref FREQ during detection

```

```

t2 = t2 + NT2 + 1;

```

```

printf("\n    cBsr=%E MHz",cBsr);
printf("\n    cBmr=%E MHz",cBmr);
printf("\n    t2=%d pts",t2);
printf("\n");

```

LOAD ITI AND RUN AND FIELD CYCLE

You *MUST* load the AWG before the ITI, because the first thing the ITI does after it's triggered is to trigger the AWG to give saturation pulses.

```

if ( loop != 0 )
{

```

```

    reset_AWG(&awg);           if (EVENTS) printf("\nreset awg");
    send_AWG(&awg);           if (EVENTS) printf("\nloaded awg");
    etrigger_AWG(&awg);       if (EVENTS) printf("\next trig awg");

```

```

clear_ITI(&iti);          if (EVENTS) printf("\ncleared iti");
send_ITI(NOECHO,&iti);   if (EVENTS) printf("\nsent iti");
trigger_ITI(&iti);      if (EVENTS) printf("\nRUNNING: trigger iti");

start_t(&ticker); Initialize starting time marker RIGHT AFTER iti trigger
stop_t(&ticker); Initialize stopping time marker

#if ifCYC

In calculating the field cycling delays, ignore the microsecond pulses

tWaitUntil1 = tShut + 10*tDeph + tONP1 + 10*tDeph + tONP2 + tShut;

waituntil(&ticker,tWaitUntil1);
    write_analog_SR(&sr,hPort,hVevolve);
    if (EVENTS) printf("\nVcycle: Hanle evolve");

tWaitUntil2 = tWaitUntil1 + tVcycleDLY;

waituntil(&ticker,tWaitUntil2);
    write_analog_SR(&sr,zPort,zVevolve);
    if (EVENTS) printf("\nVcycle: Zeeman evolve");

tWaitUntil3 = tWaitUntil1 + tVcycleUP + tDeph + 2*t1 + tVcyclePLAY;

waituntil(&ticker,tWaitUntil3);
    write_analog_SR(&sr,hPort,hVdetect);
    write_analog_SR(&sr,zPort,zVdetect);
    if (EVENTS) printf("\nVcycle: detect");

#endif
}

CREATE AWG DATA

init_AWG(&awg);          Initialize AWG structure

awg.header.sclk=40.0E6;
awg.header.tmode=1;
awg.header.EDO=0;

awg.header.offsl=2048; awg.header.offss=2048;
awg.header.out1= 1; awg.header.out2= 1;
awg.header.atten1=255; awg.header.atten2= 64;
awg.header.filt1= 4; awg.header.filt2= 4;

V1.freq=cSe*2*PI/40.0;
V6.freq=cSd*2*PI/40.0;
V3.freq=cM*2*PI/40.0;
V5.freq=cR*2*PI/40.0;
V2.freq=cBsr*2*PI/40.0;
V4.freq=cBmr*2*PI/40.0;

addsignal( 0,          DC,DC,NANOSEC(400), awg);
addsignal( 1, F6(aSd,0,t)+DC,DC,    tSpd, awg);
addsignal( 2,          DC,DC,    tLong, awg);
addsignal( 3,          DC,DC,tVeryLong, awg);
addsignal( 4, F5(aRd,0,t)+DC,DC,    tRp, awg);
addsignal( 4, F3(aMd,0,t)+DC,DC,    tMp, awg);

addsignal( 5, F1(aSi,0,t)+DC,DC,tSi, awg);

addsignal( 6, F1(aSr, p1,t)+DC,DC,    tSre, awg);
addsignal( 6,          DC,DC, t1&tLong, awg);
addsignal( 7, F1(aSp, p2,t)+DC,DC,    tSpe, awg);
addsignal( 7, F1(aSp, p2,t)+DC,DC,    tSpe, awg);
addsignal( 7,          DC,DC, t1&tLong, awg);

```

```

addsignal( 8, F1(aSp, 0,t)+DC,DC,      tSpe, awg);

addsignal( 9,          DC, F2(aBsr,0,t)+F4(aBmr,0,t)+DC,tLong, awg);
addsignal(10,F5(aRp, 0,t)+DC, F2(aBsr,0,t)+F4(aBmr,0,t)+DC,  tRp, awg);

addsignal(10,          F3(aMp,0,t)+F5(aRl,hPI,t)+DC,
                  F2(aBsr,0,t)+F4(aBmr,0,t)+DC, tMp, awg);
addsignal(10,      F6(aSp,0,t)+F3(aMl,hPI,t)+F5(aRl,hPI,t)+DC,
                  F2(aBsr,0,t)+F4(aBmr,0,t)+DC, tSpd, awg);
addsignal(11,      F6(aSl,hPI,t)+F3(aMl,hPI,t)+F5(aRl,hPI,t)+DC,
                  F2(aBsr,0,t)+F4(aBmr,0,t)+DC,tLong, awg);
addsignal(12,          DC,
                  F2(aBsr,0,t)+F4(aBmr,0,t)+DC,tLong, awg);

initialize(&awg);
repeat(10,&awg);          10 sets of "killer" pulses
    signal(1,1,&awg);      Pi/2 Ga(71)
    signal(2,tDeph/tLong,&awg); Dephase Ga(71)
endrepeat(&awg);
repeat(tONP1/(500*tVeryLong),&awg); 1st half of ONP
    signal(3,250,&awg);
    signal(3,250,&awg);
endrepeat(&awg);
repeat(10,&awg);          10 sets of "killer" pulses
    signal(4,1,&awg);      Pi/2 As(75), Ga(69)
    signal(2,tDeph/tLong,&awg); Dephase As(75), Ga(69)
endrepeat(&awg);
repeat(tONP2/(500*tVeryLong),&awg); 2nd half of ONP
    signal(3,250,&awg);
    signal(3,250,&awg);
endrepeat(&awg);
repeat((tShut+tVcycleUP)/(200*tLong),&awg); Delay while shutter closes
    signal(2,200,&awg);    and field cycles
endrepeat(&awg);
signal(5,1,&awg);
signal(2,tDeph/tLong,&awg);
signal(6,1,&awg);          t1 period !
signal(2,t1/tLong,&awg);
signal(7,1,&awg);
signal(2,t1/tLong,&awg);
signal(8,1,&awg);
repeat((tVcycleDOWN+tShut)/(200*tLong),&awg); Delay while field cycles
    signal(9,200,&awg);    and shutter opens
endrepeat(&awg);
signal(10,1,&awg);          Pi/2 Ga(71), As(75) pulse, ref
repeat(tLock/(200*tLong),&awg); Lock Ga(71), As(75), ref
    signal(11,200,&awg);
endrepeat(&awg);
repeat(tPlock/(200*tLong),&awg); ref only
    signal(12,200,&awg);
endrepeat(&awg);
signal(0,1,&awg);
finish(&awg);

#if AWGDIAG
print_signal_AWG(0,"AWG SIGNAL 0",&awg);
print_program_AWG("AWG PROGRAM",&awg);
print_header_AWG("AWG HEADER",&awg);
#endif

```

CREATE ITI DATA

```
init_ITI(&iti); Initialize ITI structure
```

```
Open shutter, hold rf switches open
```

```

addword(1, TRG_REC | SW1_RF | SW2_RF, TIME(0, 49,500, 0), &iti);
addword(1, OPEN_S | TRG_REC | SW1_RF | SW2_RF, TIME(0, 1, 0, 0), &iti);
addword(1, TRG_REC | SW1_RF | SW2_RF, TIME(0, 49,500, 0), &iti);
deftable(1,&iti);

```

Close shutter, hold rf switches open

```

addword(2, TRG_REC | SW1_RF | SW2_RF, TIME(0, 49,500, 0), &iti);
addword(2, CLOSE_S | TRG_REC | SW1_RF | SW2_RF, TIME(0, 1, 0, 0), &iti);
addword(2, TRG_REC | SW1_RF | SW2_RF, TIME(0, 49,500, 0), &iti);
deftable(2,&iti);

```

Dummy table for open and close shutter

```

addword(3, TRG_REC | SW1_RF | SW2_RF, TIME(0, 49,500, 0), &iti);
addword(3, TRG_REC | SW1_RF | SW2_RF, TIME(0, 1, 0, 0), &iti);
addword(3, TRG_REC | SW1_RF | SW2_RF, TIME(0, 49,500, 0), &iti);
deftable(3,&iti);

```

Trigger NIC

```

addword(4, TRG_NIC, TIME(0, 0, 1, 0), &iti);
addword(4, BLANK, TIME(0, 0, 10, 0), &iti);
addword(4, TRG_NIC, TIME(0, 0, 1, 0), &iti);
addword(4, BLANK, TIME(0, 0, 10, 0), &iti);
deftable(4,&iti);

```

Trigger AWG

```

addword(5, TRG_AWG, MICROSEC(1), &iti);
addword(5, TRG_REC | SW1_RF | SW2_RF, NANOSEC(400), &iti);
addword(5, TRG_REC | SW1_RF | SW2_RF, tSpd, &iti);
addword(5, TRG_REC | SW1_RF | SW2_RF, tDeph, &iti);
deftable(5,&iti);

```

```

addword(6, TRG_REC | SW1_RF | SW2_RF, 250*tVeryLong, &iti);
addword(6, TRG_REC | SW1_RF | SW2_RF, 250*tVeryLong, &iti);
deftable(6,&iti);

```

```

addword(7, TRG_REC | SW1_RF | SW2_RF, tRp, &iti);
addword(7, TRG_REC | SW1_RF | SW2_RF, tMp, &iti);
addword(7, TRG_REC | SW1_RF | SW2_RF, tDeph, &iti);
deftable(7,&iti);

```

```

addword(8, TRG_REC | SW1_RF | SW2_RF, 100*tLong, &iti);
addword(8, TRG_REC | SW1_RF | SW2_RF, 100*tLong, &iti);
deftable(8,&iti);

```

```

addword(9, TRG_REC | SW1_RF | SW2_RF, tSi, &iti);
addword(9, TRG_REC | SW1_RF | SW2_RF, tDeph, &iti);
addword(9, TRG_REC | SW1_RF | SW2_RF, tSre, &iti);
addword(9, TRG_REC | SW1_RF | SW2_RF, t1, &iti);
addword(9, TRG_REC | SW1_RF | SW2_RF, 2*tSpe, &iti);
addword(9, TRG_REC | SW1_RF | SW2_RF, t1, &iti);
addword(9, TRG_REC | SW1_RF | SW2_RF, tSpe, &iti);
deftable(9,&iti);

```

```

addword(10, TRG_REC | SW1_RF | SW2_RF, tRp, &iti);
addword(10, TRG_REC | SW1_RF | SW2_RF, tMp, &iti);
addword(10, TRG_REC | SW1_RF | SW2_RF, tSpd, &iti);
deftable(10,&iti);

```

Tell Nic to take data

Wait between data points

```

addword(11, EP_NIC | TRG_REC | SW1_RF | SW2_RF, MICROSEC(100), &iti);
addword(11, TRG_REC | SW1_RF | SW2_RF, delt2 - MICROSEC(100), &iti);
deftable(11,&iti);

```

```

addmain(nMAIN, &iti);

```

```

addmiddle( 1,1,&iti);
addtable( 4,1,&iti);           Externally trigger Nic
addtable( 1,1,&iti);           Open shutter
addtable( 5,10,&iti);          Saturate Ga(71)
addtable( 6,tONP1/(500*tVeryLong),&iti); Delay for ONP1
addtable( 7,10,&iti);          Saturate Ga(69), As(75)
addtable( 6,tONP2/(500*tVeryLong),&iti); Delay for ONP2
addtable( 2,1,&iti);           Close shutter
addtable( 8,tVcycleUP/(200*tLong),&iti); Field cycle UP
addtable( 9,1,&iti);           Wait for t1 evolution
addtable( 8,tVcycleDOWN/(200*tLong),&iti); Field cycle DOWN
addtable( 1,1,&iti);           Close shutter
addtable(10,1,&iti);           Pulse
addtable(11,NT2,&iti);         Take data
addtable( 2,1,&iti);           Close shutter
addmiddle(2,0,&iti);

```

GET DATA FROM SCOPE

```

if ( loop != 0 )
{
    while ( is_completed_ITI(&iti) == 2 )    Wait for ITI to finish
    {
        delay_millsec(100); if (EVENTS) printf("\nwaiting for iti");
    }

    enslave_NIC(&nic);           Put NIC under computer control
    read_data_NIC(1,t2,NT2,&nic); Get NIC CH1 data
    read_data_NIC(2,t2,NT2,&nic); Get NIC CH1 data
    release_NIC(&nic);          Release NIC from computer control
}
if ( loop == 0 )
{
    fprintf(fpDAT,"%0.8f DWELL\n",ttoMICROSEC(delt2)*1.0E-6);
    fprintf(fpDAT,"%d NPTS\n",NT2);
}
else
{
    print_data_NIC(fpDAT,t2,NT2,&nic); Write NIC CH1 CH2 data to file
}

```

USEFUL DIAGNOSTICS

```

#if ITIDIAG
print_ITI(&iti);
#endif

#if PAUSE
mypause();
#endif

}

```

END MAIN LOOP

```

dealloc_AWG(&awg);
dealloc_NIC(&nic);

#if ifCYC
write_param_SR(&sr); if (EVENTS) printf("\nre-initialize SR510");
#endif

printf("\nwriting to file temp.nic");
printf("\nwriting to file temp.dat");

```

```
printf("\a\a");  
exit(0);  
}
```

XV References

- [1] Electronic Structure of Semiconductor Heterojunctions,
G. Margaritondo, Ed., Kluwer Academic Publishers, Milano, Italy (1988).
- [2] Physics of Semiconductor Devices, 2nd Edition
S. M. Sze, John Wiley and Sons, NY (1981).
- [3] Principles of Nuclear Magnetism, 1st Edition
A. Abragam, Clarendon Press, Oxford (1961).
- [4] *Nuclear Dynamic Polarization by Optical Electronic Saturation and Optical Pumping in Semiconductors*
G. Lampel, Physical Review Letters **20** 491 (1968).
- [5] Optical Orientation,
F. Meier and B. P. Zakharchenya, Eds., Elsevier, Amsterdam (1984).
- [6] *Directly Detected Nuclear-Magnetic-Resonance of Optically Pumped GaAs Quantum-Wells*
S. E. Barrett, R. Tycko, L. N. Pfeiffer, and K. W. West, Physical Review Letters **72** 1368-71 (1994).
- [7] *Optical Detection of Dynamic Polarization of Nuclei in Semiconductors*
A. I. Ekimov and V. I. Safarov, JETP Letters **15** 179 (1972).
- [8] *Optical Polarization of Nuclei in GaAs/AlGaAs Quantum Well Structures*
V. K. Kalevich, V. L. Korenev, and O. M. Fedorova, JETP Letters **52** 349 (1990).
- [9] *Optically Detected Nuclear Magnetic Resonance and Knight Shift in $Al_xGa_{1-x}As$ /GaAs Heterostructures*
M. Krapf, G. Denninger, H. Pascher, G. Weimann, and W. Schlapp, Solid State Communications **78** 459 (1991).
- [10] *Optically Detected Nuclear Magnetic Resonance of Nuclei within a Quantum Well*
G. P. Flinn, R. T. Harley, M. J. Snelling, A. C. Tropper, and T. M. Kerr, Semiconductor Science and Technology **5** 533 (1990).
- [11] *Low Field Electron-Nuclear Spin Coupling in Gallium Arsenide Under Optical Pumping Conditions*
D. Paget, G. Lampel, B. Sapoval, and V. I. Safarov, Physical Review B **15** 5780 (1977).

[12] *Time-Sequenced Optical Nuclear Magnetic Resonance of Gallium Arsenide*

S. K. Buratto, D. N. Shykind, and D. P. Weitekamp, *Physical Review B* **44** 9035 (1991).

[13] *Fourier-Transform Time-Sequenced Optical Nuclear Magnetic Resonance of Gallium Arsenide*

S. K. Buratto, J. Y. Hwang, N. D. Kurur, D. N. Shykind, and D. P. Weitekamp, *Bulletin of Magnetic Resonance* **15** 190 (1993).

[14] *Optical Larmor Beat Detection of High-Resolution Nuclear Magnetic Resonance in a Semiconductor Heterostructure*

J. A. Marohn, P. J. Carson, J. Y. Hwang, M. A. Miller, D. N. Shykind, and D. P. Weitekamp, *Physical Review Letters* **75** 1364-7 (1995).

[15] Experimental Techniques in Low-Temperature Physics, 3rd Edition

G. K. White, Clarendon Press, Oxford (1989).

[16] *Application Notes*

J. C. Kemp, HINDS International Inc.

[17] J. C. Kemp, *Journal of the Optical Society* **59** 950 (1969).

[18] Experimental Pulse NMR: A Nuts and Bolts Approach,

E. Fukushima and S. B. W. Roeder, Addison-Wesley Publishing Company, Inc., Reading, Massachusetts (1981).

[19] The New Peter Norton Programmer's Guide to the IBM PC & PS/2,

P. Norton and R. Wilton, Microsoft Press (1988).

[20] *Time-Domain Multiple-Quantum NMR*

D. P. Weitekamp, *Advances in Magnetic Resonance* **11** 111-274 (1983).

Chapter 7: What Can Optical Nuclear Magnetic Resonance Measure in Single 2D Epitaxial Structures?

I Abstract

Recently we demonstrated Larmor beat detection (LBD), a novel shot-noise limited optical detection method for NMR of semiconductors which allows the full power of high-resolution solid-state NMR to be applied to single epitaxial structures. Here we apply LBD to study a single p-channel $\text{Al}_{0.36}\text{Ga}_{0.64}\text{As}/\text{GaAs}$ heterojunction. Results on an externally strained sample indicate that the method has an orders-of-magnitude resolution advantage over competing fixed-field optical detection methods. Splittings observed in a preliminary rotation study on an unstrained sample put a surprisingly low upper bound on the electric field present at the most rapidly polarizable sites in the heterojunction. Knight shift measurements lend support to a model in which these sites are luminescent donors at locations where the built in E -field has fallen off.

II Introduction

Recently we demonstrated Larmor beat detection, a novel shot-noise limited optical detection method for NMR of semiconductors which allows the full power of high-resolution of solid-state NMR to be applied to single epitaxial structures [1]. A motivating goal for this development was the possibility of layer-resolved measurements of the electron wavefunction via the Knight shift [2]. In analogy with bulk studies, the large built-in and induced E fields characteristic of epitaxial structures might also be accurately measured using the linear Stark effect of the nuclear quadrupole Hamiltonian [3].

In this paper we employ optical Larmor beat detection in sensitive time-sequenced experiments to study a single p-channel GaAs heterojunction. Krapf and co-workers have previously investigated this sample using conduction-electron spin resonance and steady-state optically detected nuclear magnetic resonance [4, 5]. Both these measurements indicated large nuclear hyperfine fields favorable for optically detecting NMR, but the low resolution of NMR spectra acquired by steady-state optical detection did not allow precise measurements of electron density by measurement of the Knight shift.

III Sample and Experimental Details

The sample studied was a single p-channel GaAs/AlGaAs heterojunction grown along the [001] axis by molecular beam epitaxy [4-7]. A sketch of the sample appears in FIG 1. A substrate of semi-insulating GaAs supports a 2500 nm layer of undoped GaAs, followed by a 6.5 nm layer of undoped $\text{Al}_x\text{Ga}_{1-x}\text{As}$ ($x = 0.36$), a 30 nm layer of p-type $\text{Al}_x\text{Ga}_{1-x}\text{As}$ ($x = 0.36$) doped with $6 \times 10^{17}/\text{cm}^3$ of Be, and a 21 nm layer of undoped GaAs. The photoluminescence spectrum (FIG. 2) of the sample reveals the expected lines at 818 nm (bulk exciton luminescence) [4, 5], and 825 nm and 830 nm (e -line and d -line respectively of H -band luminescence) [6, 7] which have been assigned to transitions involving the recombination with electrons of the 2D heavy holes localized near the interface between GaAs and undoped AlGaAs. We note that the 830 nm line, hypothesized to involve recombination near carbon impurities, is more pronounced in our sample compared to published spectra by Ossau *et al.* [6].

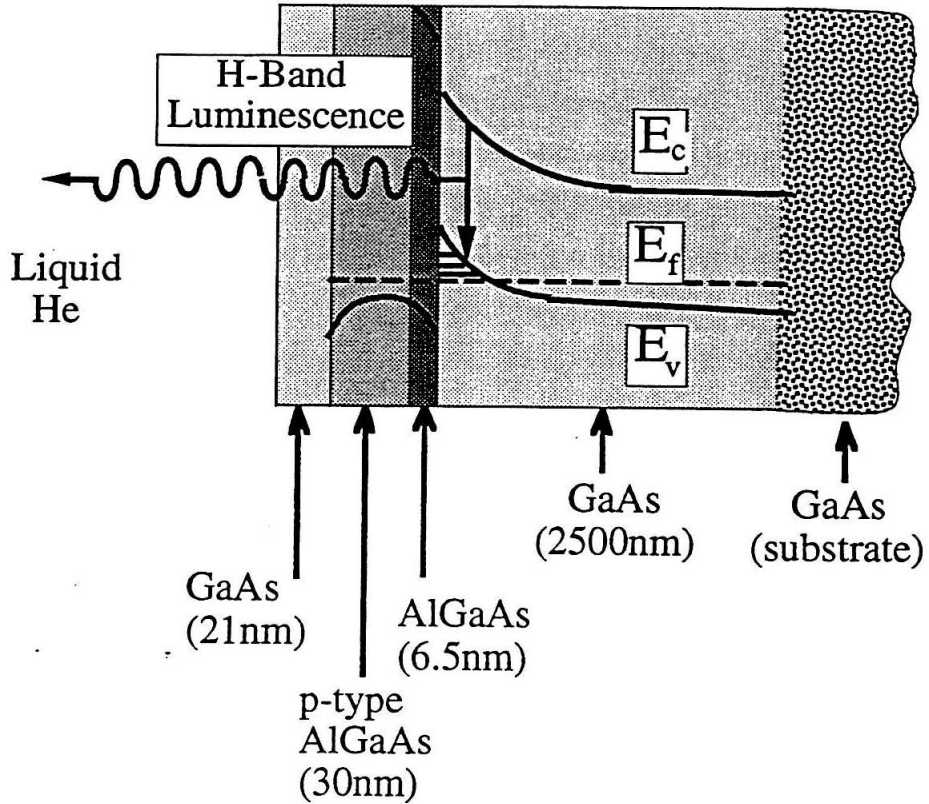


FIG. 1. Schematic of the heterojunction sample.

Band bending confines holes donated from the $\text{Al}_{0.36}\text{Ga}_{0.64}\text{As}$ to GaAs the interface, where, isolated from scattering centers, they form a high-mobility 2D hole gas.

The sample was attached by high vacuum grease or varnish to a G-10 fiberglass probe immersed in 2 K superfluid ^4He . The 240 mT Zeeman field, optical detection axis, and sample growth axis were nominally parallel. A GaAs/AlGaAs laser diode delivered ~ 5 mW CW of circularly polarized 780 nm light over ~ 1 mm², incident 15° off axis. Sample luminescence passed through a 50 kHz photoelastic modulator, a linear polarizer, an 830 nm bandpass filter (FWHM 10 nm), and was detected with a silicon avalanche photodiode in linear mode. For steady-state experiments, the photocurrent was demodulated by 50 kHz. For Larmor beat experiments, the photocurrent was demodulated by the relevant beat frequency plus or minus 50 kHz. The demodulated signal, proportional to the time-dependent difference in intensity between left and right circularly polarized luminescence, was digitized.

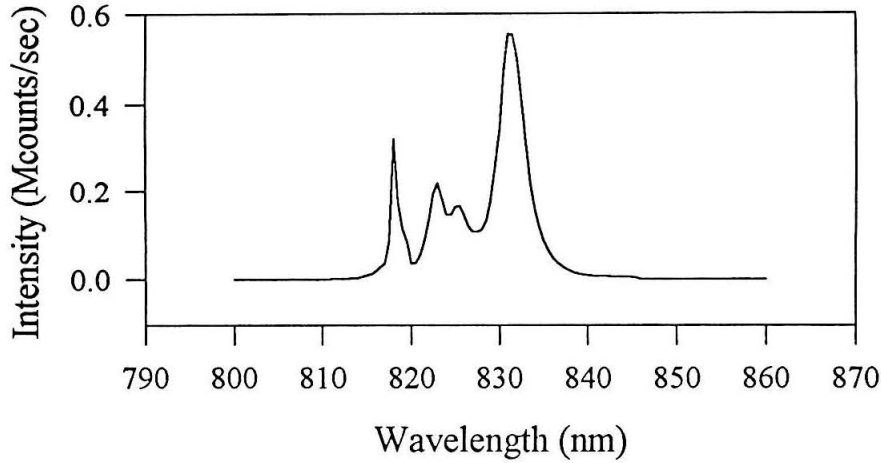
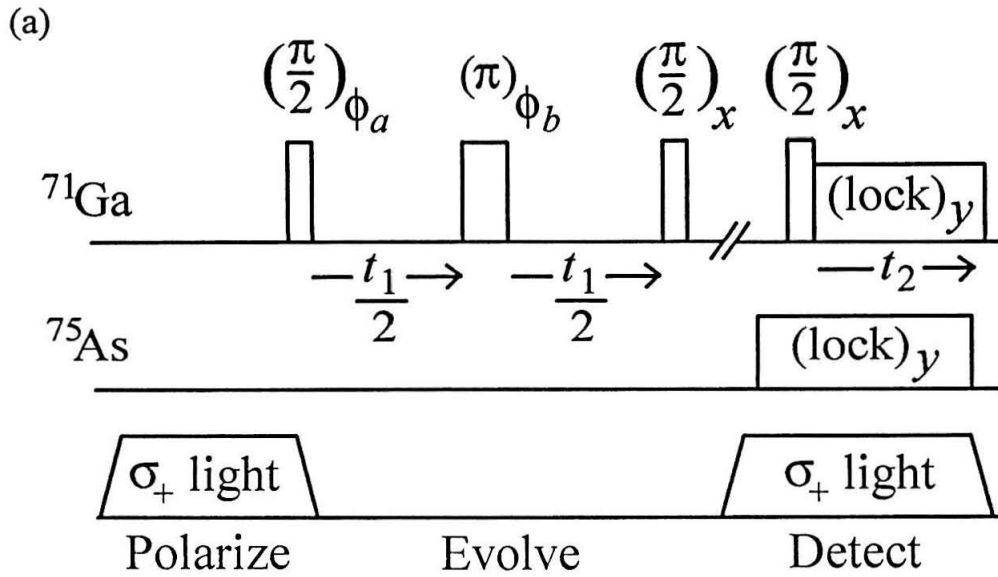


FIG. 2. Photoluminescence spectrum of the heterojunction.

The sample was excited with 1.4 W/mm^2 at 514.5 nm and $4.7\text{-}5 \text{ K}$ (Spectra Physics 2020 Ar+ laser). Luminescence was detected through a 1 m monochromator giving 0.2 nm resolution (SPEX 1704).

IV Results and Discussion

Early work highlighted the ability of Larmor beat optical detection to record spectra at high field in real time (Chapter 5). As in ordinary NMR, the 1D real-time free induction decay (FID) experiment has sensitivity inferior to an analogous 2D experiment in which spin-locking is used to prolong the transverse signal magnetization [8]. The sequence needed is shown in FIG. 3. The experiment begins with a train of ten $\pi/2$ pulses (10 ms apart) to each of the principle isotopes (not shown) to provide a reproducible condition saturation or null spin order before each shot. After a period τ_L of optical pumping, the shutter is closed, and ^{71}Ga magnetization is evolved as in any NMR experiment. The sequence shown is a spin echo, $(\pi/2)_{\phi_a} - t_1/2 - (\pi)_{\phi_b} - t_1/2 - (\pi/2)_x$. Detection during t_2 is prolonged by spin locking the ^{71}Ga magnetization remaining along a chosen rotating-frame axis while spin locking the reference ^{75}As isotope. The optical transient, now at the difference in irradiation frequencies,



(b)

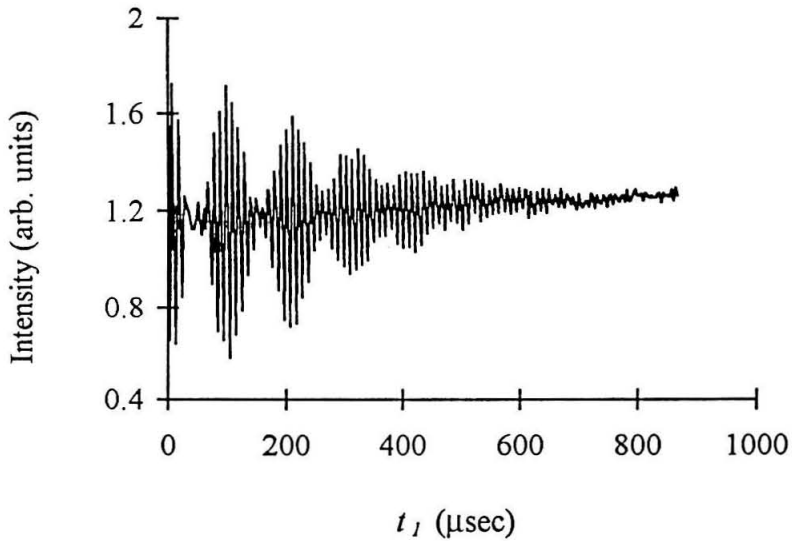


FIG. 3. Time-sequenced spin-echo NMR employing optical Larmor beat detection.

(a) Timing sequence. The optical transient in t_2 is demodulated by the Larmor beat frequency, integrated, and plotted versus t_1 to yield the spin-echo interferogram (b).

is demodulated, integrated, and plotted versus t_1 to yield the desired NMR interferogram. By leaving out the π pulse at $t_1/2$, we may record a free evolution decay interferogram, and by extending the first pulse the full length of t_1 , we may record a nutation transient. The signal-to-noise ratio per shot improves in these 2D experiments by $\sim (T_{1\rho}/T_2)^{1/2}$ since the signal persists for the spin-locking time $T_{1\rho}$ (~ 1 s) instead of the decay time T_2 for the FID (~ 100 μ s). The spectrum of interest can be shifted away from artifacts due to drifts in the total signal amplitude by applying time proportional phase incrementation (TPPI) [9], in which the phase of the on-resonance preparation pulse is stepped according to $\phi_a = \omega_{\text{tppi}} t_1$. TPPI may similarly be applied to the refocusing pulse.

As a point of reference, FIG. 4(a) shows the quasi-steady-state CW ^{71}Ga optical NMR spectrum ($\tau_L = 30$ s) of the heterostructure, reproducing the result of Ref. [5] on our sample. The signal grows in during optical nuclear polarization with a time constant of 500 s. This steady-state spectrum is featureless even for ^{71}Ga Rabi frequencies small compared to the dipolar local field, while in contrast the Fourier transform of the ^{71}Ga FID ($\tau_L = 5$ s) recorded using Larmor beat detection shows a well-resolved triplet (FIG. 4(b)). Since a spin-echo experiment (FIG. 4(c)) refocuses evolution due to static field inhomogeneity, chemical shifts, and heteronuclear dipolar couplings, the surviving triplet structure is shown to be due to quadrupole coupling. Splittings observed in the ^{69}Ga spectra (not shown) scale with nuclear quadrupole moment, verifying this conclusion. The nutation spectrum (FIG. 4(d)) in which the triplet splitting is half as large also verifies a quadrupole coupling and reveals an ω_1 of 35.1 kHz (where $\omega_1 = \gamma_N^{\text{sig}} B_1$ and B_1 is the magnitude of the resonant circular component of the applied rf field). The lack of a peak at 52.6 kHz, where $2\omega_1$ would fold into the nutation spectrum, proves that there are no strongly quadrupole-perturbed sites ($\omega_Q \gg \omega_1$) contributing to the spectrum [10].

The spectra of Fig. 4(b-d) are consistent with a roughly Gaussian distribution of ^{71}Ga quadrupole splittings (mean splitting of -18.6 ± 0.1 kHz and FWHM of 4.6 ± 0.3 kHz) corresponding to an electric field gradient whose principal component along [001] is $V_{zz} = -6.76 \times 10^{18}$ V/m² (where the sign is obtained as discussed below). The mean quadrupole splitting varied from 12 to 20 kHz between dewar cooling cycles, although, as discussed below, this splitting can be made to disappear with strain-free sample mounting.

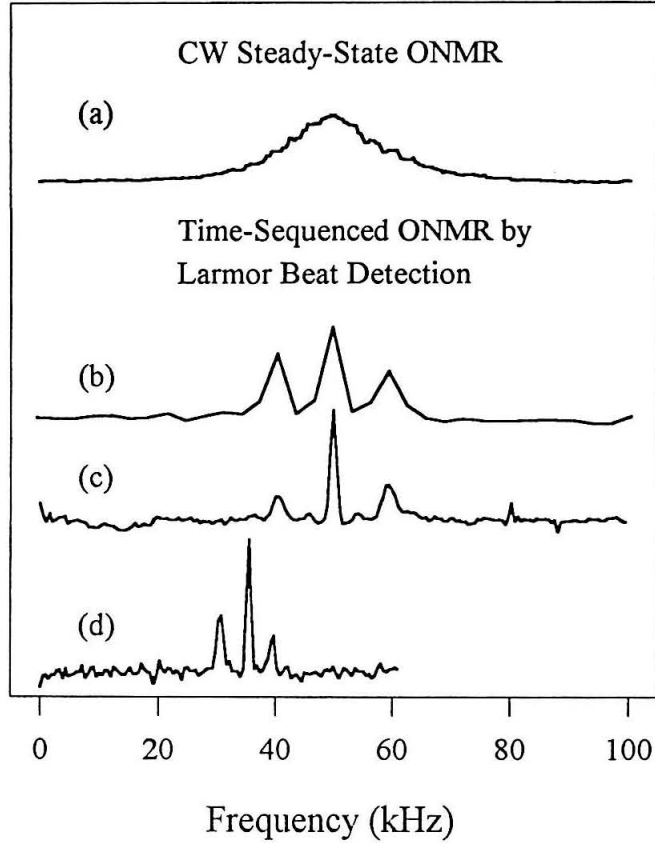


FIG. 4. Optical NMR spectra of the heterostructure.

(a) Steady-state CW ^{71}Ga optical NMR spectrum (see text). (b) Fourier transform of ^{71}Ga free induction decay in t_1 , following a $\theta = \pi/2$ pulse, recorded by Larmor beat detection in t_2 . (c) Spin echo spectrum. (d) Nutation spectrum. Each spectrum (b)-(d) results from one t_2 transient at each t_1 point, with the entire set of transients taken in 30 minutes.

An electric field gradient (EFG) can be induced at a nuclear site in GaAs when its tetrahedral symmetry is broken due to local bonding effects [11] (inconsistent with the observed narrow distribution of quadrupole couplings) as well as by changes in electron distribution due to strain [12] induced by lattice mismatch or external pressure. Quadrupole couplings observed previously in quantum wells have been attributed to external strain such as that developed in a rigidly mounted sample upon cooling [13].

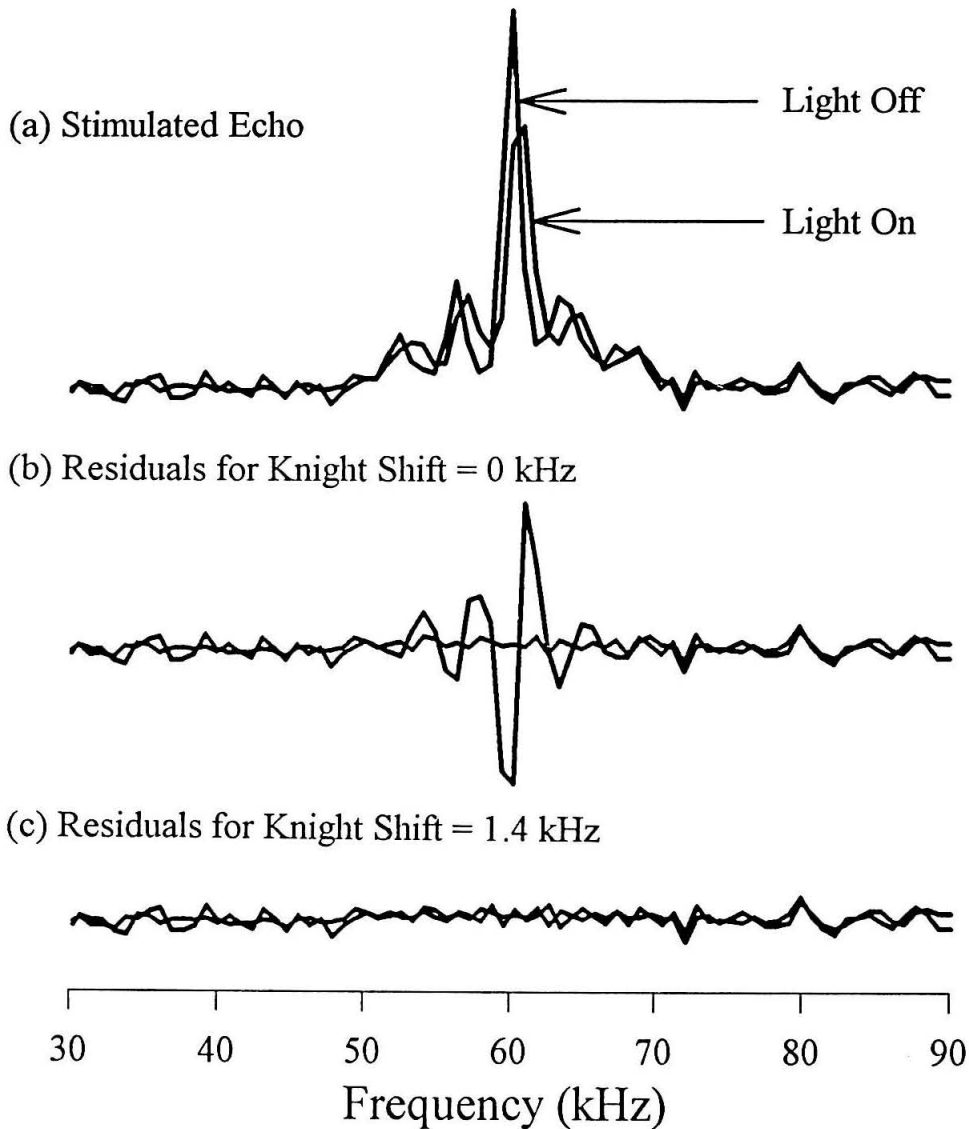


FIG. 5. Optically-induced Knight shift measurement.

(a) Stimulated echo spectra of a strained sample. For the “Light on” spectrum, the sample has been irradiated during half of the stimulated echo. Assuming no Knight shift is present, the best fit to the “Light off” spectrum shown in (a) has the residuals shown in (b). The residuals in (c) indicate a ^{71}Ga Knight shift of 1.4 kHz.

Assuming that our splittings are due to external strain perpendicular to [001], we infer a strain of 70 ppm and in turn a pressure of 8.2×10^6 Pa (0.082 kbar). An EFG can also be induced by electric fields [3],

even when they are homogeneous. Symmetry arguments [3, 14] show, however, that an electric field $E_{[001]}$ (such as the built-in electric field of the heterojunction) in a cubic crystal gives rise to an EFG whose principal component along [001] vanishes, so that varying the angle between \mathbf{B}_0 and [001] would be required to measure $E_{[001]}$. Since a ^{69}Ga quadrupole splitting as small as 1.0 kHz is resolvable, the current technique, modified to allow variation of the angle between \mathbf{B}_0 and crystal axes, could be used to sort out these contributions and thus to measure internal electric fields with a resolution of 50 kV/m and strains as small as 4 ppm in a single heterojunction.

The dependence of the satellite ratios on preparation-pulse tip angle θ measures the ^{71}Ga nuclear spin polarization (and reveals the sign of V_{zz} [15]). Assuming a single spin temperature, the satellite ratios measured as a function of θ indicate nuclear spin polarizations on the order of -10%. The calculated polarization enhancement due to ONP is approximately 2000.

A measurement of the optically-induced Knight shift appears in FIG. 5. The pulse sequence used is the stimulated echo [16]: $\pi/2 -t_1/2 -\pi/2 -\tau_{\text{DELAY}} -\pi/2 -t_1/2 -\pi/2$. The sequence partially refocuses evolution due to static field inhomogeneity, chemical shifts, and heteronuclear dipolar couplings. The time $\tau_{\text{DELAY}} \sim 10$ ms allows the light to be shuttered on, so that evolution under the Knight shift is not refocused by the echo. The extra doublet appearing at only half the quadrupole splitting is due to coherence pathways that exchange central transition coherence with satellite coherence.

The observed 0.69 kHz shift in line positions, corresponding to a 1.38 ± 0.06 kHz (1.8 Gauss) ^{71}Ga Knight shift, is consistent with the detected nuclei being located near a paramagnetic donor. Paget [17] estimates the time-averaged electron hyperfine field $\langle \mathbf{B}_e(\mathbf{r}) \rangle$ felt by nuclei a distance r away from an occupied donor site (Bohr radius $a_0 = 10$ nm) to be

$$\langle \mathbf{B}_e(\mathbf{r}) \rangle = \Gamma \langle \mathbf{S} \rangle b_e(0) \exp(-2r/a_0), \quad (1)$$

where Γ is an occupation factor, $\langle \mathbf{S} \rangle$ is the time-averaged spin of electrons occupying the donor site, and $b_e(0) = -130$ Gauss for ^{71}Ga . With $\langle \mathbf{S} \rangle = 0.06$ inferred from luminescence polarization, and taking $\Gamma = 1$, the shift is consistent with observing nuclei a distance $r \sim 0.7 a_0$ from the donor center. Since $b_e(0) \propto 1/a_0^3$, the data is also consistent with observing nuclei a distance $r \sim a_0$ away from a slightly larger ($a_0 = 8.2$ nm) donor. A signal weighting function $W(r)$ for optical NMR with maximum near $r \sim$

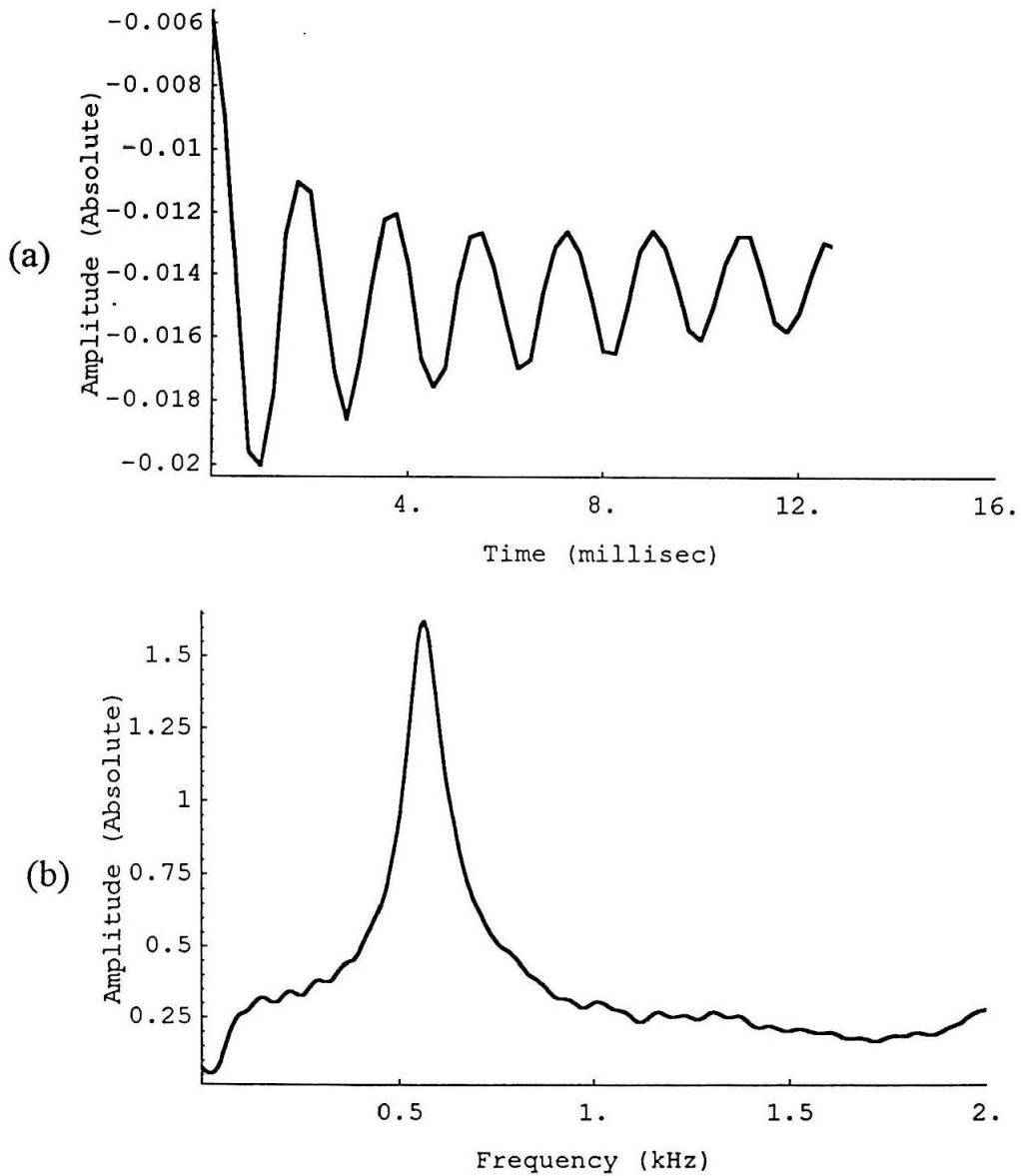


FIG. 6. Line-narrowed optical NMR spectrum of the heterostructure.

(a) CLSW-16 ($t_{90} = 3.45 \mu\text{s}$, $\tau_c = 250 \mu\text{s}$) t_1 interferogram. (b) Fourier transform of the interferogram, after line broadening by 80 Hz. The observed linewidth is 127 Hz, indicating an intrinsic linewidth of < 50 Hz. Homogeneous pulse offsetting, instead of time-proportional phase incrementation of the preparation pulse, has been used to shift the interferogram from zero frequency. The observed offset of 565 ± 63 Hz agrees well with the expected 606 Hz.

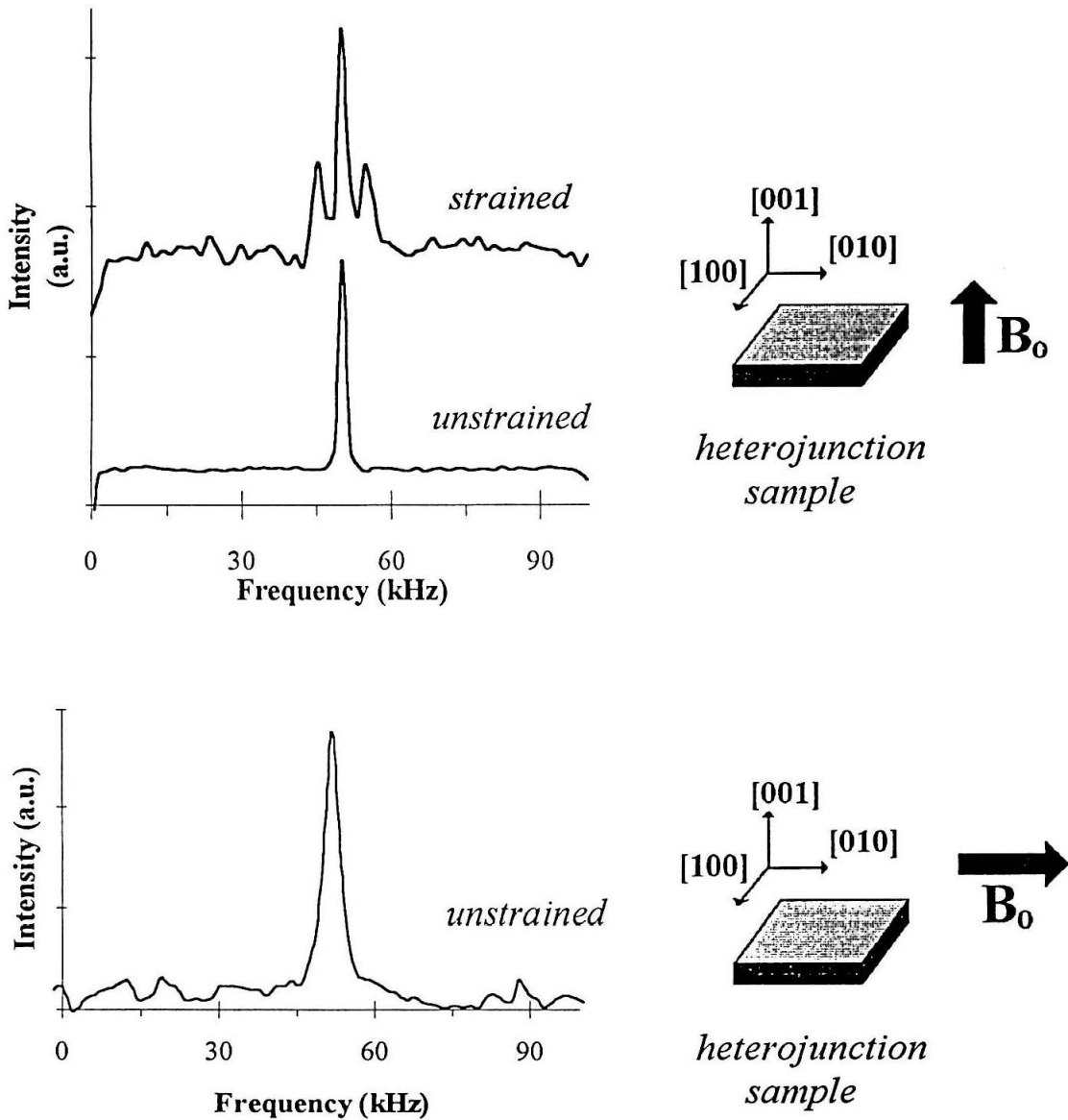


FIG. 7. Optical NMR spectra of the unstrained heterostructure.

(Top) Spin-echo spectra for a strained, then unstrained sample. Magnetization in both cases evolved with the 0.24 T magnetic field oriented along the [001] crystal axis of the heterostructure; (Bottom) Spin-echo spectrum of an unstrained sample where magnetization evolved with the magnetic field along the [010] axis.

a_0 is expected. Indeed, assuming nuclei are equally polarized within the donor volume,

$$W(r) \propto r^2 \exp(-2r / a_0), \quad (2)$$

where the first term is a weighing proportional to the number of nuclei in a shell a distance r from the donor, and the second term is proportional to the hyperfine coupling at r . This function indeed peaks at $r \sim a_0$. We note also a statistically significant change in the width of the central transition, from 1.32 ± 0.05 kHz (light off) to 1.78 ± 0.05 kHz (light on).

A much higher resolution Knight shift measurement is possible by intercalating light pulses into the windows of a more powerful line-narrowing sequence than the stimulated echo [2]. As a first step towards such an experiment, we have evolved ^{71}Ga magnetization under the CLSW-16 line-narrowing sequence [18] (discussed in Chapter 2). See FIG. 6. The observed linewidth, ~ 50 Hz, indicates that Knight shift measurements with resolution improved by ~ 20 fold are feasible.

In FIG. 7 (top), we have removed the quadrupole coupling by more carefully mounting the sample, verifying that the electric field gradient quantified above is in fact due to external strain. To obtain the “unstrained” spectrum, the sample was affixed with the smallest amount of vacuum grease, and slowly cooled from room temperature to 77 K over a 6 hour period (cooling further to 2 K occurs in 20 minutes). FIG. 7 (bottom) shows the result of a spin echo experiment in which magnetization has evolved with the static field along the [010] crystal axis.

The lack of resolved quadrupole splittings in this spectrum indicates that, at sites responsible for the NMR signal, the E field is less than ~ 5 kV/cm [3]. We must, then, be observing donors well away from the heterojunction’s ~ 250 kV/cm built-in interfacial electric field [19]. This is not unexpected since (1) spin-polarized free carriers created by optical pumping should be swept away from the interface by the interfacial E -field, as in a diode [20], before they can trap at a donor site and (2) donor sites cannot be occupied near the interface in any case since thermodynamic predictions assert that these sites are emptied by E fields as small as ~ 6 kV/cm. Consider an electron sitting in a donor-site potential well having a Bohr radius of 10 nm and a depth of 6 meV (a typical donor ionization energy). In this case an applied field of $6\text{mV}/10\text{nm} = 6$ kV/cm would lower the barrier enough for thermal processes at 2 K to ionize the donor.

V Conclusions

NMR line splittings in a strained p-channel AlGaAs/GaAs heterojunction observed by optical Larmor beat detection show that method has an orders-of-magnitude resolution advantage over competing fixed-field optical detection methods for measuring strain and electric fields. Preliminary rotation studies on an unstrained sample are consistent with a surprisingly low upper bound for E -fields at the most rapidly polarizable sites in the heterojunction. Knight shift measurements are consistent with these sites being donors. Taken together, the data suggests we are observing sites near donors situated at locations where the built-in interfacial field has fallen off. A spectrum collected for ^{71}Ga evolving under a 16-pulse line-narrowing sequence achieves ~ 50 Hz resolution, indicating that Knight shift measurements improved by ~ 20 fold are possible. Remarkably, this is not far from the resolution required (~ 10 Hz) to resolve atomic layers in a quantum well by the conduction-electron Knight shift.

Larmor beat optical detection combined with rotation studies should allow measurement of interfacial E -fields to better than 1%. Unfortunately, this interfacial field is not observed here. As thermodynamic arguments indicate, even a small E -field is enough to ionize donors and preclude optical nuclear polarization and detection near the interface. One way to regain sensitivity to interfacial nuclei would be to let spin diffusion carry nuclear spin polarization to and from the region of large interfacial E -field (>30 nm away). Given the measured spin-diffusion coefficient for ^{75}As in GaAs of $0.1 \text{ nm}^2/\text{s}$ [21], this could take many minutes. A more time-efficient alternative would be to bias the sample — and “unbend” the bands [20] — during optical pumping and detection, allowing optical nuclear polarization and detection through now un-ionized near-interface donor sites. The sample could be unbiased during NMR evolution, in a time-sequenced experiment, to map out the interfacial E field.

VI Acknowledgments

This work was funded by the NSF program in Materials Synthesis and Processing and by NASA through the Caltech President's Fund. We thank A. Ksendzov, J. Liu, and F. Grunthner of the NASA Jet

Propulsion Laboratory's Center for Space Microelectronics Technology for sample preparation and luminescence characterization, and L. Burnett and A. Perry for cryogenics advice.

VII References

- [1] *Optical Larmor Beat Detection of High-Resolution Nuclear Magnetic Resonance in a Semiconductor Heterostructure*
J. A. Marohn, P. J. Carson, J. Y. Hwang, M. A. Miller, D. N. Shykind, and D. P. Weitekamp, Physical Review Letters **75** 1364-7 (1995).
- [2] *Can Nuclear Magnetic Resonance Resolve Epitaxial Layers?*
S. K. Buratto, D. N. Shykind, and D. P. Weitekamp, Journal of Vacuum Science and Technology B **10** 1740 (1992).
- [3] *Electric Shifts in Magnetic Resonance*
N. Bloembergen, Proc. Colloq. Ampere (Atomes Mol. Etudes Radio Elec.) **11** 39-57 (1962).
- [4] *Optically Detected Conduction Electron Spin Resonance, Overhauser Shift, and Nuclear Magnetic Resonance in $Al_xGa_{1-x}As/GaAs$ Heterostructures*
M. Krapf, G. Denninger, H. Pascher, G. Weimann, and W. Schlapp, Superlattices and Microstructures **8** 91-6 (1990).
- [5] *Optically Detected Nuclear Magnetic Resonance and Knight Shift in $Al_xGa_{1-x}As/GaAs$ Heterostructures*
M. Krapf, G. Denninger, H. Pascher, G. Weimann, and W. Schlapp, Solid State Communications **78** 459 (1991).
- [6] *Radiative Recombination of a 3D-Electron with a 2D-Hole in p-Type $GaAs/(GaAl)As$ Heterojunctions*
W. Ossau, E. Bangert, and G. Weimann, Solid State Communications **64** 711 (1987).
- [7] *New Photoluminescence Effects of Carrier Confinement at an $AlGaAs/GaAs$ Heterojunction Interface*
Y. R. Yuan, M. A. A. Pudensi, G. A. Vawater, and J. L. Merz, Journal of Applied Physics **58** 397 (1985).
- [8] *Time-Domain Multiple-Quantum NMR*
D. P. Weitekamp, Advances in Magnetic Resonance **11** 111-274 (1983).
- [9] G. Drobny, A. Pines, S. Sinton, D. P. Weitekamp, and D. Wemmer, Symp. Faraday Soc. **13** 49 (1979).
- [10] *2D NMR Nutation Spectroscopy in Solids*
A. Samoson and E. Lippmaa, Journal of Magnetic Resonance **79** 255-68 (1988).
- [11] *Structural Concepts for Disordered Inorganic Solids - Modern NMR Approaches and Strategies*

H. Eckert, *Berichte der Bunsen Gesellschaft für Physicalische Chemie* **94** 1062-85 (1990).

[12] *Experimental gradient-elastic tensors and chemical bonding in III-V semiconductors*

R. K. Sundfors, *Physical Review B* **10** 4244-52 (1974).

[13] *Optically Detected Nuclear Magnetic Resonance of Nuclei within a Quantum Well*

G. P. Flinn, R. T. Harley, M. J. Snelling, A. C. Tropper, and T. M. Kerr, *Semiconductor Science and Technology* **5** 533 (1990).

[14] *Macroscopic Symmetry and Properties of Crystals*

C. S. Smith, in *Solid State Physics: Advances in Research and Applications*, edited by F. Seitz and D. Turnbull, Academic Press, New York (1958), Vol. 6, p. 175-249.

[15] *Signs of the Quadrupole Coupling in ${}^7\text{LiNO}_3$ from Nuclear Magnetic Resonance at Low Temperature*

P. L. Kuhns and J. S. Waugh, *Journal of Chemical Physics* **97** 2166-9 (1992).

[16] Principles of Nuclear Magnetic Resonance in One and Two Dimensions,

R. R. Ernst, G. Bodenhausen, and A. Wokaun, Oxford University Press, New York (1987).

[17] *Low Field Electron-Nuclear Spin Coupling in Gallium Arsenide Under Optical Pumping Conditions*

D. Paget, G. Lampel, B. Sapoval, and V. I. Safarov, *Physical Review B* **15** 5780 (1977).

[18] *Nutation Sequences for Magnetic Resonance Imaging in Solids*

H. M. Cho, C. J. Lee, D. N. Shykind, and D. P. Weitekamp, *Phys. Rev. Lett.* **55** 1923 (1985).

[19] N. Bothka, D. K. Gaskill, P. D. Wright, R. W. Kaliski, and D. A. Williams, *Journal of Crystal Growth* **107** 893 (1990).

[20] Physics of Semiconductor Devices, 2nd Edition

S. M. Sze, John Wiley and Sons, NY (1981).

[21] *Optical Detection of NMR in High-Purity GaAs: Direct Study of the Relaxation of Nuclei Close to Shallow Donors*

D. Paget, *Physical Review B* **25** 4444 (1982).